Univerzita Karlova v Praze
Matematicko-fyzikální fakulta

DIPLOMOVÁ PRÁCE

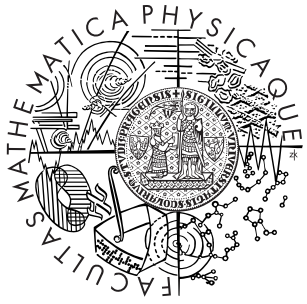

Bc. Stanislav Valenta

Fotonové silové funkce v jádře ^{177}Lu z měření dvoukrokových gamma kaskád

Ústav částicové a jaderné fyziky

Vedoucí diplomové práce: Mgr. Milan Krtička, Ph.D.

Studijní program: Fyzika, Jaderná a subjaderná fyzika

2010

Charles University in Prague
Faculty of Mathematics and Physics

DIPLOMA THESIS

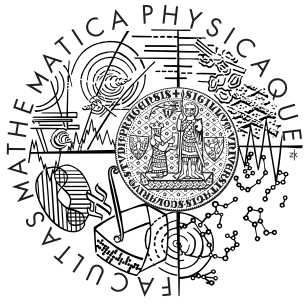

Bc. Stanislav Valenta

Photon strength functions in ^{177}Lu from two-step gamma cascade measurement

Institute of Particle and Nuclear Physics

Supervisor: Mgr. Milan Krtička, Ph.D.

Study Programme: Physics, Nuclear and Particle Physics

2010

Rád bych hluboce poděkoval vedoucímu mé práce Mgr. Milanu Krtičkovi, Ph.D. za jeho neutuchající snahu při časově náročném vedení této práce, cenné připomínky a diskuse a poskytnutí specializovaného softwaru a odborné literatury.

Za poskytnutí experimentálních dat naměřených na výzkumném reaktoru v Řeži a zajištění exkurze tamtéž velice děkuji Mgr. Ivu Tomandlovi, CSc.

Dále bych chtěl poděkovat několika přátelům za různorodou pomoc a podporu, jmenovitě pak Mgr. Jiřímu Krollovi, Bc. Petru Morávkovi a Bc. Martinovi Rusňákovi.

V neposlední řadě bych chtěl vyslovit díky své rodině a přítelkyni za neustávající podporu v celé době mých studií.

Prohlašuji, že jsem svou diplomovou práci napsal samostatně a výhradně s použitím citovaných pramenů. Souhlasím se zapůjčováním práce.

V Praze dne 16. srpna 2010 Bc. Stanislav Valenta

Contents

1 Introduction **7**

2 Photon strength functions and level density **10**
2.1 Level density 10
2.2 Photon strength functions 12
2.2.1 Fluctuation properties of partial radiation widths 15
2.2.2 $E1$ photon strength function 15
2.2.3 $M1$ photon strength function 20
2.2.4 $E2$ photon strength function 23
2.3 Total radiation width of capturing states 24

3 Modelling algorithm and experimental setup **25**
3.1 Two Step Cascades experiment 25
3.2 Computer simulations 32
3.2.1 Assumptions 32
3.2.2 The algorithm of the simulation method 33
3.2.3 Response of detector system 35

4 Results and discussion **38**
4.1 Analysis of the experimental data 38
4.2 Simulation 41
4.3 Comparsion of experimental data
with simulation results 43
4.3.1 Binned TSC spectra 43
4.3.2 Average total radiation width 48

5 Summary **83**

Název práce: Fotonové silové funkce v jádře ^{177}Lu z měření dvoukrokových gamma kaskád
Autor: Bc. Stanislav Valenta
Katedra (ústav): Ústav částicové a jaderné fyziky
Vedoucí diplomové práce: Mgr. Milan Krtička, Ph.D.
E-mail vedoucího: krticka@ipnp.troja.mff.cuni.cz

Abstrakt: V předložené práci studujeme fotonové silové funkce, jejichž studium probíhá již více než padesát let. V průběhu této doby byla vytvořena celá řada modelů bud na základě čistě teoretických, či fenomenologických přístupu, které se pokoušejí popsat experimentální výsledky. Korektnost těchto modelů je stále diskutabilní a její ověření je v současnosti předmětem intenzivní experimentální i teoretické činnosti. Výsledky analýzy měření dvoukrokových γ kaskád doprovázejících záchyt tepelného neutronu na jádru ^{176}Lu jsou porovnány s výstupy Monte Carlo simulace založené na předpokladu platnosti tzv. Extrémního Statistického Modelu. Porovnání výsledků zpracování experimentálních dat s výsledky získanými pomocí počítačových simulací se stává základním nástrojem studia korektnosti teoretických modelů. Námi analyzovaný experiment poskytuje informace zejména o $E1$ a $M1$ fotonové silové funkci, především pak o tzv. nůžkové rezonanci.

Klíčová slova: Fotonová silová funkce, Nůžková rezonance, Hustota jaderných stavů, Extrémní Statistický Model

Title: Photon strength functions in ^{177}Lu from two-step gamma cascade measurement
Author: Bc. Stanislav Valenta
Department: Institute of Particle and Nuclear Physics
Supervisor: Mgr. Milan Krtička, Ph.D.
Supervisor's e-mail address: krticka@ipnp.troja.mff.cuni.cz

Abstract: The subject of the study made in this work are photon strength functions. Many models, both based on theoretical as well as phenomenological approaches, were proposed for these quantities, describing the gamma decay of the nucleus, during last 50 year. However, the correctness of these models is still questionable and its verification is the subject of intensive experimental and theoretical activity at the present time. The results of the analysis of measurements of the two-step γ cascades following thermal neutron capture on the ^{176}Lu nucleus are compared with the outputs of the Monte Carlo simulations based on the validity of the so-called Extreme Statistical Model. Comparison of experimental data with outcomes of simulations thus becomes the basic tool for studying correctness of theoretical models. The experiment analyzed in the present work provides information mainly about $E1$ and $M1$ photon strength functions, especially about the so-called scissors resonance.

Keywords: Photon strength function, Scissors resonance, Level density, Extreme Statistical Model

Chapter 1

Introduction

In the present work we study the emission of photons from excited atomic nuclei which originate from non-relativistic nuclear reactions. Thanks to incredible complicated nuclear hamiltonian nobody is able to formulate the fundamental equations governing the γ-ray emission. Moreover we can safely assume that even if those equations were known solving them would be impossible thanks to their complexity. For those reasons we need to use simplified models such as description using *photon strength functions* (PSFs), also called γ-ray or radiative strength functions.

Introduced in 60's [1] PSFs are supposed to describe the process of the emission of photons from *highly* excited nuclei. To be more precise description using PSFs should be valid in the region of such excitation energy that nucleus radiates at so many frequencies making observation of single transitions impossible, i.e. one observes a "continuum spectrum". For that reason we predict some smooth, average properties of the γ-ray spectrum, not individual frequencies and the associated spectral intensities.

Various experiments can be (and have been) used to obtain information on photon strength functions. At first photonuclear experiments and slow-neutron capture reaction started the study of PSFs. Variety of other reactions have been used for last 30 years, namely both elastic and inelastic scattering of electrons, nucleons and photons at various energies, and also light- and heavy-ion induced fusion reactions. Many theoretical approaches have been introduced with aim to describe the photon strength functions.

The present work follows former and ongoing effort of authors from Faculty of Mathematics and Physics at Charles University in Prague and Nuclear Physics Institute of the ASCR to learn more about PSFs. To the results on various nuclei (e.g. ^{163}Dy, ^{168}Er, ^{160}Tb, ...) the contribution with those on ^{177}Lu is made. The PSFs are studied using data of photon deexcitation of nucleus following ther-

mal neutron capture. The other possible reaction channels - elastic neutron scattering - are of no importance for interaction of nucleus with thermal neutron. The neutron resonances (i.e. capturing states above the neutron threshold) are fairly narrow (the widths are up to tenths of eV) making the lifetime $\approx 10^{-14}$ s. That long lifetime coresponds to the fact that the projectile energy is shared among all other constituents - that is the Bohr's concept of compound nucleus [2] - making the decay mode of the compound nucleus independent on it's origin.

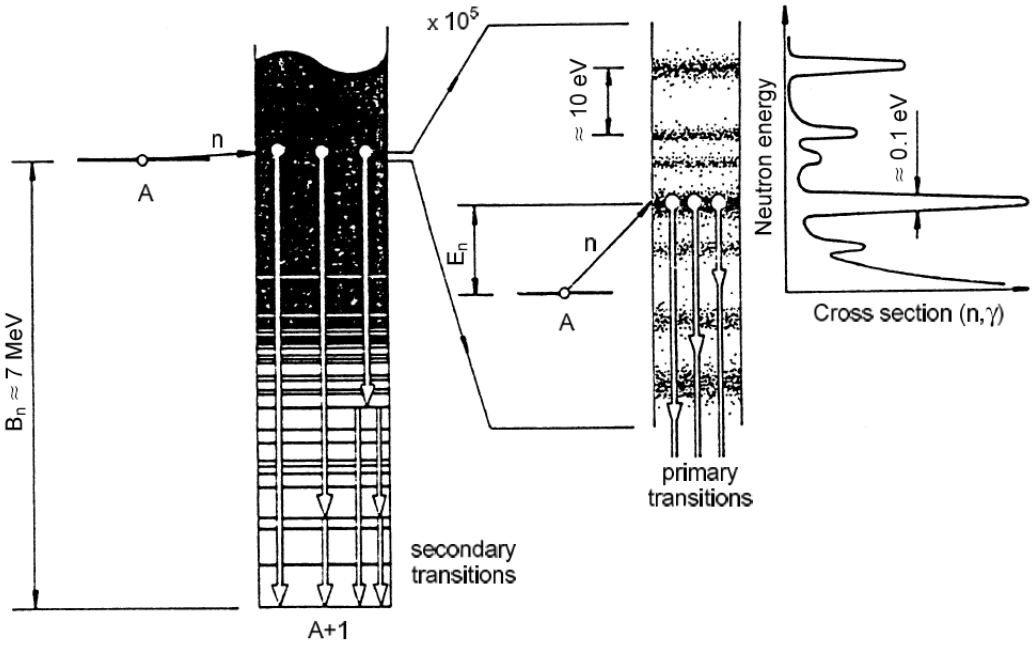

Figure 1.1: An illustration of (n,γ) interaction. The figure is taken from [50].

In Fig. 1.1 the schema of (n,γ) reaction is drawn. Thermal neutron with kinetic energy of $E_n \approx 0.02$ eV is captured on target nucleus with mass number A. The resulting nucleus with mass number $A + 1$ is highly excited with excitation energy being the sum of the neutron separation energy B_n and the neutron kinetic energy E_n. Typical value of the neutron separation energy is from 6 to 9 MeV, in our case 7.0724 MeV. The resulting $A + 1$ nucleus is a well-defined quantum mechanical state. Its decay begins with an emission of a primary γ quantum and proceeds by emission of secondary γ quanta until the nucleus ends up in the ground state.

The observed γ-ray spectrum is very complex thanks to the fact that the deexcitation of a medium-heavy or heavy nucleus proceeds throught a large number of levels. Such spectrum is dominanted by the lines corresponding to high-energy primary transitions and the secondary transitions between (few) low-lying levels. Besides these strong transitions there exist many weak and very weak lines be-

longing to less-energetic primary transitions and secondary transitions between levels at medium or high excitation energies that form the "continuous" component of spectrum. This "hidden part" of the spectrum is subject of our interest and study since it contains information on PSFs. Particularly helpful for purpose of extracting information on PSFs are coincidence measurements of the γ-ray spectrum. For that reason we investigate γ-ray spectra from measurements of two-step cascades (TSC) following thermal neutron capture performed at research reactor at Řež near Prague.

The experimental TSC spectra are compared with the spectra simulated using the Monte-Carlo based `DICEBOX` code. The simulations are based on the postulates of the so-called Extreme Statistical Model (ESM) that implicates various assumptions on the PSFs and level densities (LD). In spite of clear time consuming disadvantage of this approach it seems to have more positives than negatives compared to the "direct" iterative extraction of the shape and parameters of PSFs (and possibly LD). Those advantages are possibility to control the response of the detector system and all the involved fluctuations of statistical quantities.

In the next chapter the present experimental and theoretical status of photon strength functions as well as level density is briefly summarized. Chapter 3 contains description of the coincidence experiment that produced experimental data processed in this work and the `DICEBOX` algorithm used to simulate TSC spectra. Then in Chapter 4 the experimental data are analyzed and compared with various outcomes of simulations. Finally main conclusions of the present work are summarized in Chapter 5.

Chapter 2

Photon strength functions and level density

2.1 Level density

Individual levels with all their characteristics (spin, parity, decay properties, ...) are known experimentaly up to certain energy, in case of studied nucleus ^{177}Lu about 1 MeV. The levels can be measured there because the energy spacing between them is big enough (i.e. level density is sufficiently low). There exists one additional region where individual levels can be observed. Those are the few resonances of certain spin in small energy range just above the neutron separation energy. Experimental technique used for this purpose is so called the neutron time-of-flight method. To describe the remaining intervals of excitation energy, we need to rely on statistical models.

The formula for nuclear level-density derived by Bethe in 1936 [3] raised purely on statistical approach. Using the idea that the complete information on the spectrum of a system is equivalent to the knowledge of the partition function of the system. Concidering a gas of noninteracting fermions with equally spaced nondegenerated single particle levels with fixed spin Bethe obtainded for density ρ at excitation energy E

$$\rho(E) = \frac{\exp(2\sqrt{aE})}{4\sqrt{3}E}, \tag{2.1}$$

where a is so called level density parameter.

More realistic Back-Shifted Fermi Gas (BSFG) formula [4] takes into account the fact that two types of fermions with tendency to form pairs are present in nucleus. Extra energy is needed to separate such pair, introducing this energy is

done by energy shift Δ with final formula being

$$\rho(E,J) = f(J)\frac{\exp\left(2\sqrt{a(E-\Delta)}\right)}{12\sqrt{2}a^{\frac{1}{4}}(E-\Delta)^{\frac{5}{4}}}, \tag{2.2}$$

where $f(J)$ is the spin distribution factor. Assuming the gaussian distribution of spin projections M, $f(J)$ is equal to [5]

$$f(J) = \exp\left(-\frac{J^2}{2\sigma_c^2}\right) - \exp\left(-\frac{(J+1)^2}{2\sigma_c^2}\right) \approx \frac{2J+1}{2\sigma_c^2}\exp\left(-\frac{(J+1/2)^2}{2\sigma_c^2}\right), \tag{2.3}$$

where σ_c is the spin cut-off parameter which can be according to [5] expressed as

$$\sigma_c^2 = k\sqrt{a(E-\Delta)}A^{\frac{2}{3}}. \tag{2.4}$$

The constant k was proposed to be 0.0888 in [5], later parametrization [6] suggested 0.1146. Later, another formulas were suggested to describe spin cut-off parameter. In our work we use the formula proposed in [9]

$$\sigma_c^2 = 0.0146\frac{1+\sqrt{1+4a(E-\Delta)}}{2a}A^{\frac{5}{3}}. \tag{2.5}$$

Systematic deviation from theoretical spin distribution formula (2.3) may occur in some nuclei, for futher information see [7, 8].
The parameters a and Δ in formula (2.2) are unique for each nucleus. One can adjust them to reproduce level density at low energies as well as at the resonance region above the neutron separation energy.

Gilbert and Cameron [5] have proposed another formula, which sufficiently well describes the low-energy behaviour of level density

$$\rho(E,J) = \frac{f(J)}{T}\exp\left(\frac{E-E_0}{T}\right). \tag{2.6}$$

The two parameters E_0 and T - the nuclear temperature - in this so-called *Constant Temperature Formula* (CTF) are again unique for each nucleus and can be obtained from fitting the formula to above-mentioned experimental data. Within this approach the spin cut-off parameter entering the formula (2.6) via $f(J)$ is taken independent on excitation energy in simple form [10]

$$\sigma_c = (0.98 \pm 0.23)A^{(0.29\pm0.06)}. \tag{2.7}$$

Gilbert and Cameron also distinguish two regions of excitation energies. For low-energy region the CTF model is used, above certain energy (typical value is in range 4-6 MeV) the level density is described by BSFG formula. In some other

works [9] it is suggested that the CTF formula may be a good approximation for entire excitation energy region up to neutron separation energy. We adopted this approach in our simulations. Naturally, other models of the level density exist but they are not used in the present work. Recently von Edigy and Bucurescu introduced the form of the spin cut-off parameter that can be used in both BSFG and CTF formula [13]:

$$\sigma^2 = 0.391A^{0.675}(E - 0.5Pa')^{0.312}, \tag{2.8}$$

with re-evaluated level-density parameters (a, Δ and E_0, T respectively). Pa' is the deuteron pairing energy calculated from mass or mass excess values $M(A, Z)$ of the mass tables [12] with formula:

$$Pa' = \frac{1}{2}[M(A+2, Z+1) - 2M(A, Z) + M(A-2, Z-1)] \tag{2.9}$$

For futher details see [13]. Both BSFG and CTF models work with the assumption of parity independence of level density. This dependence cannot be a priori excluded. On the other hand it is supposed to be negligable above few MeV of excitation energy in spherical nuclei [14, 15]. Futhermore this dependence vanishes more quickly with a deformation of nuclei. There are indirect experimental tests of level density. The first kind of experiment is based on analysis of shapes of neutron evaporation spectra from variously induced (p,n,α) reactions within the Hauser-Feshbach statistical approach. It allows determination of absolute values of level density and gives a reasonable agreement with BSFG formula for wide variety of nuclei [16, 17]. Known exceptions are several closed-shell nuclei with $A \approx 208$ giving better agreement with CTF formula. In addition the level density can be extracted from primary γ-ray spectrum following the (^{3}He,$\alpha\gamma$) and (^{3}He,^{3}He' γ) reactions in rare-earth region using the algorithm known as "Oslo method" [18, 19, 20]. The method used does not provide absolute values of the level density but information about the shape of the level density energy dependence. The rest of analysis is performed using the above mentioned regions (low excitation energy and neutron resonances). For rare earth nuclei there is a remarkable agreement with BSFG shape. In Fig. 2.1 the level density energy dependence of models used in this work is ploted.

2.2 Photon strength functions

The partial γ-decay width from an initial state α with spin J_α to final state β with spin J_β through the emission of a photon of type X, multipolarity L and energy $E_\gamma = E_\alpha - E_\beta$ is given by formula

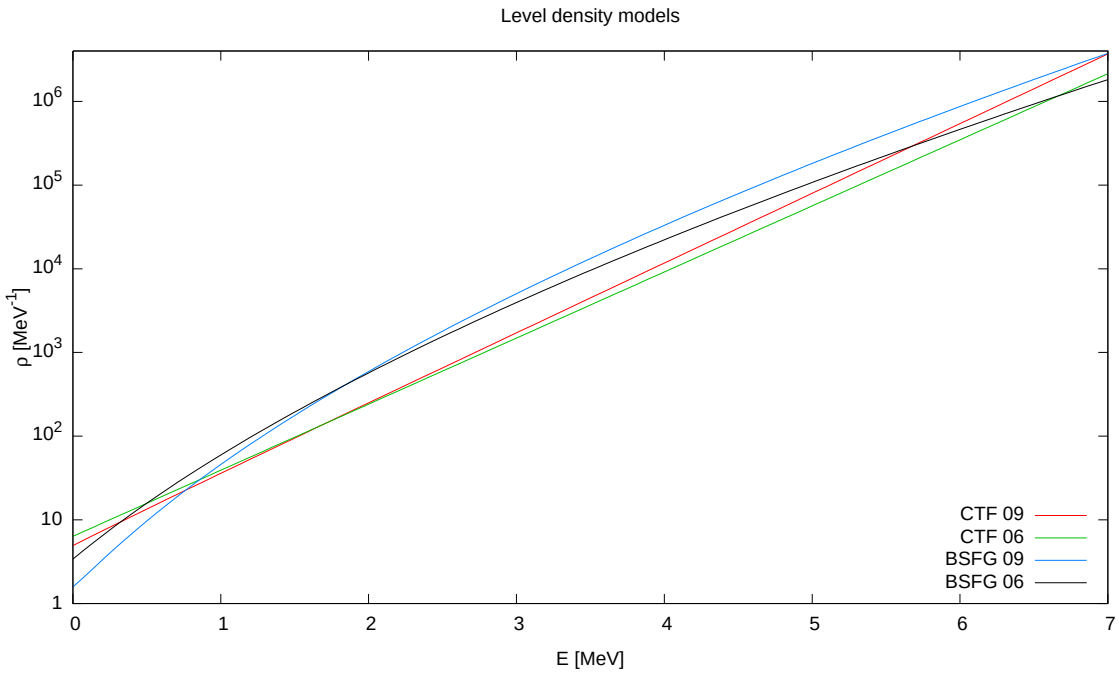

Figure 2.1: The energy dependence of level density. The plotted curves correspond to tested models summed over half-integral spins of our interest, that is $\frac{7}{2} + \frac{9}{2} + \ldots + \frac{17}{2}$. The label "06" denotes the spin cut-off parameter in the form (2.5) and (2.7) for the BSFG and the CTF formula respectively. The spin cut-off parameter (2.8) is used in the level densities marked "09".

$$\Gamma^{(XL)}_{\alpha\gamma\beta} = \frac{8\pi(L+1)}{L[(2L+1)!!]^2}\left(\frac{E_\gamma}{\hbar c}\right)^{2L+1} B(XL)\downarrow, \tag{2.10}$$

where $B(XL)\downarrow$ stands for the reduced transition probability of deexcitation of the nucleus

$$B(XL)\downarrow = \frac{2J_\beta+1}{2J_\alpha+1}B(XL)\uparrow = \frac{1}{2J_\alpha+1}|\langle\alpha J_\alpha\|\mathcal{H}^{(XL)}\|\beta J_\beta\rangle|^2. \tag{2.11}$$

$B(XL)\uparrow$ stands for the reduced transition probability of photoexcitation, $\mathcal{H}^{(XL)}$ is the electromagnetic transition operator of type X and multipolarity L. Once the level density is significantly high it is convenient to use average partial radiation width and relate it to a function $f^{(XL)}$ which is called photon strength function

$$\bar{\Gamma}^{(XL)}(\alpha \to \beta) = \frac{f^{(XL)}E_\gamma^{2L+1}}{\rho(\alpha)}. \tag{2.12}$$

In the single-particle approach the $f^{(XL)}$ is assumed to be constant, i.e. does not depend on transition energy $E_\alpha - E_\beta$.

Numerical relations between reduced transition probabilities, $B(XL)\downarrow$, and photon strength functions, $f^{(XL)}$, can be obtained using (2.10) and (2.12). For lowest multipolarity transitions we get

$$\frac{1}{\Delta}\sum_{\Delta} B(E1)\downarrow [e^2fm^2] = 0.95510^6 f^{(E1)}[MeV^{-3}] \tag{2.13}$$

$$\frac{1}{\Delta}\sum_{\Delta} B(M1)\downarrow [\mu_N^2] = 86.610^6 f^{(M1)}[MeV^{-3}] \tag{2.14}$$

$$\frac{1}{\Delta}\sum_{\Delta} B(E2)\downarrow [e^2fm^4] = 1.2510^{12} f^{(E2)}[MeV^{-5}] \tag{2.15}$$

for deexcitation going to the zero-spin ground state. The summations on the left hand sides run over an energy interval Δ.

Using the detailed-balance principle one can derive a relation between the partial radiation width $\Gamma^{(XL)}_{\alpha\gamma\beta}$ of the γ transition in (2.10) and the XL component of the photoabsorption cross section $\sigma^{(XL)}_{\beta\gamma\alpha}$

$$\Gamma^{(XL)}_{\alpha\gamma\beta} = \frac{E_\gamma^2}{(\pi\hbar c)^2}\frac{2I_\beta+1}{2I_\alpha+1}\sigma^{(XL)}_{\beta\gamma\alpha}. \tag{2.16}$$

This leads to alternative definition of photon strength function $f^{(XL)}$

$$f^{(XL)}(E_\gamma) = \frac{1}{(\pi\hbar c)^2}\frac{\bar{\sigma}^{(XL)}_{tot}(E_\beta \to E_\alpha)}{(2L+1)E_\gamma}, \tag{2.17}$$

using assumption that photoabsorption cross section does not depend on the properties (excitation energy, spin, parity) of the initial (β) state. Additional assumption, known as *Brink hypothesis* [21], is usually made. It says that the average photoabsorption cross section from any level β does depend only on transition energy $E_\gamma = E_\alpha - E_\beta$ and not on other properties of the level. The hypothesis was originaly suggested for $E1$ transitions but it can be modified for any type and multipolarity of the radiation. The Brink hypothesis is visualized in Fig. 2.2. Nowadays it seems that such a strict Brink hypotesis is too strong simplification of the reality. It seems that PSF does depend not only on the photon energy but also on other characteristics of the final (β) state.

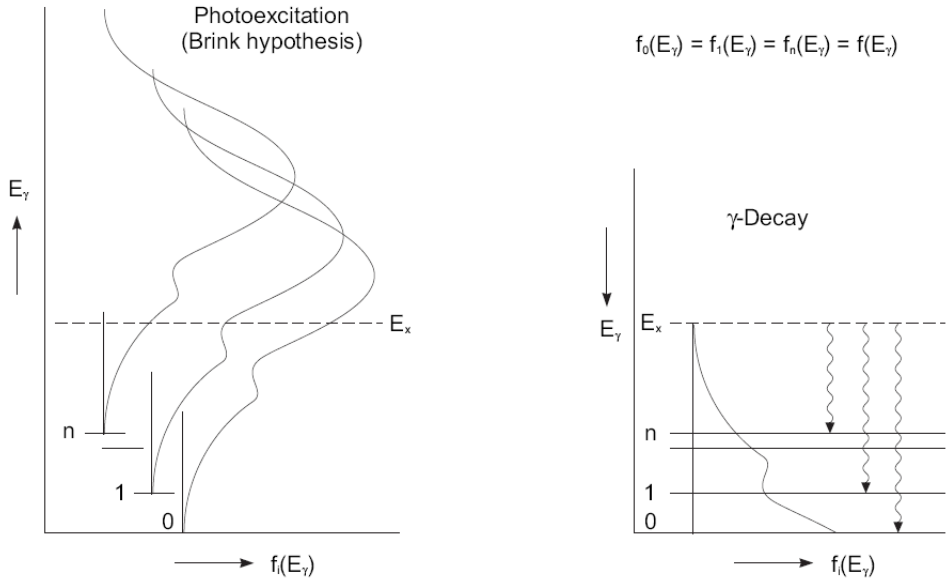

Figure 2.2: The Brink hypothesis for photoexcitation and γ-decay following neutron capture reaction. The figure is taken from [50].

2.2.1 Fluctuation properties of partial radiation widths

Looking closely at the fluctuation properties of the partial radiation widths $\Gamma^{(XL)}_{\alpha\gamma\beta}$ they are assumed to fluctuate strongly, according to the Porter-Thomas (P-T) distribution (see original article [69] or more detailed description in [50])

$$P(x)dx = \frac{1}{\sqrt{2\pi x}} e^{-\frac{x}{2}} dx, \tag{2.18}$$

where $x = \Gamma_{\alpha\gamma\beta}/\bar{\Gamma}_{\alpha\gamma\beta}$ and $\bar{\Gamma}_{\alpha\gamma\beta}$ is the average radiation width for the transition from initial state α to final state β. Note should be made that P-T distribution is actually a χ^2 distribution with the number of degrees of freedom $\nu = 1$.

2.2.2 $E1$ photon strength function

By measuring photoabsorption cross section above neutron separation energy Baldwin and Kleiber [22] found a wide resonance. This resonance was actually predicted few years earlier [23] and was interpreted as a consequence of colective vibrations of proton and neutron fluids. This motion has dipole character hence the name *giant dipole electric resonance* (GDER). To describe the GDER existence one can use classical models of motion. If proton and neutron fluids vibrate within a fixed nuclear surface Fig. 2.3 a) the restoring force is proportional to the density gradient

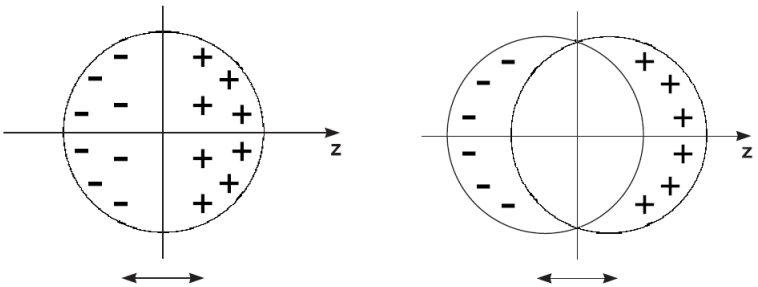

Figure 2.3: Models of possible GDER motions. The figure is taken from [50].

of those fluids [23, 24] making the center of resonance dependence $E_G \approx A^{-\frac{1}{3}}$. Assuming the vibrations of incompressible proton and neutron spheres against each other, see Fig. 2.3 b) the restoring force is proportional to the nuclear surface area [25], so the center of resonance shifts as $E_G \approx A^{-\frac{1}{6}}$. The position of the resonance is well approximated by $E_G = 31.2A^{-\frac{1}{3}} + 20.6A^{-\frac{1}{6}}$, which suggests that the real GDER is probably mixture of two described models.

The experimental data from (γ, n) reactions clearly show that the shape of the GDER is well described by Lorentzian shape near the maximum of the resonance which is about 15 MeV. Our region of interest is under the neutron separation energy, i.e. on the low-energy tail of the resonance. It is not quite sure if the Lorentzian extrapolation is valid also for energies well below the maximum of the resonance. The *Brink-Axel* model is the most frequently used model of $E1$ PSF. Assuming the Lorentz form of $\bar{\sigma}_{tot}^{(XL)}(E_\gamma)$ in (2.17) the PSF formula reads

$$f_{BA}^{(E1)}(E_\gamma) = \frac{1}{3(\pi\hbar c)^2} C_\Sigma \frac{E_\gamma \Gamma_G}{(E_\gamma^2 - E_G^2)^2 + E_\gamma^2 \Gamma_G^2}, \tag{2.19}$$

where E_G is the center and Γ_G halfwidth of the resonance, both usually expressed in MeV. The normalization constant C_Σ can be obtained by fitting the photonuclear data and is expressed in form

$$C_\Sigma = \sigma_G \Gamma_G, \tag{2.20}$$

where σ_G is the cross section in the maximum of resonance usually expressed in mb. The shape (2.19) of PSF describes well the photonuclear data around the maximum of GDER, that is at energies $E_\gamma \geq 10$ MeV.

In fact when dealing with a nuclei with a static quadrupole deformation, the GDER splits, so the $E1$ PSF is represented by incoherent superposition of two resonances described by (2.19) with two sets of parameters E_G, Γ_G and σ_G. This splitting can be described using hydrodynamical model - the oscillations of nuclei

surface govern the shape of giant resonance. The intensities of two modes - oscillations along and perpendicular to the symmetry axis - are expected to be in ratio 1 : 2. That is indeed supported by photonuclear data.

The analysis of intensities of primary transitions in (n,γ) reaction leads to conclusion that the simple BA model (2.19) is inadequate for spherical nuclei. For deformed nuclei this contradiction was not observed.

Another model we use for $E1$ PSF is so called *KMF* model. It was proposed by S.G. Kadmenskij, V.P. Markushev and V.I. Furman in 80's. Within the framework of semi-microscopic shell-model approach using the theory of finite Fermi systems the formula for $f^{(E1)}$ in spherical nuclei was derived [26]

$$f^{(E1)}_{KMF}(E_\gamma, T_f) = \frac{1}{3(\pi\hbar c)^2} F_K \sigma_G \Gamma_G \frac{E_G \Gamma_G(E_\gamma, T_f)}{(E_\gamma^2 - E_G^2)^2}, \tag{2.21}$$

where the damping width $\Gamma_G(E_\gamma, T_f)$ depends on nuclear temperature T_f as

$$\Gamma_G(E_\gamma, T_f) = \frac{\Gamma_G}{E_G^2}(E_\gamma^2 + 4\pi^2 T_f^2). \tag{2.22}$$

the nuclear temperature T_f of a nuclear state at excitation energy E_f is [26]

$$T_f = \sqrt{\frac{E_f - \Delta_p}{a}}, \tag{2.23}$$

where a is level-density parameter from (2.2) and Δ_p is a pairing correction, see [27]. The authors [26] recommended the factor $F_k \approx 0.7$.

The KMF model is supposed to describe the $E1$ PSF only in low-energy region ($E_\gamma \ll E_G$) since formula (2.21) diverges at $E_\gamma = E_G$ making any prediction in GDER region meaningless. The comparison of predictions by KMF model with experimental intensities of $E1$ primary transitions to low-energy states in (n,γ) reactions gives reasonable agreement in spherical nuclei but it underestimates the strength in well deformed nuclei [28, 29].

In order to describe the $E1$ PSF in both low-energy and GDER energy region in spherical nuclei the so-called generalized Lorentzian was proposed [30]

$$f^{(E1)}_{GLO}(E_\gamma, T_f) = \frac{1}{3(\pi\hbar c)^2} \sigma_G \Gamma_G \left[\frac{E_\gamma \Gamma_G(E_\gamma, T_f)}{(E_\gamma^2 - E_G^2)^2 + E_\gamma^2 \Gamma_G^2(E_\gamma, T_f)} + F_K \frac{4\pi^2 T_f^2 \Gamma_G}{E_G^5} \right]. \tag{2.24}$$

The first term in brackets, similar to that in Eq. (2.19), provides agreement with (γ,n) experimental data near the maximum of GDER. Futhermore this formula has a similar properties as KMF, Eq. (2.21), for low energies thanks to the second term. The most important property is a non-zero limit for $E_\gamma \to 0$ (if $T_f \neq 0$).

This feature is desired since experimental data on ^{143}Nd(n,$\gamma\alpha$) reaction suggest such a behaviour [31]. Latter analysis with significantly better statistics [32] led to the conclusion that the low-energy $M1$ transitions dominate over $E1$. As a consequence the experimental confirmation of the finite limit of $E1$ PSF for $E_\gamma \to 0$, $T_f \neq 0$ remains open.

A phenomenological modification of the damping width (2.22) was proposed [33] to achieve better agreement in case of deformed nuclei. Aditional empirical enhancement factor k_0 enters the damping width $\Gamma_G(E_\gamma, T_f)$

$$\Gamma_G(E_\gamma, T_f) = \left[k_0 + \frac{E_\gamma - E_{\gamma 0}}{E_G - E_{\gamma 0}}(1 - k_0)\right] \frac{\Gamma_G}{E_G^2}(E_\gamma^2 + 4\pi^2 T_f^2), \tag{2.25}$$

which is of course reduced to (2.22) for $k_0 = 1$. For $k_0 > 1$ $\Gamma_G(E_\gamma, T_f)$ is enhanced at $E_\gamma = E_{\gamma 0}$ compared to value given by Eq. (2.22). Authors [34, 35] recommend $E_{\gamma 0} \approx 4.5$ MeV. The enhancement was determined by adjusting set of calculated average total radiation widths $\bar{\Gamma}_\gamma$, energy dependences of (n,γ) reaction cross section and γ-ray spectra from the (n,γ) reaction for medium-heavy and heavy nuclei. The value of k_0 as a function of mass number A differs for each level density model, for futher details see [35]. For BSFG formula (2.2) k_0 is given as

$$k_0(A) = \begin{cases} 1.0 & \text{pro} \quad A < 148 \\ 1.0 + 0.09(A - 148)^2 \exp[-0.18(A - 148)] & \text{pro} \quad A \geq 148 \end{cases}, \tag{2.26}$$

while for CTF-like formula proposed in [36]

$$k_0(A) = \begin{cases} 1.5 & \text{pro} \quad A < 145 \\ 1.5 + 0.131(A - 145)^2 \exp[-0.154(A - 145)] & \text{pro} \quad A \geq 145 \end{cases}. \tag{2.27}$$

Using $\Gamma_G(E_\gamma, T_f)$ in form from Eq. (2.25) in (2.19) (and replacing Γ_G^2 in numerator by combination $\Gamma_G.\Gamma_G(E_\gamma, T_f)$) one gets so-called *enhanced Lorentzian with energy dependent width* model (EELO). Doing the same in (2.24) we obtain *enhanced generalized Lorentzian* model(EGLO).

The resonances build above the certain states E_f as predicted by $f^{(E1)}$ models used in our study are ploted in Fig. 2.4. Using obvious relation $E_f = E_i - E_\gamma$ in Eq. (2.23) the PSF becomes parametrized by the energy of initial state E_i and thus has physical meaning for $E_\gamma \leq E_i$. As in our case the nucleus decays, this is the quantity of our interest, see Fig. 2.5. The parameters of splitted GDER were taken as $E_G = 12.32$ MeV; $\Gamma_G = 2.57$ MeV; $\sigma_G = 217$ mb and $E_G = 15.47$ MeV; $\Gamma_G = 4.70$ MeV; $\sigma_G = 287$ mb from experimental fit to (γ,n) data [37]. To test EELO and EGLO models we set $E_{\gamma 0} = 4.5$ MeV and $k_0 = 1.4$, resp. 2.8 for BSFG, resp. CTF level density formula using formulae (2.26), resp. (2.27).

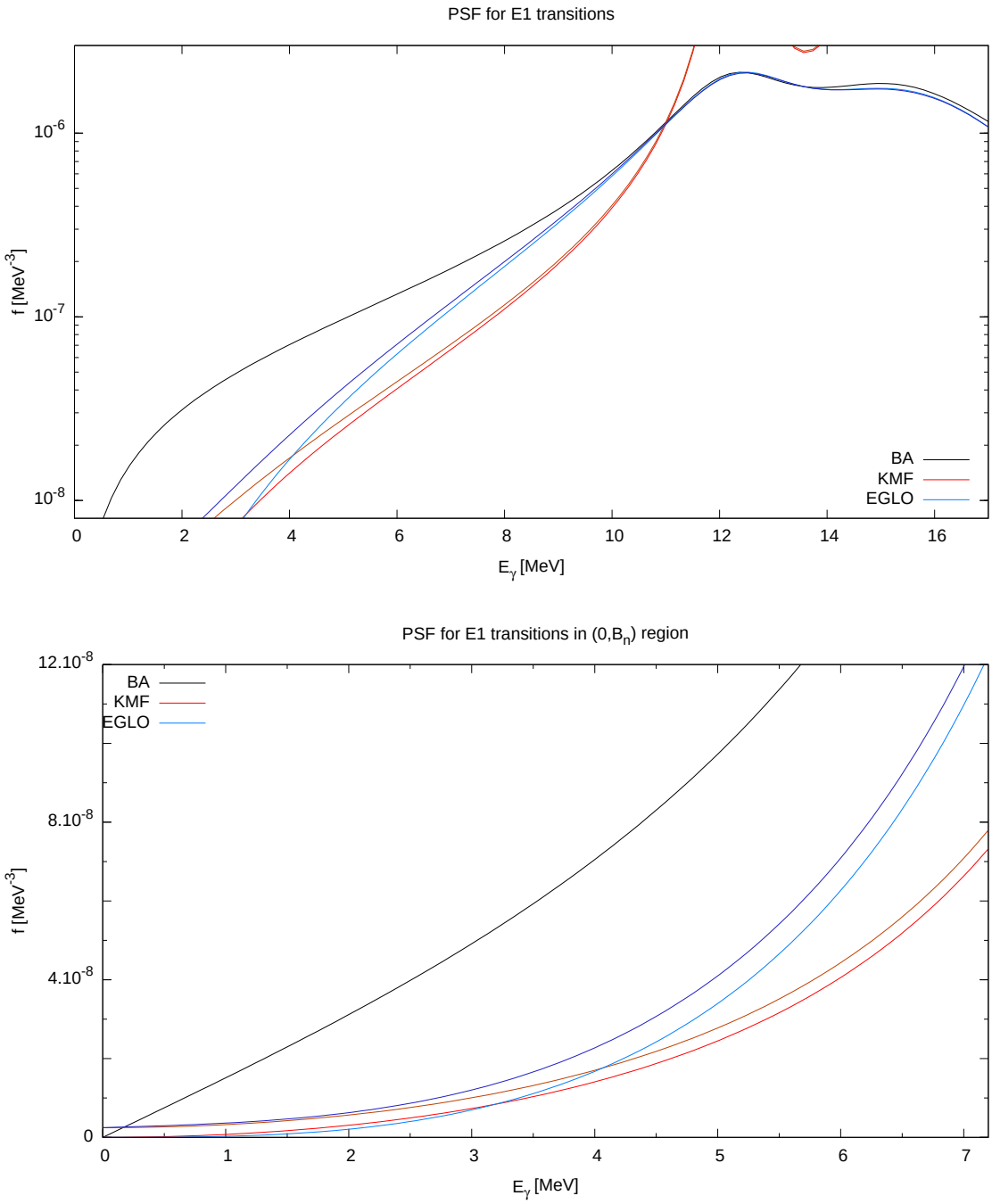

Figure 2.4: The models of E1 PSF used in the present work. Since the KMF and EGLO models depend on the energy of final state E_f, see Eq. (2.23), the dependence is shown for two energies $E_f = 0$ and 2 MeV (the upper, darker lines correspond to 2 MeV).

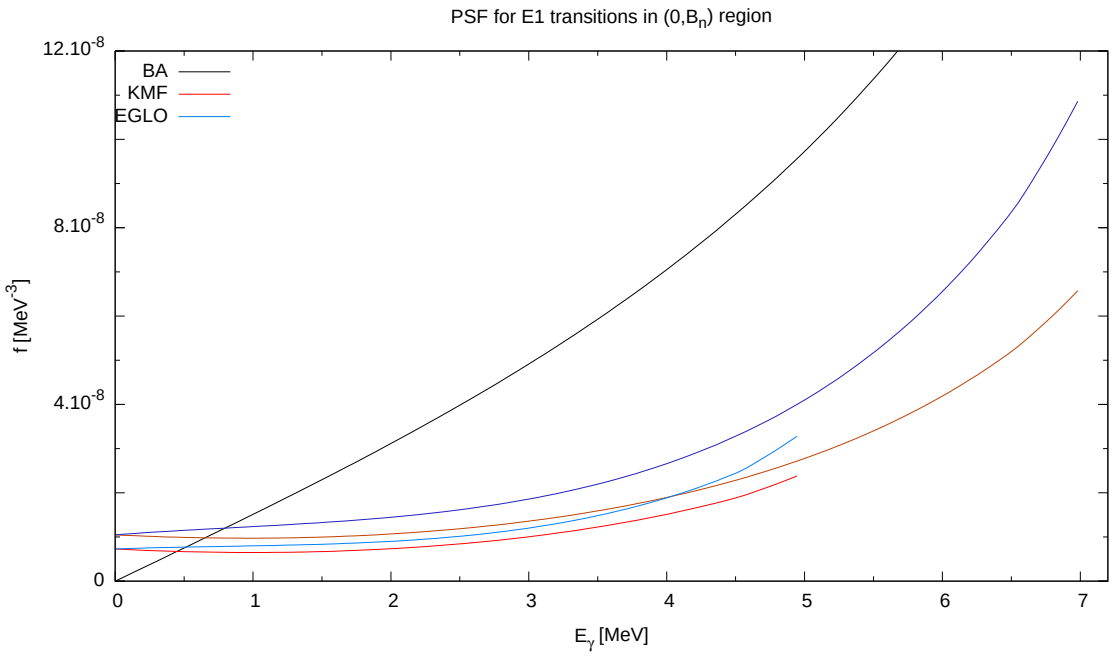

Figure 2.5: The models of E1 PSF used in the present work parametrized by the energy of initial state. The BA model remains the same since it exhibits no temperature dependence. The energies of initial states are (i) 7 MeV – close to the capturing state, the upper, darker lines and (ii) 5 MeV.

The fact that GDER is a general feature of nuclei up to excitation energy of several hundred MeV was proved by measurements of radiative capture of light and heavy ions. Another remarkable conclusion from these experiments is that the position of GDER remains very stable even above highly excited nuclear states, the dependence on excitation energy is negligable. This conclusion strongly supports Brink hypothesis in its most general formulation.

On the other hand experimental information about $E1$ PSF in our region of interest, that is $E_\gamma < B_n$, is not that satisfactory. Apart from the above mentioned data on intensities of primary transitions in (n,γ) reactions one can rely on measurements of (γ, γ') reactions for excitation energies $E_\gamma \approx 2 - 4$ MeV [38] and lately on data from (^{3}He,$\alpha\gamma$) and (^{3}He,^{3}He' γ) experiments [18, 19, 39].

2.2.3 $M1$ photon strength function

Relevant experimental information about $M1$ photon strength function above particle emission threshold is suppressed due to dominance of $E1$ transitions. This fact is not crucial for our work since only the information for energies up to about neu-

tron separation energy B_n is needed. In this range the experimental information about $M1$ PSF is comparable to that about $E1$ PSF. Various experiments were performed to obtain information on $M1$ PSF, namely study of γ-ray emission following the slow neutron capture and inelastic scattering of protons, electrons and photons on nuclei.

The simplest approximation of $M1$ PSF is single particle model (SP) - $f_{SP}^{(M1)}$ is independent on transition energy. To estimate the value of $f_{SP}^{(M1)}$ by measuring total intensities of primary γ transitions following resonance capture of neutrons one needs to deal with Porter-Thomas fluctuations. To supress this effect partial radiation widths of transitions from neutron capturing state to low energy state needs to be averaged over sufficiently high number of neutron resonances. The intensities of γ transitions observed in so-called average resonance neutron capture (ARC) need to be properly normalized. This is achieved by averaging the partial radiation widths determined for each resonance by combination of the neutron time-of-flight and standart γ-spectroscopy methods [40]. The most important conclusion from ARC data is the value of ratio $f^{(E1)}/f^{(M1)}$ at energy $E_\gamma \approx 7$ MeV

$$f^{(E1)}/f^{(M1)} = 7 \pm 1, \tag{2.28}$$

that is valid for most nuclei with $A \geq 100$ [40].

Single particle model is probably too simple. It has been found that resonance structure similar to GDER (but weaker) are probably present also in $M1$ PSF. The structure known for the longest time is so-called spin-flip resonance (SF). The investigation using inelastic scatering of protons with kinetic energy $T_p = 200$ MeV on medium-heavy and heavy nuclei led to determination of parameters of SF. In deformed nuclei the centers of found double-humped structure shift as $\approx 34A^{-\frac{1}{3}}$ and $\approx 44A^{-\frac{1}{3}}$ [41]. Analyzing some of the ARC data authors [43, 44] proposed the spin-flip mode centered at $E_{SF} \approx 41A^{-\frac{1}{3}}$ with width $\Gamma_{SF} = 4$ MeV for nuclei with $A \approx 105$. When we use spin-flip mode in present work the shape of the resonance is assumed in form given in Eq. (2.19). The center of the resonance follows the formula proposed by [43] $E_{SF} = 7.3$ MeV, width is set to $\Gamma_{SF} = 3$ MeV and cross section is adjusted to $E1$ model used to satisfy the condition (2.28), that is $\sigma_{SF} = 2.0$ mb, 0.8 mb and 1.3 mb for BA, KMF and EGLO models respectively.

In the middle of the 80's the inelastic scattering experiments using electron beams on deformed rare-earth nuclei confirmed the existence of colective $M1$ mode [45] that was theoreticaly predicted in late 70's to occure in deformed nuclei. A simple geometrical Two-Rotor-Model (TRM) used by authors [46] expects the $M1$ mode represented by a scissors-like counterrotation of the proton vs the neutron fluid. This mode is usually called the *scissors mode* (SC) for evident reasons. Futher theoretical and experimental investigation on many rare-earth nuclei determined the center of SC $E_{SC} \approx 3$ MeV. The reaction (γ, γ') aka nuclear

resonance flourescence (NRF) turned out to be the powerful tool for scissors mode investigation since it's highly sensitive and selective to the low-lying dipole excitations. Using NRF an important fragmentation of the photon strength was found around 3 MeV i.e. in the interval of SC dominance [38]. These data also revealed the dependence of the total strength of the SC mode on the deformation parameter squared δ^2. The energy center E_{SC} of the SC mode was proposed [47] to follow the formula deduced from NRF data

$$E_{SC} = 13.4\sqrt{1+9\delta^2}A^{-\frac{1}{3}} \tag{2.29}$$

As the δ parameter is ≈ 0.1 for investigated nucleus ^{177}Lu we have started our simulations with $E_{SC} = 3.2$ MeV.

Total strength of the SC mode observed in (γ,γ') experiments on well-deformed even-even rare-earth nuclei is approximately $3\mu_N^2$. In these nuclei the SC mode strength is distributed over few states in energy range of 400 - 500 keV. For odd and odd-odd nuclei the observed strength is usually smaller thanks to higher level density which does not allow to observe all the transitions in NRF experiment.

The resonance structure centered at $E_\gamma = 3$ MeV was also observed in analysis of two step γ-cascades (TSC) following thermal neutron capture on deformed ^{163}Dy nucleus [48, 49]. The resonance in $M1$ PSF was postulated in the form of Lorentzian (2.19) yielding the mean value of the parameters $E_{SC} = 3.0$ MeV, $\Gamma_{SC} = 0.6$ MeV and $\sigma_{SC} = 0.9$ mb. Total strength of the SC mode observed in this analysis was established $\approx 6\mu_N^2$. Note should be made that the TSC experiment, contrary to the NRF measurements provide the strenght not only for the ground state but for excited states as well. The Brink hypothesis can thus be tested using these results.

Similar observation of the resonance at energy $E_\gamma \approx 2.5-3$ MeV gave analysis of γ-ray spectra in neutron capture experiments on deformed nuclei using higher neutron energies, specifically 10-800 keV [56, 59] and 0.5-3.0 MeV [58]. Stability (i.e. independence of the center of resonance on incident neutron energy) of resonance confirms that observed resonance is due to shape of photon strength function not the shape of level density.

From results [18, 19, 39] on reactions (^{3}He,$\alpha\gamma$) and (^{3}He,^{3}He' γ) on deformed nuclei similar strength of scissors resonance was deduced as in (n,γ) experiments. But the halfwidth obtained by analysis in these experiments is typically $\Gamma_{SC} \geq 1.0$ MeV contrary to smaller widths of (γ,γ') and TSC experiments. Similar variance holds for value of cross section in maximum of resonance: experiments with helium probes estimate $\sigma_{SC} = 0.5$ mb [57], fast neutron experiments $\sigma_{SC} \approx 0.2-0.4$ mb [56]. Futher analysis of the TSC data on other nuclei didn't restrict the cross section that much leaving possible interval $\sigma_{SC} = 0.2-1.0$ mb [48, 49, 51]. Futhermore the NRF and TSC experiments provide the center of resonance ≈ 3.0 MeV contrary to fast-neutron and ^{3}He induced reactions with result

$\approx$ 2.6 MeV for $A \approx 160$ nuclei. The strict form of Brink hypothesis was applied in all mentioned analyses for practical reasons.

The shapes of $M1$ PSF (together with some $E1$ for comparsion) used in present work are plotted in Fig. 2.6. As the parameters of the SC mode are subject of our study and adjustment, the shorthand notation is used in the form $(E_{SC};\Gamma_{SC};\sigma_{SC})$ in the present work.

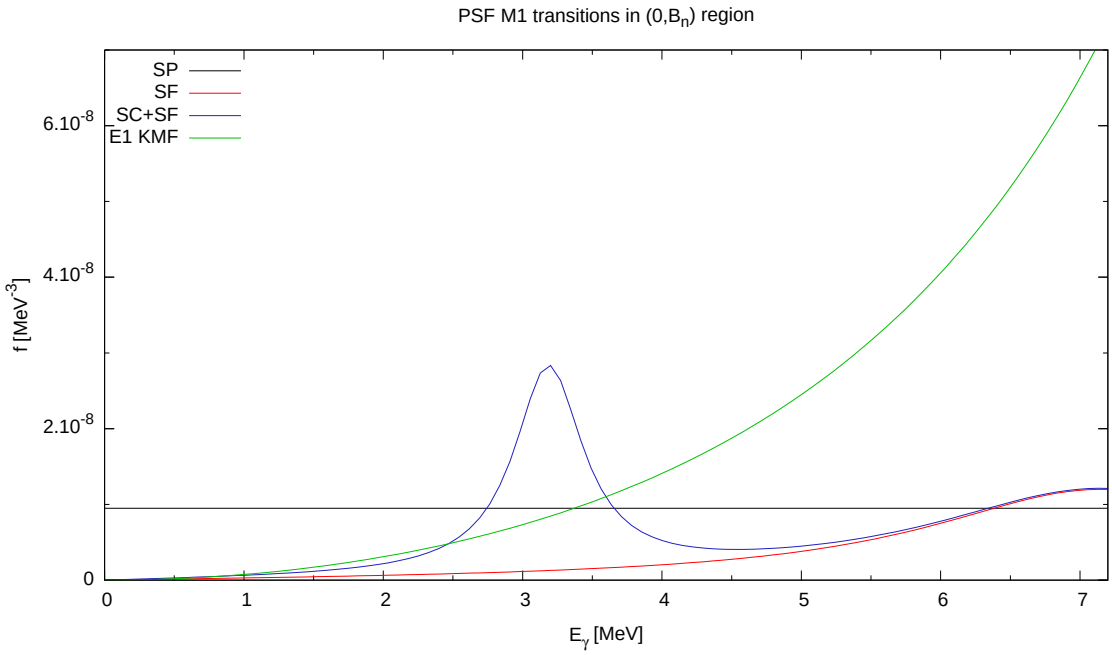

Figure 2.6: The models of M1 PSF used in the present work. The KMF model for E1 PSF is plotted for comparsion. Note that the M1 strength is adjusted to fulfil the condition (2.28). The parameters of SC mode are (3.2;0.6;1.0). Note that the height of SC resonance is lineary proportional to the σ_{SC}.

2.2.4 $E2$ photon strength function

In addition to the dipole transitions also the electric quadrupole transitions might give an observable contribution to the statistical part of γ-ray spectra that result from compound nucleus reactions. Considering the decay of excited nucleus with low spin we expect minor contribution from these transitions.

The cross section of inelastic scattering of charged particles contains multipole matrix elements [55] making such reactions main source of information on $E2$ strength. In early 70's the resonance characted of $E2$ strengths was observed

in inelastic scattering of electrons, protons and α particles on nuclei, see [44] and references therein. Interpreted as isoscalar *giant quadrupole electric resonance* (GQER) this behaviour is macroscopically understood to be induced by surface oscillation of neutrons moving together with protons. The energy center of GQER following the formula $E_{\mathrm{GQER}} = 63A^{-\frac{1}{3}}$ [54] almost overlaps with the energy center of GDER. Authors in [53] proposed formulas for damping width Γ_{GQER} and cross section at the maximum of GQER σ_{GQER}: $\Gamma_{\mathrm{GQER}} = 6.11 - 0.012A$ MeV, $\sigma_{\mathrm{GQER}} = 1.5\ 10^{-4} Z^2 E_R^2 A^{-\frac{1}{3}}/\Gamma_{\mathrm{GQER}}$ mb, where both E_{GQER} and Γ_{GQER} needs to be given in MeV.

In (n,γ) reactions (thermal neutron capture and resonance capture) only few (tens) primary transitions of $E2$ type were observed so far [52, 53]. Such a tiny sample of individual $E2$ transitions with biased intensities towards higher values (effect caused by P-T fluctuations) makes the estimation of the $E2$ photon strength problematic. It is save to say that average partial radiation widths of $E2$ primary transitions estimated from (n,γ) reaction are suppressed by almost two orders of magnitude to those of $E1$ type. The $E2$ photon strength function is often approximated by single-particle model, i.e. $f_{SP}^{(E2)} = \mathrm{const}$. The available experimental data don't contradict neither one. In the present work we use both models, i.e. SP and GQER, the single particle strength is taken as $f_{SP}^{(E2)} = 10^{-10}\ \mathrm{MeV}^{-5}$. The shape of the GQER is approximated by the Lorentzian shape, see Eq. (2.19), with resonance parameters $E_{\mathrm{GQER}} = 11.22$ MeV, $\Gamma_{\mathrm{GQER}} = 3.99$ MeV and $\sigma_{\mathrm{GQER}} = 4.25$ mb.

Higher multipolarity, i.e. $M2$, $E3$, ..., transitions are considered weak, hence contributing marginaly to the decay of compound nucleus. So we do not include them in our simulations. Only a few weak transitions of these types have been detected yet, mostly in low excitation region.

2.3 Total radiation width of capturing states

In the framework of photon strength functions the total radiation width $\Gamma_{c\gamma}$ of a neutron capturing state c can be expressed as

$$\Gamma_{c\gamma} = \sum_f \Gamma_{c\gamma f} \approx \sum_{XL} \int_0^{B_n} \frac{\rho(B_n - E_\gamma, J_f)}{\rho(B_n, J_c)} f^{(XL)} E_\gamma^{2L+1} dE_\gamma. \tag{2.30}$$

As mentioned above the partial radiation widths $\Gamma_{c\gamma f}$ fluctuate strongly, see Sec. (2.2.1), but the fluctuation of the total radiation width $\Gamma_{c\gamma}$ is expected to be strongly suppressed thanks to the large number of involved transitions, i.e. partial radiation widths $\Gamma_{c\gamma f}$. This expectation is confirmed by observations. The *average total radiation width*, $\bar{\Gamma}_{c\gamma}$, is a subject of discussion.

Chapter 3

Modelling algorithm and experimental setup

3.1 Two Step Cascades experiment

In 1958 the idea of the method called *Two-Step Cascades* (TSC) was introduced [67]. Later this method was modified for Ge detectors [68]. The TSC experiment is two-detector coincidence measurement of γ transitions following thermal neutron capture. The basic layout of the experiment is shown in Fig. 3.1. Information about each individual event consists of amplitudes of both detector signals and their time difference. For futher study one choses such events for which sum of coincident detector signals equals to a fixed energy sum E_Σ. Specifically, if detected energy sum E_Σ equals to the energy difference between the neutron capturing state and a low-lying level, hereafter called TSC final level, data on TSCs depopulating the capturing state and ending in a fixed TSC final level are selected. Under these conditions the spectrum of energies deposited in one detector contains all transition energies involved in a TSC deexcitation process - this spectrum is called the TSC spectrum.

In Fig. 3.2 few possible cascades ending at two final TSC levels (one of them being the ground state) are indicated. In the TSC spectrum for the ground state only cascade labeled D is visible[1]. The primary transition labeled 0, that goes from the neutron capturing state directly to the ground state, can eventualy contribute only via highly unprobable parasitic effects. Situation with cascades labeled A, B and C is a lot easier since all three of them are examples of desired

[1]There is actually non-zero probability that cascade labeled E is detected as two step cascade adding some parasitic contribution to three energies in the TSC spectrum, see the discussion below.

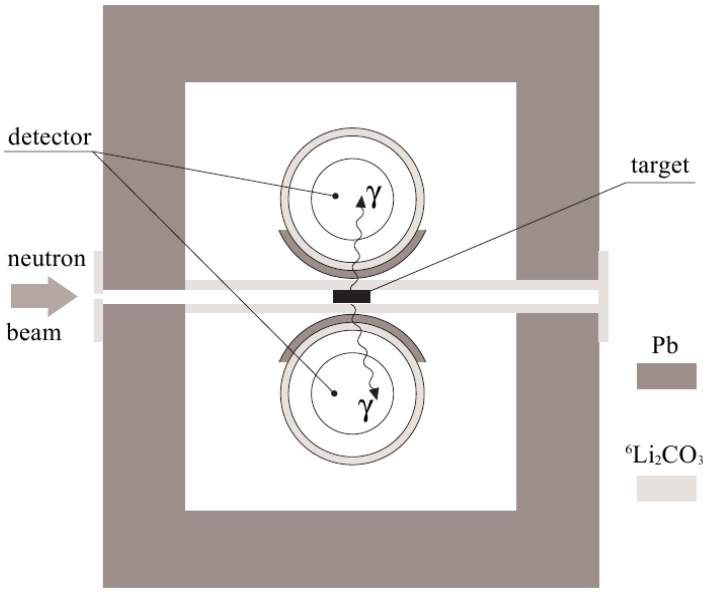

Figure 3.1: Scheme of the experimental layout. The figure is taken from [50].

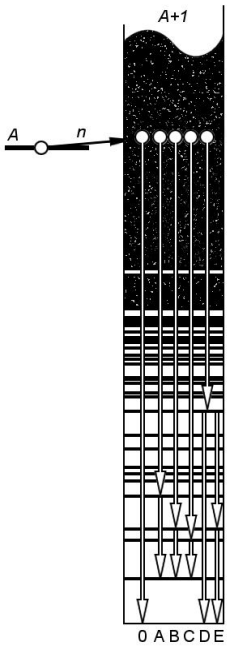

Figure 3.2: Examples of possible cascades.

contribution to TSC spectrum of first excited state. These three cascades proceed via the well-resolved intermediate level making their contribution to the TSC spectrum represented by a discrete line. For intermediate states of higher energies, the corresponding contributions form a "quasicontinuum" in the TSC spectrum. This component is of our interest since its shape and size contain information on the photon strength functions in energy interval circa 2-6 MeV. That is because the intensity of a two-step cascade $I_{\gamma\gamma}$ from an initial state i throught an intermediate level m ending on a final level f is given as

$$I_{\gamma\gamma} = \frac{\Gamma_{i\gamma m}}{\Gamma_{i\gamma}} \frac{\Gamma_{m\gamma f}}{\Gamma_{m\gamma}} = const \times E_{\gamma_1}^3 E_{\gamma_2}^3 f(E_{\gamma_1}) f(E_{\gamma_2}), \tag{3.1}$$

where $\Gamma_{\alpha\gamma\beta}$ is partial radiation widths between levels α and β, $\Gamma_{\alpha\gamma}$ is total radiation width of level α, see Eqs. (2.12) and (2.30). The transition energies are given as $E_{\gamma_1} = E_i - E_m$ and $E_{\gamma_2} = E_m - E_f$. The expectation value of PSF $f(E_\gamma)$ for an energy E_γ is supposed to follow a smooth energy dependence (i.e. above-introduced models of PSFs) while P-T fluctuations influence its actual value for a cascade, see Sec. 2.3.

The "quasicontinuum" of the TSC spectrum is believed to be described by the statistical model because of the large number of transitions involved. Thus it can provide tests of various model assumptions on PSFs and possibly level densities. The schematic representation of obtaining both TSC and energy sum spectra is visualized in Fig. 3.3. The experimental energy sum spectrum for investigated nucleus ^{177}Lu is ploted in Fig. 3.4.

A background caused by the accidental coincidences and the Compton effect is inherently contained in the coincidence spectrum. Two γ rays with desired energy sum E_Σ but originating from two different cascades can be detected in preseted coincidence time window producing a spurious event. The spurious events caused by the Compton effect originate from two γ rays with the energy sum higher than chosen energy sum E_Σ when corresponding energy difference is lost via the Compton effect. Therefore a special scanning procedure is used to extract the coincidence spectra and remove this background. Data contributing to various places in the (energy-sum) $\times$ (detection-time-difference) plane are used for the subtraction. The main "ingredients" of the procedure are [62]:

- The peak corresponding to desired events for a preselected final TSC level is defined (in Fig. 3.5 the hatched area).
- The eight rectangular regions surrounding the central region are defined.
- From coincidence spectra of these eight regions the background correction is derived as a suitable linear combination [63].

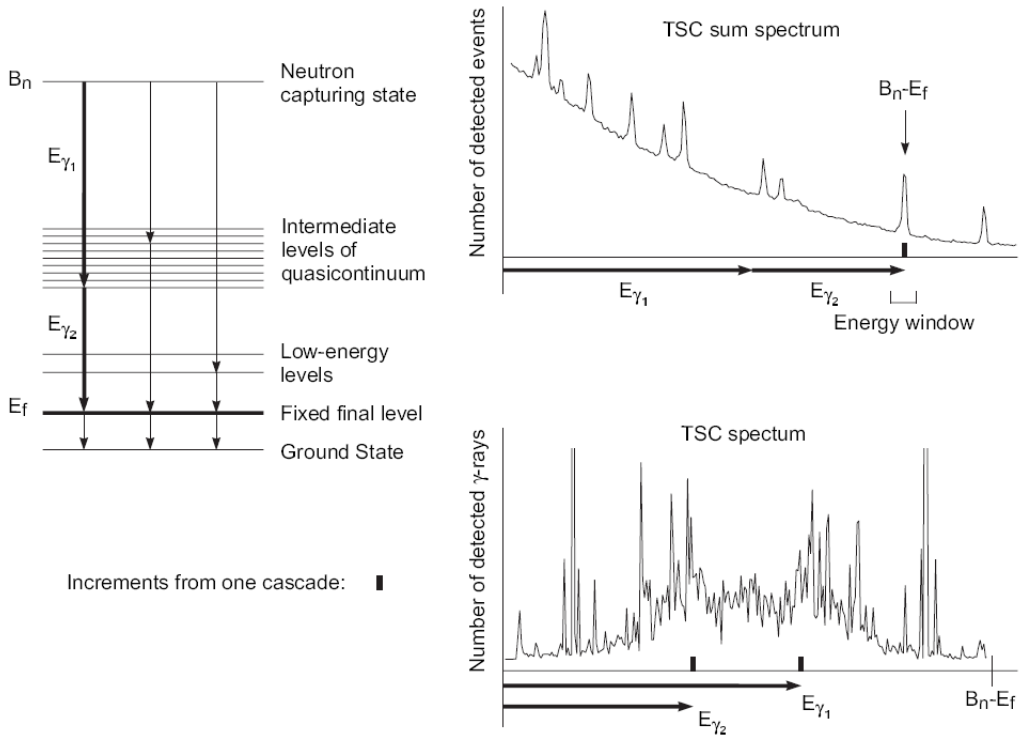

Figure 3.3: Schematic representation of obtaining TSC spectra. The figure is taken from [50].

We should note that this background correction procedure causes the so-called "bipolar structures", firstly described in [63]. These structures originate if one photon escapes the detector system after Compton scattering. The shape of bipolar structures depends on widths and locations of gate windows used for background corrections, for detailed explanation see [64]. The bipolar structure can occur only at the wings of TSC spectra and their overall area is zero. As they do not influence the "quasicontinuum" part of the TSC spectra they do not represent a problem.

Since the detectors do not distinguish between the primary and secondary transitions, the TSC spectra behave as if they were measured using a spectrometer with energy response function symmetric with respect to the midpoint of the TSC spectrum. This symmetry is revealed after correcting the TSC spectrum for energy-dependent detector efficiencies. However the resulting TSC spectrum is not strictly symmetric due to the contribution by three- and more-step cascades. The examples of experimental TSC spectra are shown in Fig. 3.6. One should once again stress that such spectrum is virtually free of background.

The probability of reaching the final TSC level in three or more steps is usually significantly higher than that in two steps. Such cascade can contribute to the TSC

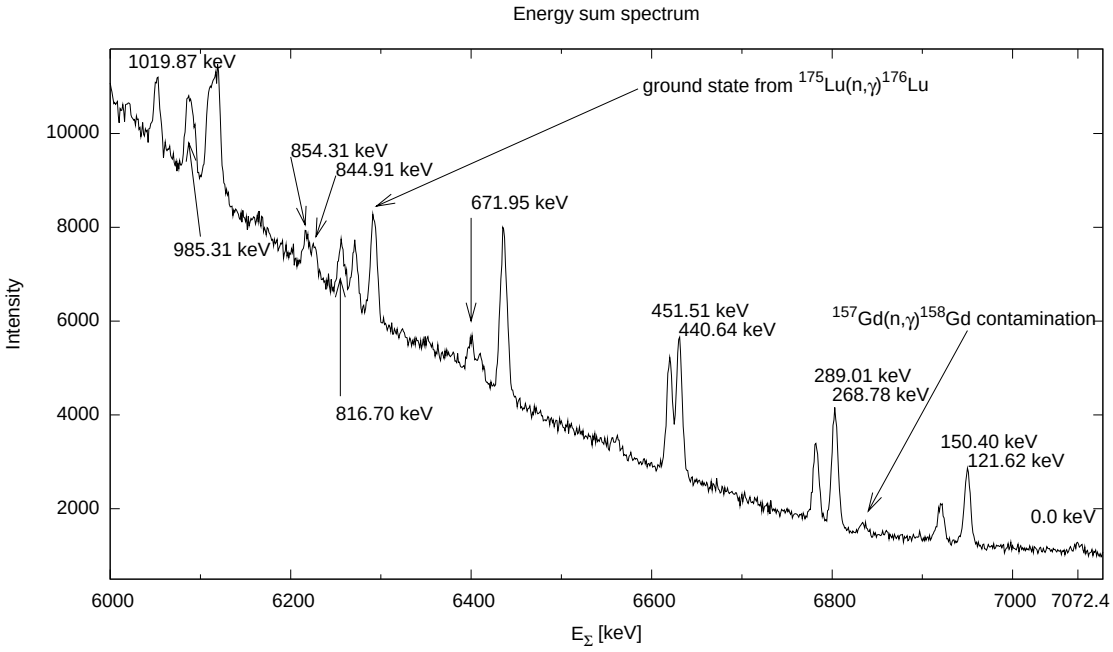

Figure 3.4: The experimental energy sum spectrum. In the sake of clarity the single and double escape peaks are not labeled.

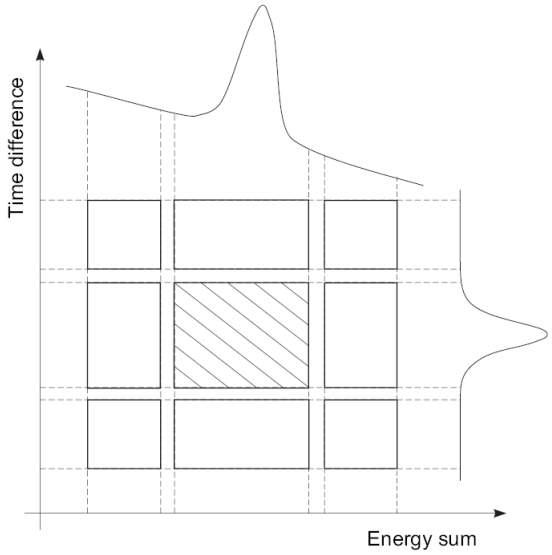

Figure 3.5: Scheme of the background subtraction procedure. The figure is taken from [51].

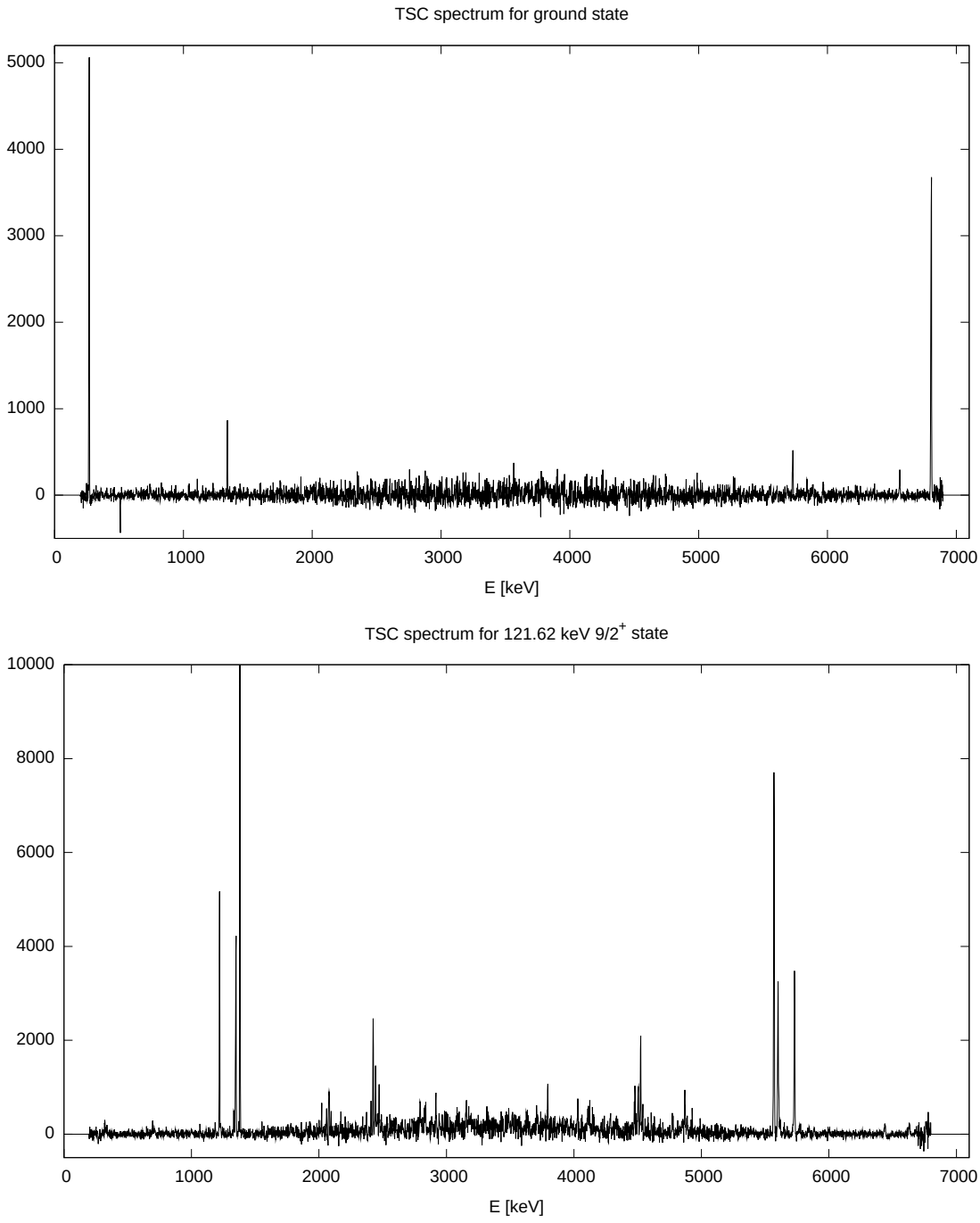

Figure 3.6: Examples of TSC spectra.

spectra if some of the photons are detected simultaneously by one of the detectors.

Despite the fact that the probability that n photons are detected simultaneously decreases with increasing n, one can not fully neglect the contribution of the three- and more-step to the TSC spectra. To minimize this parasitic effect we include three- and more- step cascades to our simulations.

It is evident that the final TSC level (unless it is the ground state) decays by emitting low energy photon. This photon can be absorbed in one of the detectors together with one of the photons from a two-step cascade eliminating the event from the TSC spectrum by enlarging the detected energy sum. This effect called "vetoing" reduces the TSC intensities (except those going to the ground state). As sketched in the schema of the experimental setup, see Fig. 3.1, the effect of vetoing is reduced by inserting lead layers between the target and the detectors. Futhermore one can estimate the corrections for vetoing if the energy dependence of the *absolute* detection efficiency is known for both detectors.

The thin lead layers between the target and the detectors help to eliminate the contribution of other possible processes - backscatter, annihilation and bremsstrahlung. The important fact is that the detector efficiencies for γ-ray energies $E_\gamma \geq 500$ keV, that is in our region of interest, remain almost unchanged after inserting these layers. All above-mentioned parasitic effects are described in detail in [62, 64].

The facility for TSC measurements has been built at the LWR-15 research reactor at Řež. A six meter long curved mirror neutron guide provides a narrow, 2×20 mm^2 beam of thermal neutrons with a flux of 3×10^6 neutron $\cdot$ cm^{-2} $\cdot$ s^{-1}. Pair of Ge detectors – one Ge(Li) and one HPGe with efficiencies 12% and 20% respectively – have been used to detect γ-rays emitted from the target – 2 g heavy capsule of natural lutetium. As seen in energy sum spectrum Fig. 3.4 both naturally occurring isotopes of lutetium contribute, we extract data for target nucleus ^{176}Lu[2] with spin and parity $J^\pi = 7^-$. To reduce γ-ray background from neutron scattering and the neutron capture in structural material a massive neutron (5 mm thick layer of $^6Li_2CO_3$) and γ shielding (lead layers) were installed as sketched in Fig. 3.1. The energy resolution in the energy sum spectrum is about 8 keV. A acquisition time needed for the experiment is hundreds hours. The detailed description of the experimental setup is given in [62].

The correction for the angular γ-γ correlation between primary and secondary γ-ray is also correctly included in our simulations. The angular correlation function

[2]The experimental data are available for both ^{175}Lu(n,γ)^{176}Lu and ^{176}Lu(n,γ)^{177}Lu reactions. The relation between the neutron binding energies can be seen in the energy sum spectrum Fig. 3.4 – the extraction of experimental data for both reactions confirmed our expectations that we should focus on the ^{176}Lu(n,γ)^{177}Lu reaction.

can be expressed as [65]

$$W(\theta) = 1 + \sum_{L=2,4,\ldots} B_L(\gamma_1) A_L(\gamma_2) Q_L P_L(cos\theta), \tag{3.2}$$

where B_L and A_L describe properties of the first and second γ transition, respectively, P_L are the Legendre polynomials of the L^{th} order and Q_L are the attenuation coefficients that describe the smearing of the angular correlation function due to finite detector solid angles. These coefficients can be calculated for a given detector and experimental setup [66]. In the very close geometry of our experimental setup the correction due to angular correlation does not exceed 10% for a dipole-dipole cascade. On the other hand mixed (i.e. $M1 + E2$) and quadrupole-quadrupole cascades may require a rather large correction.

3.2 Computer simulations

As shown in Chapter 2 there exist several combinations of models of photon strenghts functions and level densities. Futhermore one can postulate and test various irregularities in both PSFs and LDs and adjust the suggested parameters. The aim of our work is to determine which models are able to describe experimental data. In order to test all these possible combinations we simulate the electromagnetic decay of compound nucleus following the thermal neutron capture. To make the outcome of such simulation comparable with related experimental data our modelling contains also simulation of the detector system response.

3.2.1 Assumptions

As mentioned above the validity of the Extreme Statistical Model of nucleus is assumed. Other simplifying assumptions are adopted as well. The algorithm of the modelling follows namely these assumptions:

- A *complete level scheme* is adopted from other experiments below certain excitation energy E_{crit}. The complete level scheme means knowledge of all level energies, spins, parities and intensity branching ratios.
- The discretization of some *a priori* known level-density formula provides the levels of the product nucleus above E_{crit}.
- For a transition from state α to state β in energy interval $B_n > E_\alpha > E_{\mathrm{crit}}$ that is possibly, by selection rules, mixing of more multipolarities the partial radiation width $\Gamma_{\alpha\gamma\beta}$ is assumed in form

$$\Gamma_{\alpha\gamma\beta} = \sum_{XL} y^2_{\alpha\beta XL}(E_\alpha - E_\beta)^{2L+1} \frac{f^{(XL)}(E_\alpha - E_\beta)}{\rho(\alpha)}, \tag{3.3}$$

where the summation runs over all those allowed values XL whose contribution to the process of deexcitation is included in simulation, i.e. not negligable. The quantities $y_{\alpha\beta XL}$ are independently drawn random values of the normal distribution with zero mean and unit variance, $y_{\alpha\beta XL} \in \mathcal{N}(0,1)$, making the partial radiation widths random quantities from χ^2 distribution with one degree of freedom (Porter-Thomas distribution) too. The distribution of $\Gamma_{\alpha\gamma\beta}$ given by Eq. (3.3) for any set of α and/or β will be called an *ideal fragmentation*.

- Statistical independence of partial radiation widths for different initial and/or final states is assumed.

With these assumptions in mind, the levels in a real nucleus with all partial radiation widths for transitions between these levels can be obtained as a random discretization of the level density formula and a random set of values of partial radiation widths drawn from Porter-Thomas distribution. Such set contains $10^{10} - 10^{13}$ partial radiation widths for a typical deformed nucleus. This "synthetic" complete level scheme is called *nuclear realization*. Strictly speaking one can generate an infinite number of nuclear realizations, only one of them being identical with the actual complete level scheme. Some implications of this fact are discussed later. Nowadays it's impossible to store the set of partial radiation widths of mentioned size in a computer memory which might seem destructive to the described simulation. This problem is solved by so-called "precursors", their specific description is given below.

3.2.2 The algorithm of the simulation method

Following the assumptions in paragraph 3.2.1 electromagnetic cascades are generated using the following algorithm [60]:

1. Discretization of level density $\rho(E, J, \pi)$ produces all bound levels α above the critical energy E_{crit} with their essential characteristics: energy E_α, spin J_α and parity π_α.

   The *average* number of levels in given energy interval is calculated by integrating relevant level density formula, i.e. Eqs. (2.2) or (2.6). In our statistical approach this integrated number of levels can fluctuate around the average value according to Poisson distribution.

2. Above mentioned *precursor*, generator seed ζ_α is assigned to each level α with energy $E_\alpha > E_{\text{crit}}$, see Fig. 3.7. The *random* assigning of the precursors to the levels is crucial for correct function of the algorithm. All partial radiation widths $\Gamma_{\alpha\gamma\alpha'}$ for fixed level α are generated after preseting the random number generator with the precursor ζ_α, i.e. there is no need to store set of partial radiation widths in computer memory since the *same* set of $\Gamma_{\alpha\gamma\alpha'}$ is generated using the precursor ζ_α at any time. This means that by assigning the precursors ζ_α to all levels α with energy $E_\alpha > E_{\text{crit}}$ the complete set of partial radiation widths $\Gamma_{\alpha\gamma\alpha'}$ for all possible transitions $\alpha \to \alpha'$ is latently known. The set of generated partial radiation widths is thus uniquely predicted by precursors ζ_α making them a key element of the algorithm.

3. The precursor ζ_{α_c} assigned to the neutron capturing level α_c triggers the generation of partial radiation widths $\Gamma_{\alpha_c\gamma\alpha'}$ for a full set of transitions $\alpha_c \to \alpha'$ from the neutron capturing level α_c to all possible levels α' (naturally $E_{\alpha'} < B_n$).

4. A total radiation width $\Gamma_{\alpha_c\gamma} = \sum_{\alpha'} \Gamma_{\alpha_c\gamma\alpha'}$ for the neutron capturing level α_c is calculated. Now it is straight-forward to get a set of intensities $I_{\alpha\alpha'}$ for all the transitions initiating at the same capturing level α_c from a simple formula $I_{\alpha_c\alpha'} = \frac{\Gamma_{\alpha_c\gamma\alpha'}}{\Gamma_{\alpha_c\gamma}}$. These intensities naturally satisfy a normalization condition $\sum_{\alpha'} I_{\alpha_c\alpha'} = 1$, which in fact make them "branching" intensities.

5. A random number generator produces a number s_1 that governs to which bound level α_1 the selected capturing level α_c decays throught condition:

$$\sum_{\alpha'=1}^{\alpha_1-1} I_{\alpha_c\alpha'} \leq s_1 < \sum_{\alpha'=1}^{\alpha_1} I_{\alpha_c\alpha'}.$$

   As a result, the randomly chosen bound level α_1, reached by the first step of γ-cascade, is obtained.

6. The energy E_{α_1} is compared with E_{crit}. As mentioned earlier the branching intensities $I_{\alpha_1\alpha'}$ are deduced from experimental data if $E_{\alpha_1} \leq E_{\text{crit}}$, otherwise similar procedure described for capturing level α_c is applied to level α_1. Namely the precursor ζ_{α_1} presets the random generation of realizations of partial radiation widths $\Gamma_{\alpha_1\gamma\alpha'}$ for all possible transitions $\alpha_1 \to \alpha'$. After calculation of a total radiation width $\Gamma_{\alpha_1\gamma}$ and consequently all branching intensities $I_{\alpha_1\alpha'}$ for the intermediate level α_1 a random number s_2 is generated and using similar condition as in previous item a second intermediate level α_2 is reached.

7. The energy E_{α_2} is compared with E_{crit}. The simulation proceeds as described in previous item until the ground state is reached in n-th step, in the example in Fig. 3.7 the cascade reaches the ground state in four steps. When the ground state is reached all elements of cascade decay are available: all intermediate levels (i.e. their energies E_{α_i}, spins J_{α_i} and parities π_{α_i}) and all individual transitions (i.e. their multipolarities L, or multipolarity mixing ratios δ, and types X). These data are now available for modelling the desired quantity, in our case e.g. TSC spectra.

8. The procedure described in items 5-7 is repeated many times to achieve satisfactory statistical accuracy of a modelled quantity of interested. The number of cascades generated within a nuclear realization in the present work is 10^5 unless said otherwise.

9. As the Porter-Thomas fluctuations influence the quantities of interest the algorithm described in items 1-8 is repeated for several nuclear realizations. The information on a modelled quantity, e.g. TSC intensity, is obtained using various independent nuclear realizations. As a final step estimates of a mean value and an rms value are calculated for a quantity of interest.

In the described simulations two kinds of uncertainties are unavoidably present. The uncertainties originating from the finite number of simulated events in each nuclear realization can be, in principle, reduced by large enough number of events simulated for each nuclear realization, i.e. above described items 5 to 7 need to be repeated sufficiently many times. Contrary to this solution, the uncertainties originating from finite number of nuclear realizations cannot be reduced by enlarging the amount of simulated nuclear realizations. On the other hand, enlarging the sample of nuclear realizations provides better estimation of these uncertainties. Unless specified otherwise 25 realizations were simulated.

The described algorithm for simulating cascades following the thermal neutron capture was implemented into code `DICEBOX` [60].

The fact that the statistical model is not able to involve all fineness of electromagnetic decay of compound nucleus should be stressed here. Nevertheless we trust its ability to describe the main features of electromagnetic decay, i.e. that it is reasonably close to reality.

3.2.3 Response of detector system

In adopted modelling approach the response of the detector system is simulated as well. The goal of whole simulation is to obtain the *measurable* spectra under fixed model assumptions. Specifically, TSC spectra that can be directly compared with the corresponding experimental spectra.

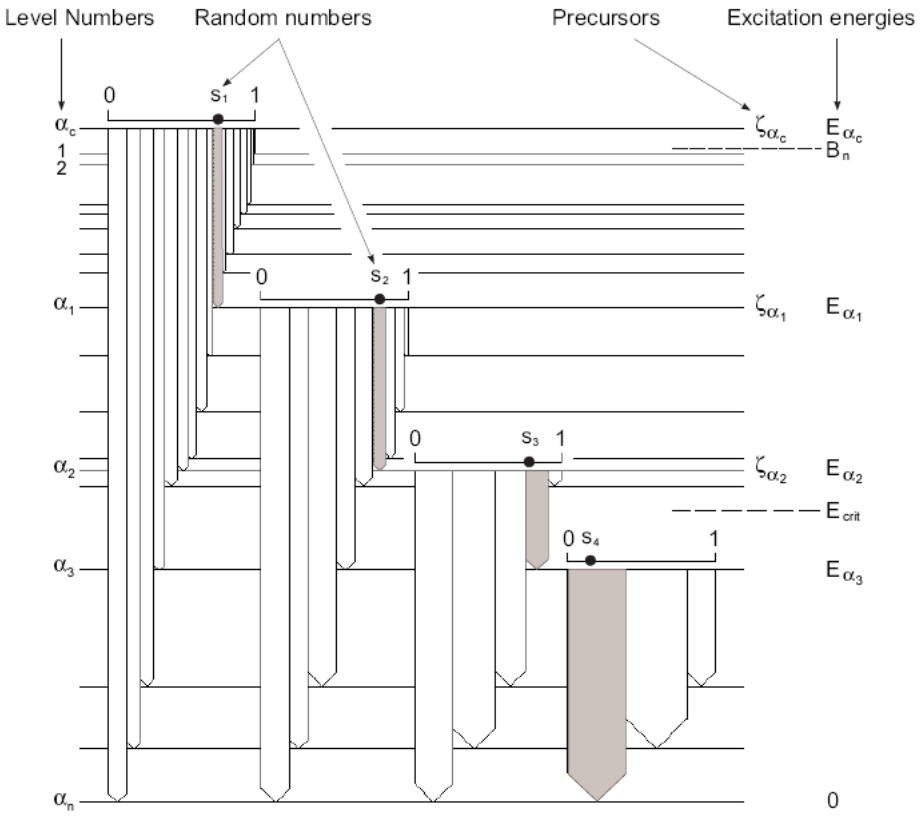

Figure 3.7: Schematic description of cascade simulation. The figure is taken from [50].

The auxiliary program simulates the detection process of artificially modelled cascades. Besides accounting the efficiency of detectors to a transition energy it also evaluates the contribution of cascades with more than two steps as well as the angular correlation and vetoing effects, see Sec. 3.1. Both the simulated and experimental TSC intensities were corrected for all the above-mentioned effects.

The TSC intensity in a given spectrum at energy E_γ is divided by the product of photopeak detector effeciencies at energies E_γ and $E_\Sigma - E_\gamma$ making the TSC intensity corrected for the detector-effeciency. As a consequence of this procedure the resulting *net* TSC spectrum is symmetric with respect to its midpoint. This procedure is not proper for summing intensities since they contain the contribution of three- and more-step cascades. One can not remove the contribution of three- and more-step cascades since it is impossible to separate this contribution from experimental spectra. This is not a problem since this contribution is taken into account in simulations. In general, one can say that these contributions

become more important as the final TSC level energy draws near the ground state.

For each final TSC level, the correction for vetoing and angular correlation was performed by multiplying both the simulated and experimental TSC intensities by proper factors. These factors were obtained by averaging both mentioned effects over an ensemble of generated cascades which in the proper interval proceed via the final TSC level.

The detector effeciencies were determined from two types of the auxiliary measurements of γ-ray spectra - with radioactive sources (^{137}Cs, ^{60}Co, ^{133}Ba, ^{152}Eu) and using reaction ^{35}Cl(n,γ). For the analysis of chlorine runs (i.e. reaction ^{35}Cl(n,γ)^{36}Cl) the transition intensities were taken from [61]. The estimated accuracy of the determined detector effeciencies is better than about 7% in the whole range of γ-ray energies. In the energy interval from 250 keV to circa 1500 keV the accuracy is better, approximately 4%.

Chapter 4

Results and discussion

This chapter contains the specific description of experimental data processing for ^{176}Lu(n,γ)^{177}Lu reaction. The model combinations used in our simulations are introduced, their outcomes are compared with corresponding experimental data. Futher aspects of our analysis are discussed.

4.1 Analysis of the experimental data

As mentioned in Chapter 3 the energy dependence of the detection efficiency is crucial for processing the simulated data to form comparable with the experimental data as well as for estimation and extraction of some parazitic effects. The absolute detection efficiency of both Ge(Li) and HPGe detectors was simulated and results of the simulation were corrected using auxiliary measurements on ^{137}Cs and ^{60}Co. These data together with ^{133}Ba, ^{152}Eu and ^{35}Cl(n,γ)^{36}Cl data were used to estimate the peak detection efficiency.

The absolute detection efficiency η_{tot} of single detector can be defined as the ratio of number of detected γ-quanta N to number of emitted γ-quanta N_0:

$$\eta_{\mathrm{tot}} = \frac{N}{N_0} = \frac{N}{A_t t} = \frac{N}{A p_t t}, \tag{4.1}$$

where A is the activity of the sample, the A_t and p_t denote the activity and probability of observed transition and t is the measurement time. The energy dependence of the absolute detection efficiency, necessary for inclusion of the veto effect, is plotted in Fig. 4.1. The final dependence (black line in Fig. 4.1) is obtained by multiplying the fit to the simulated points (red line in Fig. 4.1) so the curve fits the experimental points. Despite the fact that the simulation of the absolute detection efficiency was performed using simplified geometry the correction to the experimental data does not exceed 10%. We justify this procedure by the argument

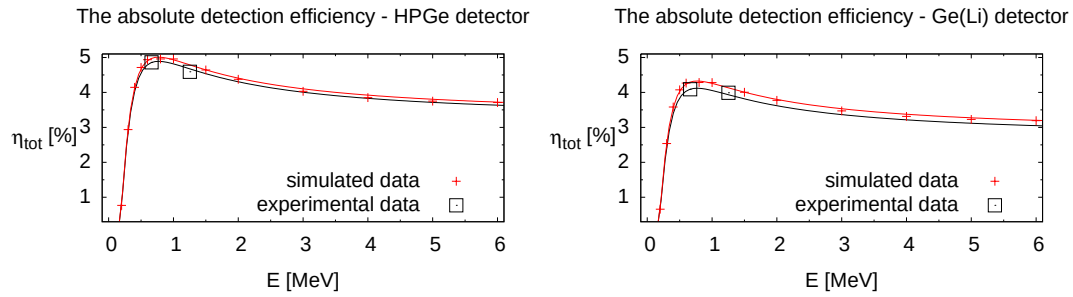

Figure 4.1: The energy dependence of the absolute detection efficiency for both used detectors.

that the shape of the energy dependence of the absolute detection efficiency does not significantly change with small change of the geometry of the detection system. Futhermore the correction on the veto effect is smaller than 10% so the eventual inaccuracy in the estimation of the energy dependence of the absolute detection efficiency does not represent significant error.

The peak efficiency $\eta(E)$ for the transition with energy E_γ is defined in a way analogous to the definition of the absolute efficiency. The number of detected γ-quanta N in Eq. (4.1) is replaced by the peak area S_t corresponding to the considered transition:

$$\eta(E) = \frac{S_t}{Ap_t t}. \tag{4.2}$$

The energy dependence of the peak detection efficiency is plotted in Fig. 4.2, for the data from chlorine runs futher adjustment is necesarry due to the fact that the activity A in Eq. (4.2) can not be reasonably established. As this adjustment is done simply by multiplying the chlorine data to reproduce the fit on the data from radioactive isotopes measurements in the overlap region (circa 0.7-1.7 MeV, see Fig. 4.2) it does not introduce futher inaccuracies.
The energy sum spectrum from the measurements focused on getting the data for ^{176}Lu(n,γ)^{177}Lu reaction is plotted in Fig. 3.4. We managed to identify the origin of all the peaks (the single and double escape peaks are not labeled) in the energy sum spectrum. We were able to extract the TSC spectra for all the levels in Tab. 4.1 but for the futher analysis we focus on three pairs of levels with best statistics, those are labeled 1-6, see Tab. 4.1. The levels labeled 7-12 are not used because the experimental errors make any reasonable analysis impossible. The ground state has served for normalization and some tests regarding $E2$ PSF, see below.

After applying the procedure eliminating the background caused by the Compton effect and the accidental coincidences described in Chapter 3 and correcting

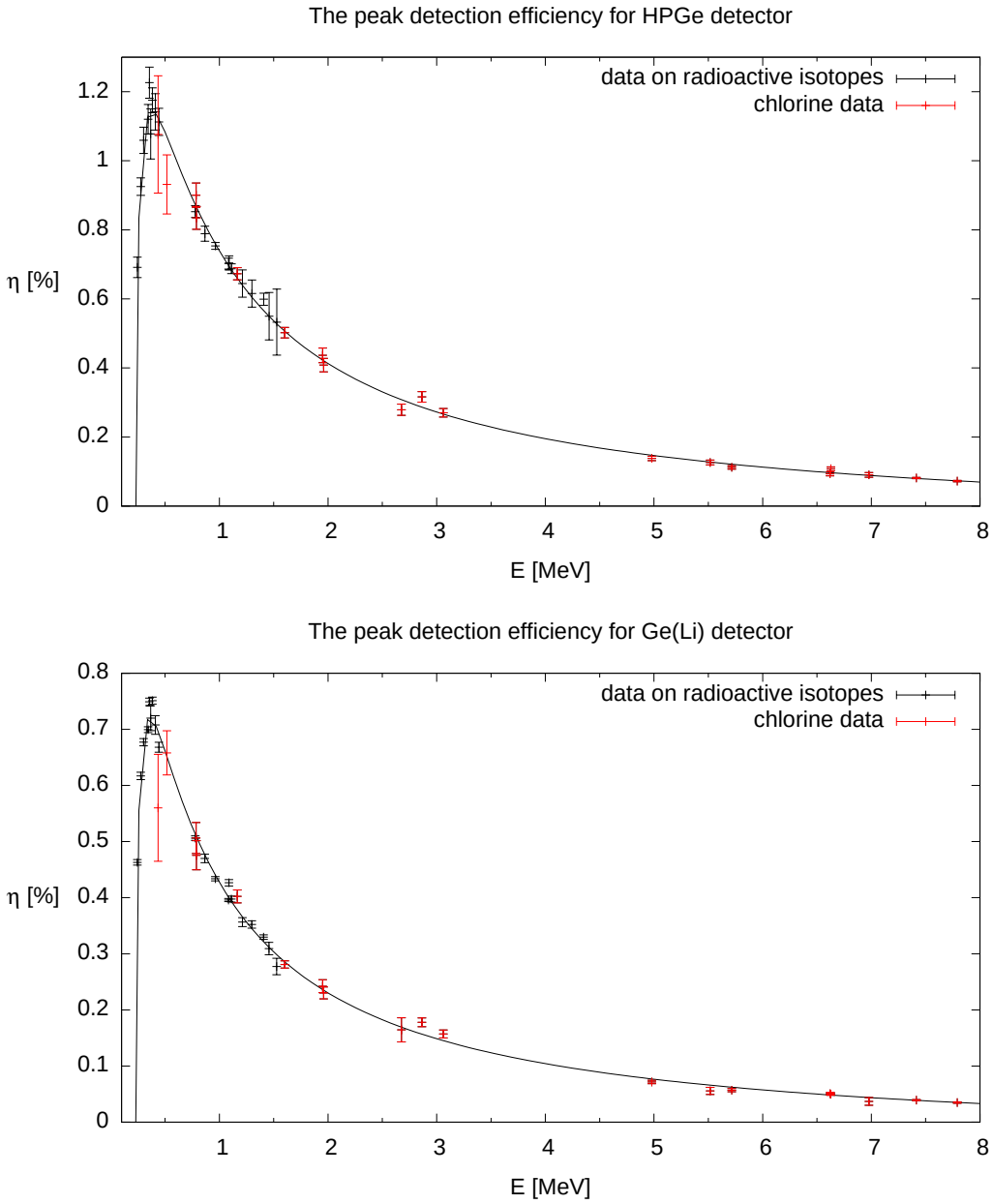

Figure 4.2: The energy dependence of the peak detection efficiency for both used detectors.

the measured TSC spectra for the detection efficiency we get essentially background-free TSC spectra. The examples of such spectra for the states labeled G.S. and 1 are given in Fig. 3.6. These spectra are then binned and ready for the comparsion

label	E_Σ [keV]	E_f [keV]	J^π
G.S.	7072.4	0.00	$\frac{7}{2}^+$
1	6950.8	121.62	$\frac{9}{2}^+$
2	6922.0	150.40	$\frac{9}{2}^-$
3	6803.6	268.78	$\frac{11}{2}^+$
4	6783.4	289.01	$\frac{11}{2}^-$
5	6631.8	440.64	$\frac{13}{2}^+$
6	6620.9	451.51	$\frac{13}{2}^-$
7	6400.5	671.95	$\frac{9}{2}^+$
8	6255.7	816.70	$\frac{11}{2}^+$
9	6227.5	844.91	$\frac{17}{2}^-$
10	6218.1	854.31	$\frac{17}{2}^+$
11	6087.1	985.31	$\frac{13}{2}^+$
12	6052.5	1019.87	$\frac{9}{2}^+$

Table 4.1: The final TSC levels identified in the energy sum spectrum.

with the modelled partner, see below.

4.2 Simulation

The simulations were performed using code `DICEBOX` as mentioned in Chapter 3. In the sake of clarity we use abbreviated notation when specifying the used models, e.g. 1000, 41116. The first number corresponds to the $E1$ PSF model, the second denotes whether the SP model or "resonances" (SF and SC models) are used for the $M1$ PSF – the third number in the case of a five-digit label indicates the presence of the SC mode. The following number indicates the $E2$ PSF model. The last position is used to specify the LD formula. All labels for the PSF and LD models are defined in Tab. 4.2, for few examples see Tab. 4.3.

In addition to already introduced $E1$ PSF models we adopt the so-called "KMF – BA" model for $E1$ PSF in our simulations, the definition is the same as in [50], that is

$$f^{(E1)}_{\text{KMF - BA}}(E_\gamma, T_f) = \begin{cases} f_{\text{KMF}} & \text{for} \quad E_\gamma < E_L \\ \frac{E_\gamma - E_L}{4} f_{\text{BA}} + \frac{E_H - E_\gamma}{4} f_{\text{KMF}} & \text{for} \quad E_L \leq E_\gamma \leq E_H \\ f_{\text{BA}} & \text{for} \quad E_\gamma > E_H \end{cases} , \quad (4.3)$$

where we set $E_L = 4$ MeV and $E_H = 8$ MeV.

The LD models are labeled according to which spin cut-off parameter is used. The labels 0 and 6 refer to CTF and BSFG formula with spin cut-off parameter from Eq. (2.5) and (2.7) respectively. The labels 8 and 9 refer to that given in Eq. (2.8).

quantity		model	label
PSF	$E1$	BA	1
		KMF	4
		GLO	5
		EGLO	6
		KMF – BA	X
	$M1$	SP	0
		SF	10
		SF+SC	11
	$E2$	SP	0
		GQER	1
LD		CTF	0
		BSFG	6
		CTF	8
		BSFG	9

Table 4.2: The labels used for PSF and LD models in the present work.

label	model for			
	$E1$	$M1$	$E2$	LD
1000	BA	SP	SP	CTF
1106	BA	SF	SP	BSFG
11100	BA	SC+SF	SP	CTF
11116	BA	SC+SF	GQER	BSFG
4100	KMF	SF	SP	CTF
41116	KMF	SC+SF	GQER	BSFG
51116	GLO	SC+SF	GQER	BSFG
61110	EGLO	SC+SF	GQER	CTF
61116	EGLO	SC+SF	GQER	BSFG

Table 4.3: The examples of abbreviated notation for the combinations of PSF and LD models.

4.3 Comparsion of experimental data with simulation results

4.3.1 Binned TSC spectra

The TSC spectra can be absolutely normalized if one knows the absolute intensity of a two-step cascade, called hereafter the *normalization cascade*, connecting the capturing state with a final TSC level. The intensity of a normalization cascade $I_{\gamma\gamma}$, see Eq. (3.1), is given by the absolute intensity of the primary transition multiplied by the intensity branching ratio of the intermediate level. Although there is no free parameter, the experimental quantities may be subject to relative large uncertainties.

The complete level scheme up to E_{crit} was adopted from Evaluated Nuclear Structure Data File (ENSDF), data therein for ^{177}Lu were obtained almost exclusively from [70]. The primary transition from the capturing state to the final TSC state labeled 3 followed by the secondary transition to the ground state was chosen as the normalization cascade. The uncertainty of the intensity of the primary transition is 8.4%, the uncertainty of the branching ratio (the other possible transition is to the final TSC state 1) is about 20%. Despite these uncertainties we concider the resulting normalization satisfactory.

The study of detailed shapes of TSC spectra can give us significant information on PSFs. Summing a TSC intensity for a given final state over relatively narrow bins, 100 keV, these possible structures of the width of several hundreds keV can be studied. On the other hand simulated TSC intensities for such a narrow interval may be strongly polluted by P-T fluctuations. As mentioned above, experimental errors may become important in the spectra with relatively small statistics. However, the experimental errors are on the level of a few percent in the TSC spectra with sufficiently large statistics, in our case for final TSC levels 1-6. The spectra, resulting from the above-mentioned summing, will hereafter be called *binned TSC spectra* and intensities in particular bins *binned TSC intensities*. As the bins are not situated symmetrically around the midpoints of the spectra the presented binned TSC spectra are not completely symmetric with respect to midpoints of the spectra.

A quantitative assessment of agreement between experimental and simulated TSC intensities based on mathematical treatment is very complicated for binned TSC spectra as individual bins in the spectra are (strongly and non-trivialy) correlated. Therefore no parameter was adopted to quantify the agreement of experimental and simulated spectra. This could make the presented conclusions rather subjective, but we hope that Figures 4.4 - 4.35 will give sufficient and clear information about the degree of agreement or disagreement between simulated and

experimental binned TSC spectra.

The figures, where simulated and experimental spectra for final TSC levels 1-6 are compared, are "organized" in the way schematically shown in Tab. 4.4. This figure layout ensures that levels with different parities are separated by columns. At the same time the energy of final TSC levels increases from the top to the bottom of the figures. The experimental data are plotted as points with errorbars, the simulation results are visualised by the coridor between two histograms. The width of the corridor corresponds to two standard deviations - the lower and upper edges correspond to the average minus and plus standard deviation, respectively. The average and standard deviation were deduced from simulations of 25 different nuclear realizations.

positive parity	negative parity
final TSC level 1	final TSC level 2
final TSC level 3	final TSC level 4
final TSC level 5	final TSC level 6

Table 4.4: The general layout of the following tables.

A special attention will be paid to the scissors mode region which is situated in the most sensitive part of the spectra. When looking at the experimental binned TSC spectra for final TSC levels 1-6 one can clearly see[1] that the TSC intensity increases around the midpoint, that is at the energy interval 3-4 MeV, forming a broad peak with a "plateau" for final levels with positive parity, see Fig. 4.3. This feature might be manifestation of presence of a resonance structure in a PSF. In the work [50] the possible influence of some structures in the level density on the peak structures in the TSC spectra is discussed and excluded. In the present work this conclusion is adopted.

The basic selection of the model combinations was performed as the first step of our analysis. As expected the combinations of models that include SP model for $M1$ PSF such as 1000, 1016 or 4016, have no chance of reproducing the experimental shapes of the TSC spectra, for the example of results see Fig. 4.4.

The situation does not improve after exchanging the single particle model of $M1$ PSF with the SF resonance *without* postulating any kind of resonance in the 3 - 4 MeV region – in our notation models 11010,41016,..., for the example

[1]The binned TSC intensities are subject to relatively large statistical (dominantly Porter-Thomas) fluctuations, these make the spectra cranky, see Fig. 4.3. On the other hand one should be able to see a general trend. The simulated spectra seem to be smooth as they result from the average over many nuclear realizations, the results for one chosen realization would show fluctuations similar to experimental spectra.

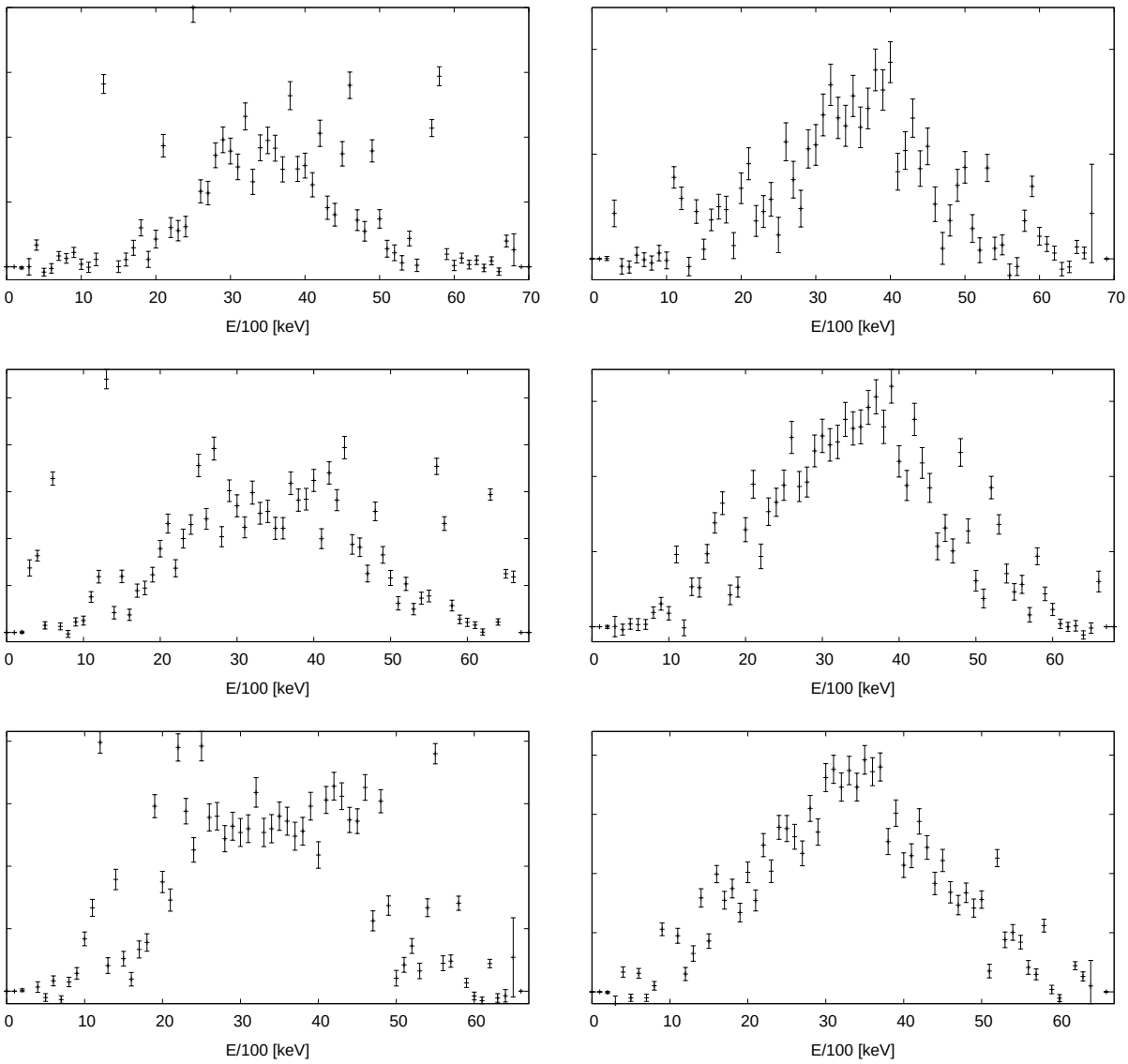

Figure 4.3: The experimental TSC spectra. One can observe the increase of the TSC intensity around the midpoint as well as the crancky structure caused by the statistical fluctuations.

of resulting TSC spectra see Fig. 4.5.

To achieve the agreement of experimental and simulated data we postulate the SC resonance in the $M1$ PSF. The initial parameters of the SC resonance were taken as (3.2;0.6;1.0) – the energy center E_{SC} follows the Eq. (2.29), the other parameters were adopted from the analysis of TSC spectra of ^{163}Dy nucleus [48, 49].

The SC resonance with these parameters is clearly unable to reproduce experimental data, see Fig. 4.7. Futhermore the simulations with models 41106 and 41116, see Fig. 4.6, 4.7, proved the fact that the results do not depend on the choice of the $E2$ model, for futher analysis we use GQER model.

To determine the parameters of the SC resonance several tens of simulations were performed on the model combination 41116. It has been found that the energy center of the SC mode must be very close to $E_{SC} = 4$ MeV to provide reasonable agreement with the experimental binned TSC spectra. This can be easily seen from Figs. 4.7 - 4.17, where the simulated TSC spectra are compared to the experimental ones for several energies of the scissors mode. Such a high energy of the mode has never been observed before. Not even significant enhancement (with respect to results in [48, 50, 51]) of the SC resonance parameters, i.e. increasing the Γ_{SC} to 1.4 MeV and simultaneously the σ_{SC} to 2 mb, does not produce the agreement with experimental data for $E_{SC} < 3.8$ MeV, for example see Fig. 4.11. We estimate that the energy cannot be lower than 3.8 MeV and higher than 4.1 MeV.

Contrary to rather precise determination of E_{SC} one is not able to specify the halfwidth and total strength of the scissors mode with high accuracy. However it is evident that Γ_{SC} must be ≥ 1.0 MeV and σ_{SC} must be ≥ 2.0 mb to achieve an acceptable agreement with experiment, see Fig. 4.13 - 4.17. In our simulations we did not tried to test $\Gamma_{SC} > 1.4$ MeV and $\sigma_{SC} > 3.0$ mb. In any case, the total strength of the scissors mode is significantly higher than the strength observed so far in any other nucleus.

Using the parameters (4.0;1.0;3.0) of the SC resonance we examined which combinations of $E1$ and LD models give the reasonable reproduction of the experimental binned TSC intensities, the results are plotted in Figs. 4.18 - 4.26. The BA model of $E1$ PSF with CTF LD model gives reasonable agreement, but the errors of simulate TSC intensities are significantly higher, see Fig. 4.18. In the combination with BSFG formula the BA model fails to predict the experimental data, see Fig. 4.19.

The BSFG rather than CTF formula seems to be more suitable in combination with KMF model, see Figs. 4.20 and 4.15.

The GLO model fails with both LD models – the results show systematic underestimation of the TSC intensities for positive parity and oposite effect for positive parity, see results – Fig. 4.21 and 4.22. This is not that surprising as this model was suggested for spherical nuclei and its generalization, the EGLO model should describe deformed nuclei better.

We believe that for the EGLO and KMF – BA models we are able to adjust the parameters of SC resonance to reproduce the experimental data, the parameters (4.0;1.0;3.0) seem reasonable for the 61110 combination. Futher simulations

using this model combination revealed that more suitable parameters of SC mode are (4.0;1.0;2.0), the resulting TSC spectra are given in Fig. 4.27. The futher adjustment was also performed on the model combination X1110, the results are similar to those on model combination 41116.

The LD formulae 8 and 9 were tested in the combinations with 4111 and 6111 PSF models. The results with the SC parameters (4.0;1.0;3.0) are given in Figs. 4.28 – 4.31. The resulting binned TSC spectra do not differ much from their partners with LD models 0 and 6. Our conclusion is that these models (in proper combination with PSFs models) are able to produce reasonable agreement of simulated and experimental data. The TSC data seems to be insensitive to the change of level density given by different spin cut-off parameters, see Eqs. (2.5),(2.7) and (2.8).

So far the strict form of the Brink hypothesis has been assumed for the $M1$ PSF. We performed some test of the violation the Brink hypothesis, in general we concidered the parameter of the SC resonance to shift lineary with the energy of the final level E_f. That is, if the parameter above the ground state is p_0, the parameter of the SC resonance above the excited state f is $p_f = p_0 + k \times E_f$, where p can be E_{SC}, Γ_{SC} or σ_{SC}. No significant improvement of agreement of experimental with simulated data was achieved.

Whenever the scissors mode was postulated in our simulations, it was present in $M1$ PSF so far. The fact, that the SC resonance is not present in $E1$ PSF as a so-called "pigmy" resonance and missing in $M1$ PSF, can be intuitively deduced from the balance of experimental binned TSC intensities around the midpoint of the spectra for the pair of final TSC levels at similar excitation energy with the same spin but opposite parity. One parity (the same as the parity of the capturing state) is populated by the combination of transitions of the same type and multipolarity – $E1 + E1$ and $M1 + M1$, the opposite parity by the combination $E1 + M1$ and $M1 + E1$. When removing the $M1$ strength and adding the $E1$ strength around the $E_\gamma \approx 4$ MeV, one clearly increases the TSC intensities for the states with same parity as the capturing state and dramaticly decreases the TSC intensities for the states with opposite parity. The intuitive conclusion is confirmed by simulation result, see Fig. 4.32, we postulated pigmy resonance (in the form of Lorentzian (2.19)) in $E1$ PSF and removed the SC mode from $M1$ PSF.

Removing the SC resonance from $M1$ PSF and postulating a resonance in the $E2$ PSF – in the way similar to $E1$ case – one does not dramatically influence the TSC intensities (with respect to those with SC mode in $M1$ PSF) for the low-lying final TSC states 1-6 since for these states the selection rules for the $M1$ and $E2$ tran-

sitions are the same. One can expect the influence of the fact that $E2$ transitions can procede via greater spin range. Nevertheless differences are notable between the TSC spectra in Fig. 4.33 and Fig. 4.15, there are probably several reasons, one of them being the absence of SF-like structure in $E2$ PSF. The question raises whether the binned TSC spectra would look the same for the $M1$ PSF with SC mode but without SF resonance. These spectra are plotted in Fig. 4.34, the spectra look significantly different compared to those in Fig. 4.33. These figures indicate that the TSC spectra are better reproduced with the resonance structure in $M1$ PSF.

In addition there seems to be another way how to check the multipolarity of the resonance structure. One can try to check predicted TSC intensities for a final TSC level that can be populated by the combinations of transitions that need to contain at least one $E2$ transition, in our case the ground state (that is dominantly populated by $E1+E2$ combination). The resulting spectra are plotted in Fig. 4.35 – one for the $M1$ PSF with SC mode, the other one for the $E2$ PSF with a SC-like resonance and $M1$ PSF without SC resonance, see labels. Considering both the negative influence on the final TSC states 1-6 (keeping the agreement of experimental and modelled data for states 1 and 2 the simulations clearly fail at reproducing the experimental TSC intensities for states 5 and 6) and absence of a peak structure around the midpoint of the binned experimental TSC spectrum for the ground state our conclusion is that the a SC-like resonance in $E2$ PSF cannot reproduce the experimental data and SC resonance in $M1$ PSF is thus necessary.

The mentioned simulations without SF resonance in $M1$ PSF also proved the fact that the resulting binned TSC spectra are sensitive to its presence in $M1$ PSF. The results with SF resonance are clearly better, compare the spectra in Fig. 4.34 and Fig. 4.15.

4.3.2 Average total radiation width

The average total radiation width of capturing state $\bar{\Gamma}_{c\gamma}$, see Sec. 2.3, provides another criterion for the analysis of model combinations. The experimental value for the nucleus ^{177}Lu is $\bar{\Gamma}_{c\gamma} = 90 \pm 20$ meV [71]. The errors of simulation results do not exceed 5% and are thus negligible with respect to the experimental uncertainty of 22%.

Tables 4.7 – 4.8 show that the $\bar{\Gamma}_{c\gamma}$ depends strongly on the adopted LD formula. The results using CTF formula are at least twice smaller than those deduced using BSFG formula with spin cut-off parameter given in Eq. (2.5). The general feature is the underestimation of the experimental value by the CTF formula.

The results given in Tabs. 4.5 and 4.7 confirm some conclusions given in Sec. 4.3.1. It has been found that the $E1$ transitions influence the average total radiation

width (TRW) much strongly than $M1$ and $E2$ transitions. As a consequence, the large experimental uncertainty of TRW does not allow us to make any restriction to models of $M1$ and $E2$ PSFs. In fact, as shown in Tab. 4.6, TRW not negligibly depend on the position and strength of the scissors mode but almost all the results are still consistent with the experimental value.

On the other hand, we are able to make some general conclusions about $E1$ PSF. TRW obtained with the combination of BA model for $E1$ PSF and BSFG model is too high while the predictions of other $E1$ PSF models in combination with CTF model are too low. It means that only certain combinations of level density and $E1$ PSF are allowed.

model combination	E_{SC} [MeV]	Γ_{SC} [MeV]	σ_{SC} [mb]	$\bar{\Gamma}_{c\gamma}$ [meV]
1016				246
11016				161
11116	3.2	0.6	1.0	181
4016				88
41016				56
41106	3.2	0.6	1.0	76
41116	3.2	0.6	1.0	76

Table 4.5: The average total radiation widths for basic model combinations.

model combination	E_{SC} [MeV]	Γ_{SC} [MeV]	σ_{SC} [mb]	$\bar{\Gamma}_{c\gamma}$ [meV]
41116	2.6	0.6	1.0	88
41116	2.9	1.0	2.0	136
41116	3.2	0.6	1.0	76
41116	3.5	0.6	1.0	71
41116	3.5	1.4	2.0	121
41116	3.8	1.0	2.0	92
41116	3.9	1.4	2.0	102
41116	4.0	0.8	2.0	80
41116	4.0	1.0	3.0	101
41116	4.0	1.4	3.0	119
41116	4.1	1.4	3.0	114

Table 4.6: The average total radiation widths for different sets of SC resonance parameters.

model combination	E_{SC} [MeV]	Γ_{SC} [MeV]	σ_{SC} [mb]	$\bar{\Gamma}_{c\gamma}$ [meV]
11110	4.0	1.0	3.0	77
11116	4.0	1.0	3.0	201
41110	4.0	1.0	3.0	39
41116	4.0	1.0	3.0	101
51110	4.0	1.0	3.0	36
51116	4.0	1.0	3.0	91
61110	4.0	1.0	3.0	43
61116	4.0	1.0	3.0	97
X1110	4.0	1.0	3.0	40
X1116	4.0	1.0	3.0	104

Table 4.7: The average total radiation width for various combinations of $E1$ PSF and LD models.

model combination	E_{SC} [MeV]	Γ_{SC} [MeV]	σ_{SC} [mb]	$\bar{\Gamma}_{c\gamma}$ [meV]
41110	4.0	1.0	3.0	39
61110	4.0	1.0	3.0	47
41118	4.0	1.0	3.0	26
61118	4.0	1.0	3.0	28
41116	4.0	1.0	3.0	101
61116	4.0	1.0	3.0	97
41119	4.0	1.0	3.0	66
61119	4.0	1.0	3.0	69

Table 4.8: The influence of the LD formula on the average total radiation width.

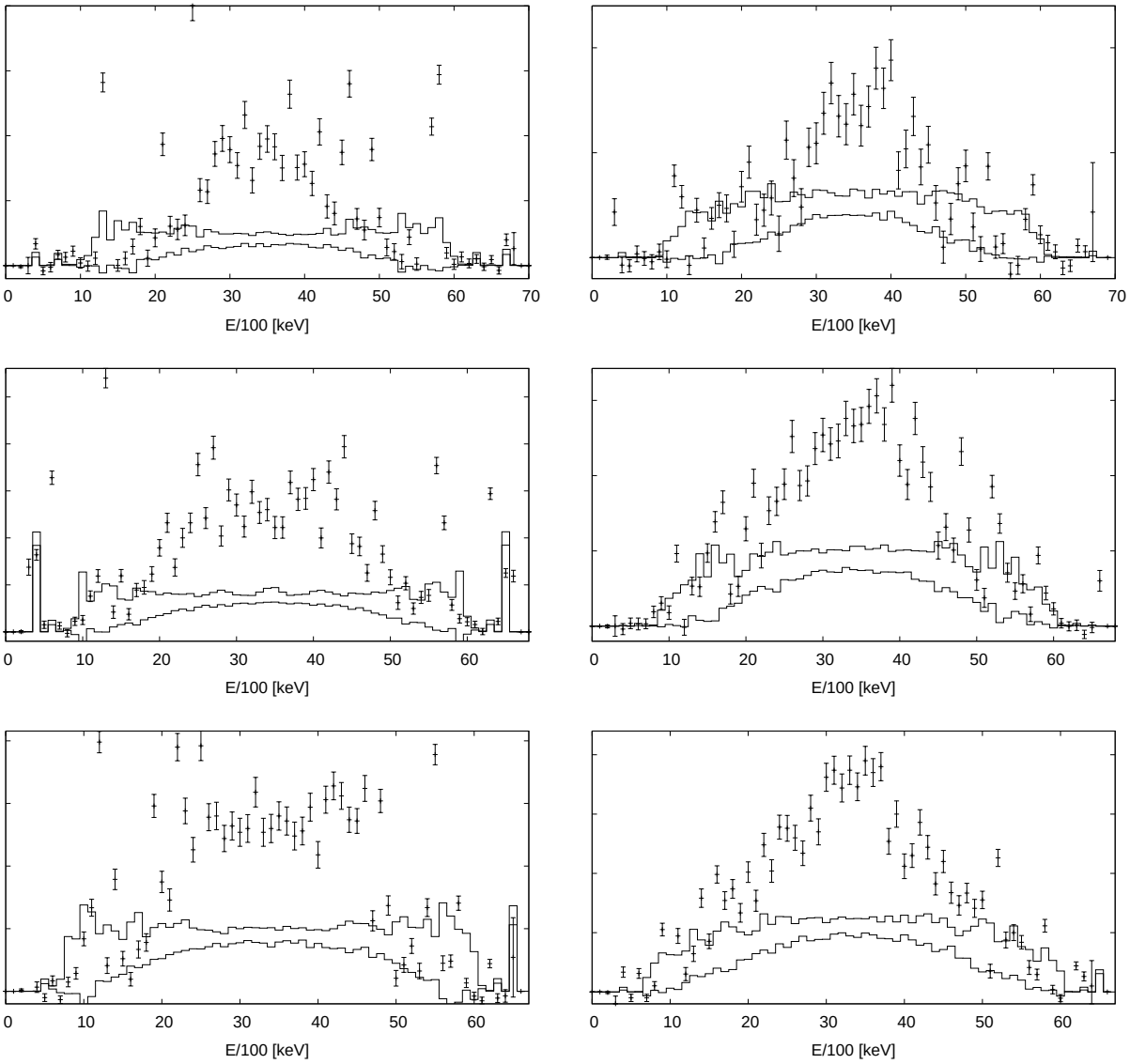

Figure 4.4: The TSC spectra for the model combination 1016.

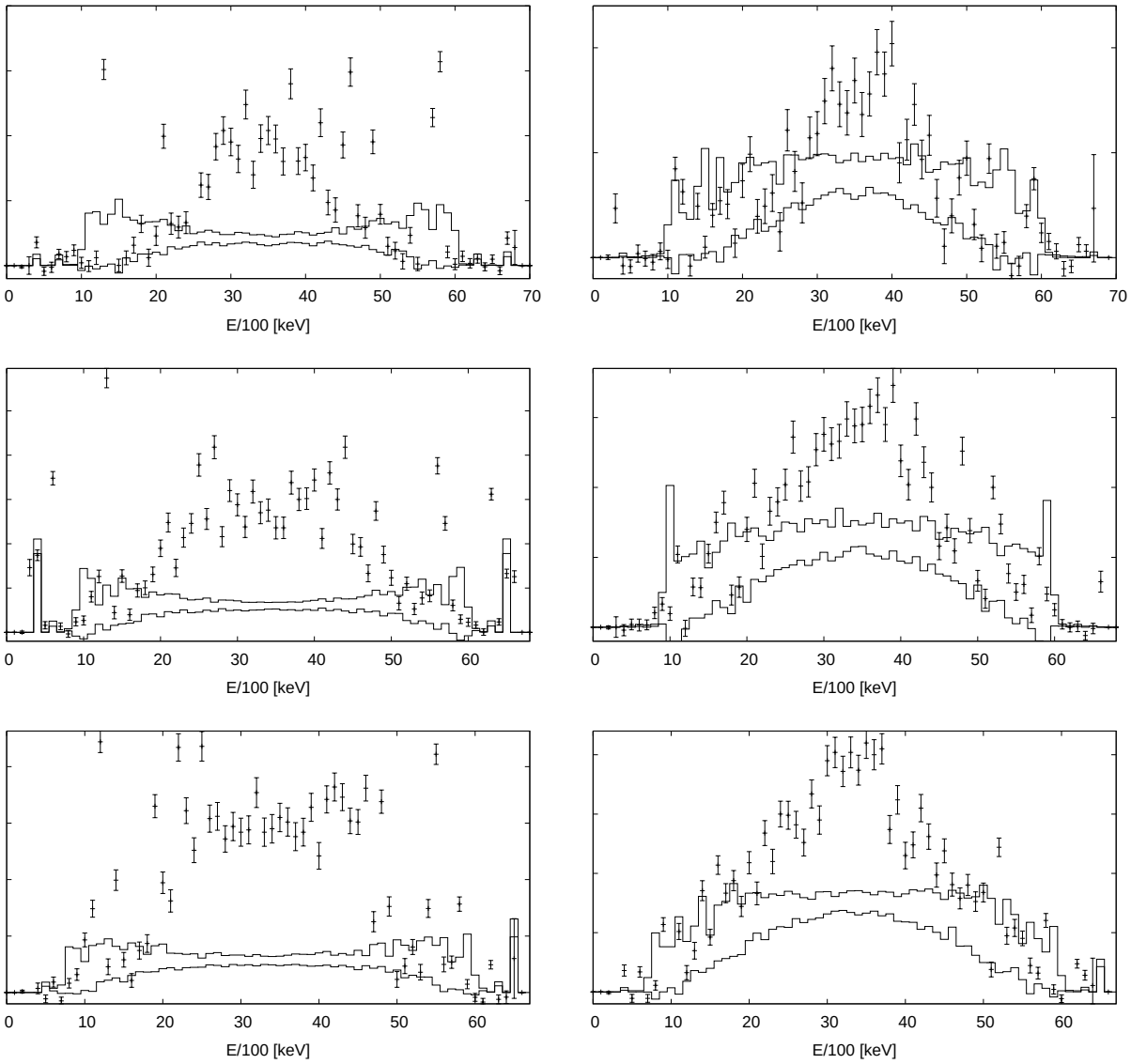

Figure 4.5: The TSC spectra for the model combination 41016.

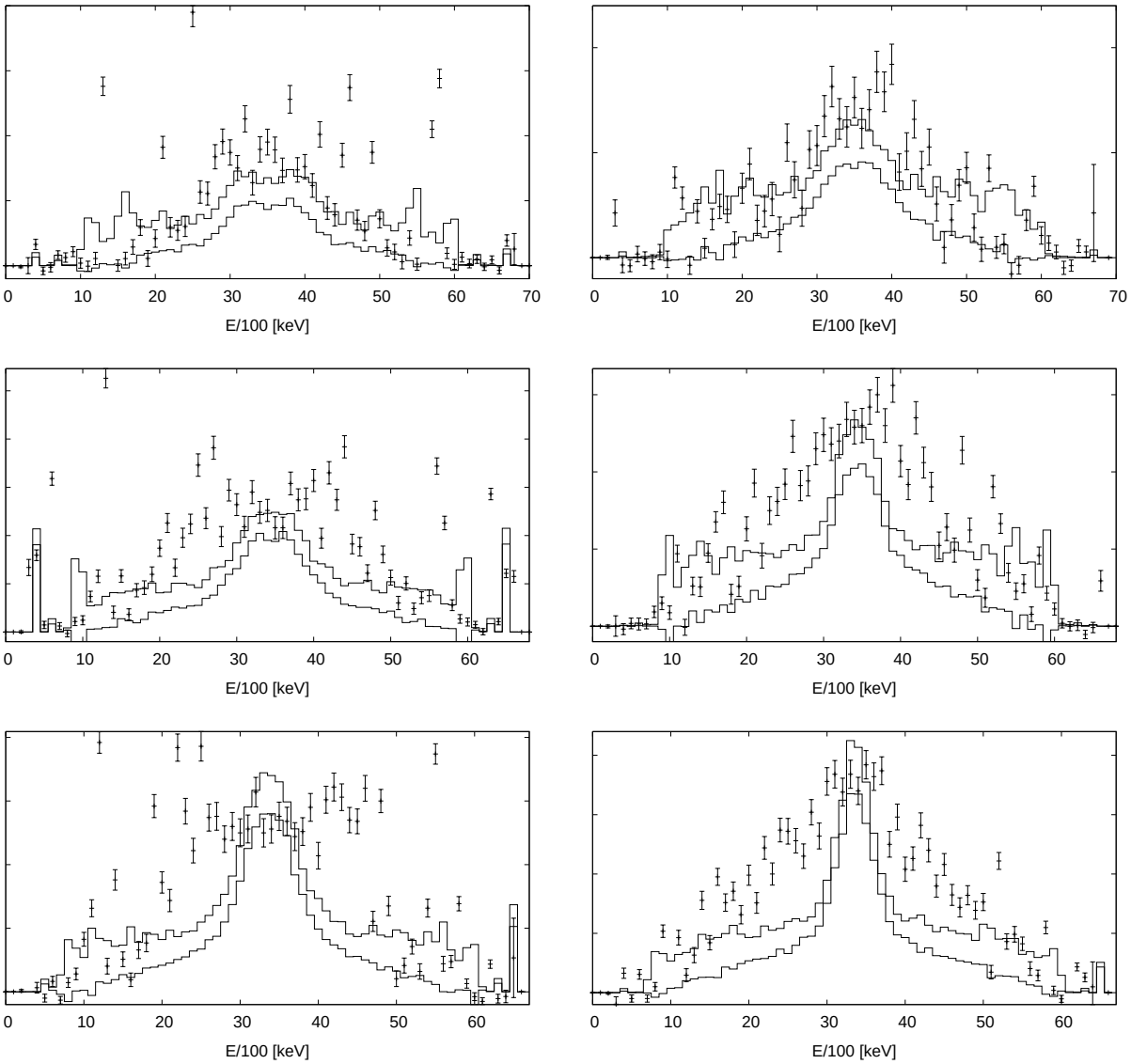

Figure 4.6: The TSC spectra for the model combination 41106 with SC resonance parameters (3.2;0.6;1.0).

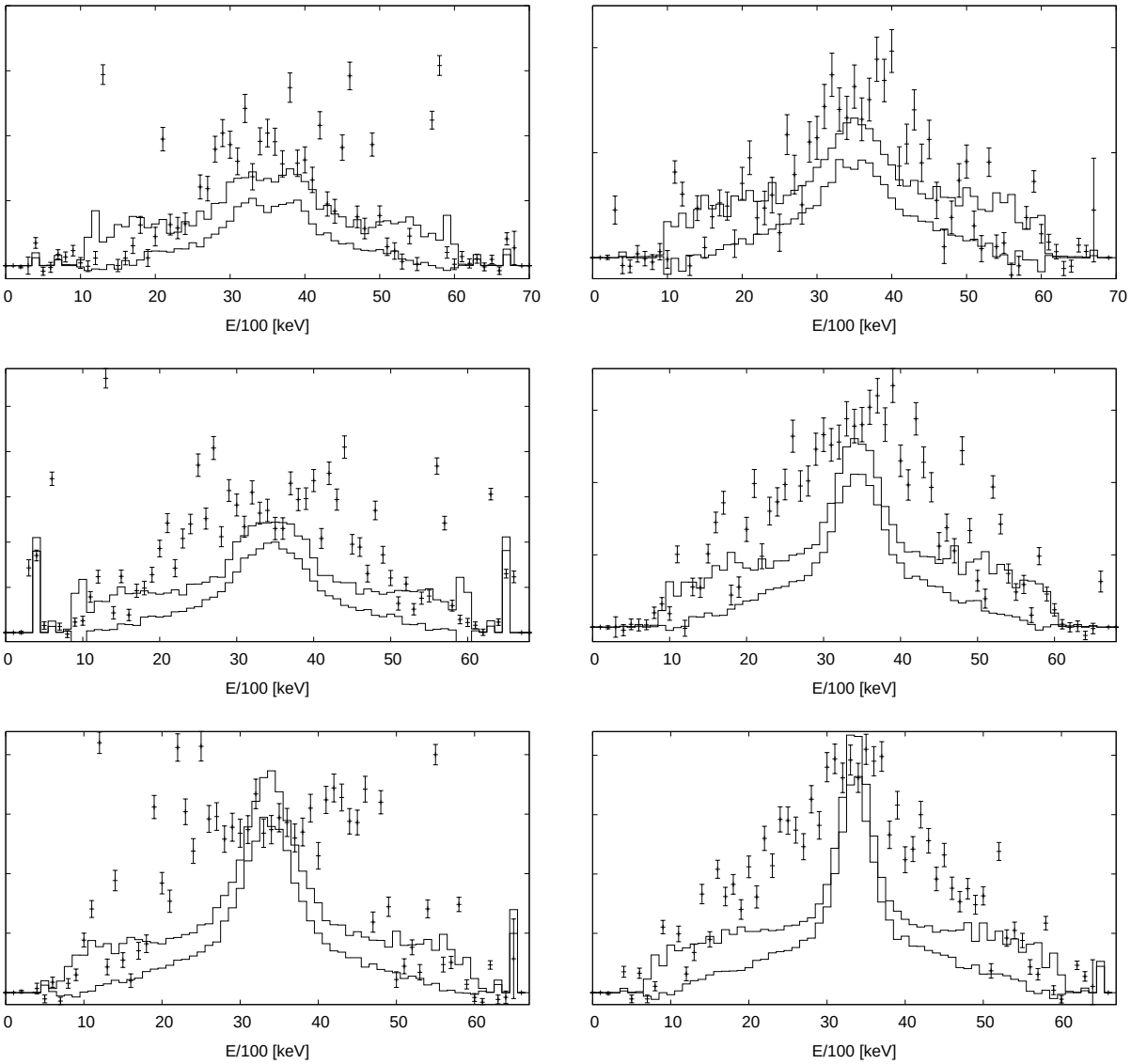

Figure 4.7: The TSC spectra for the model combination 41116 with SC resonance parameters (3.2;0.6;1.0).

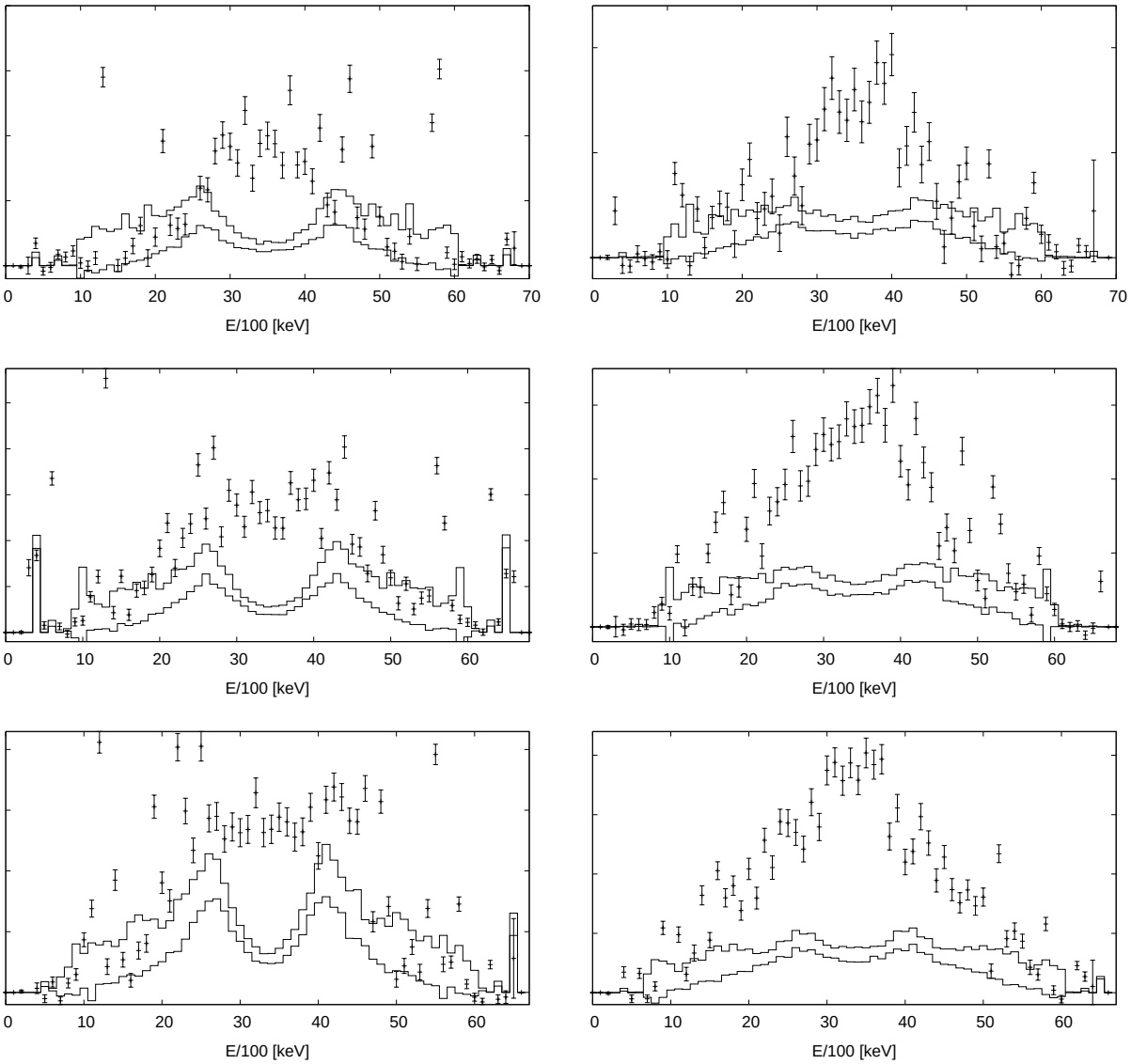

Figure 4.8: The TSC spectra for the model combination 41116 with SC resonance parameters (2.6;0.6;1.0).

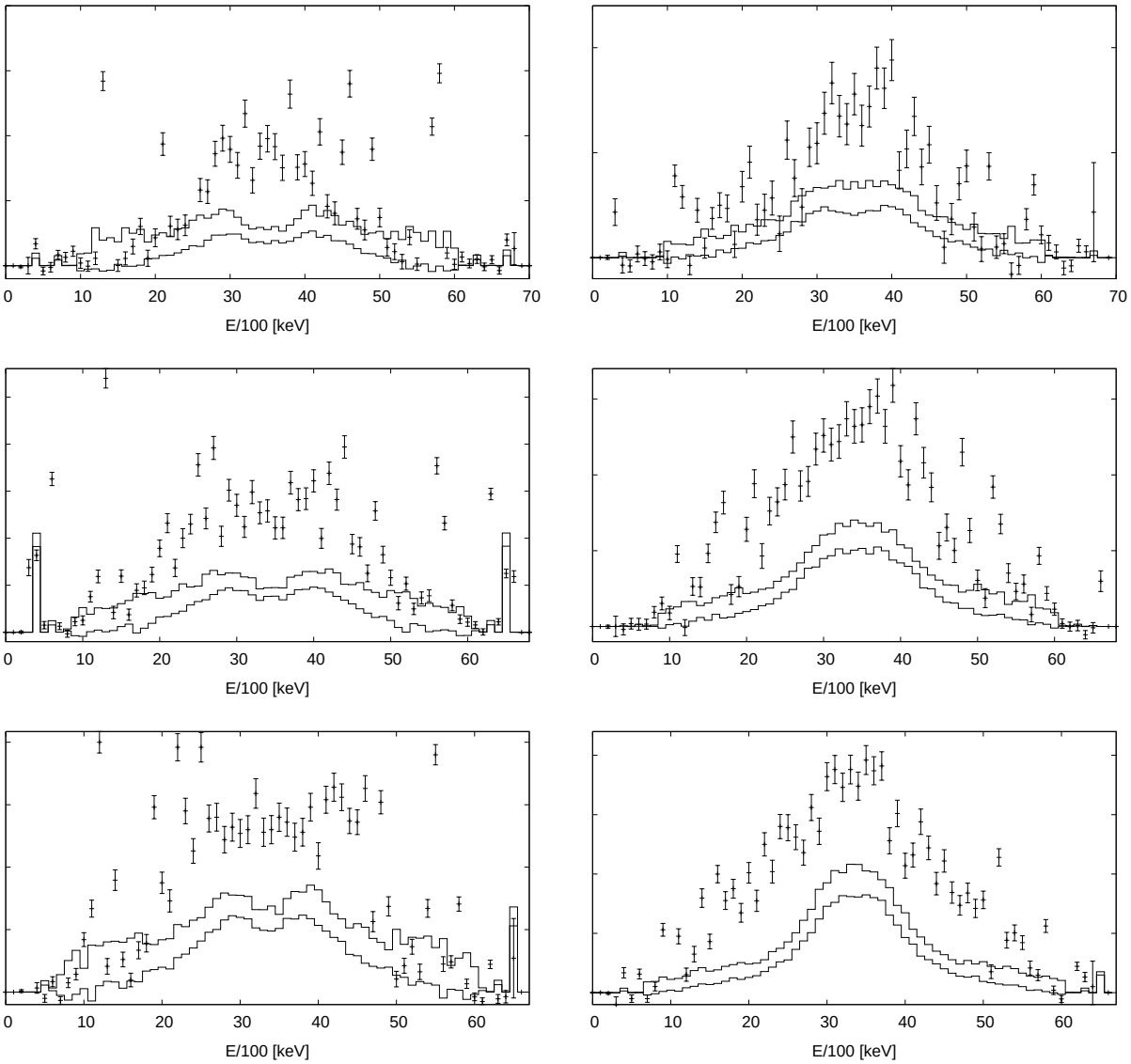

Figure 4.9: The TSC spectra for the model combination 41116 with SC resonance parameters (2.9;1.0;2.0).

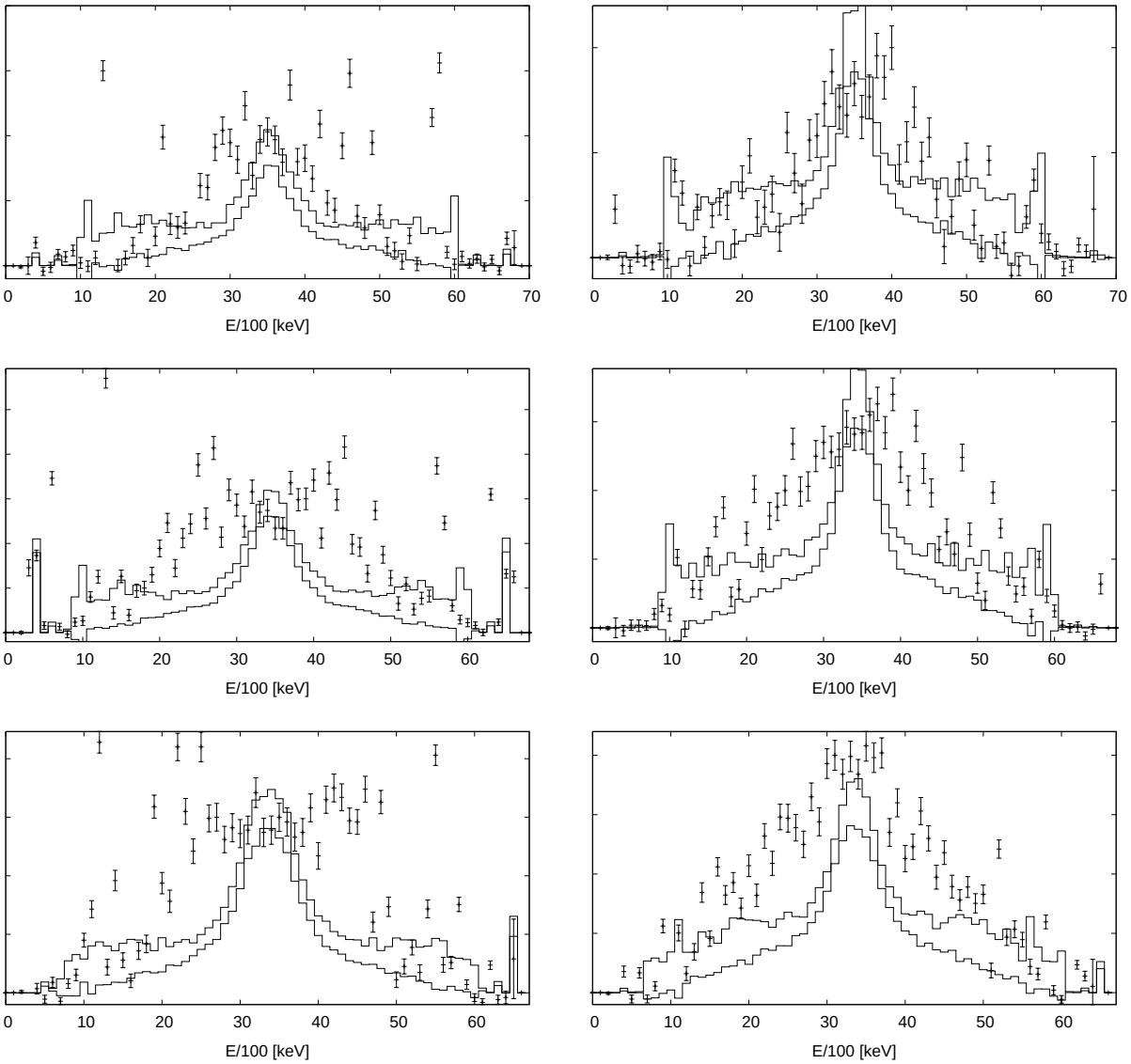

Figure 4.10: The TSC spectra for the model combination 41116 with SC resonance parameters (3.5;0.6;1.0).

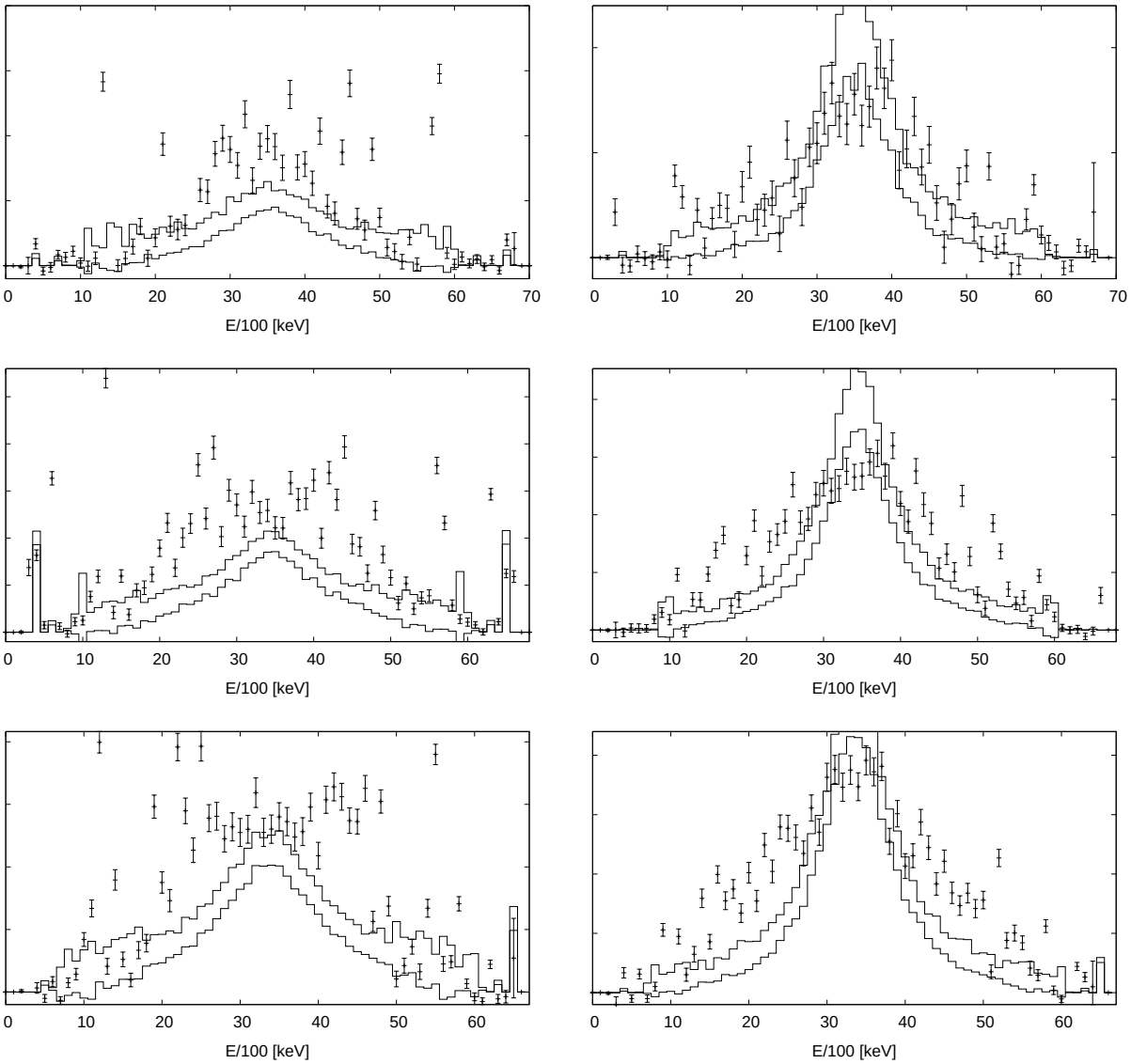

Figure 4.11: The TSC spectra for the model combination 41116 with SC resonance parameters (3.5;1.4;2.0).

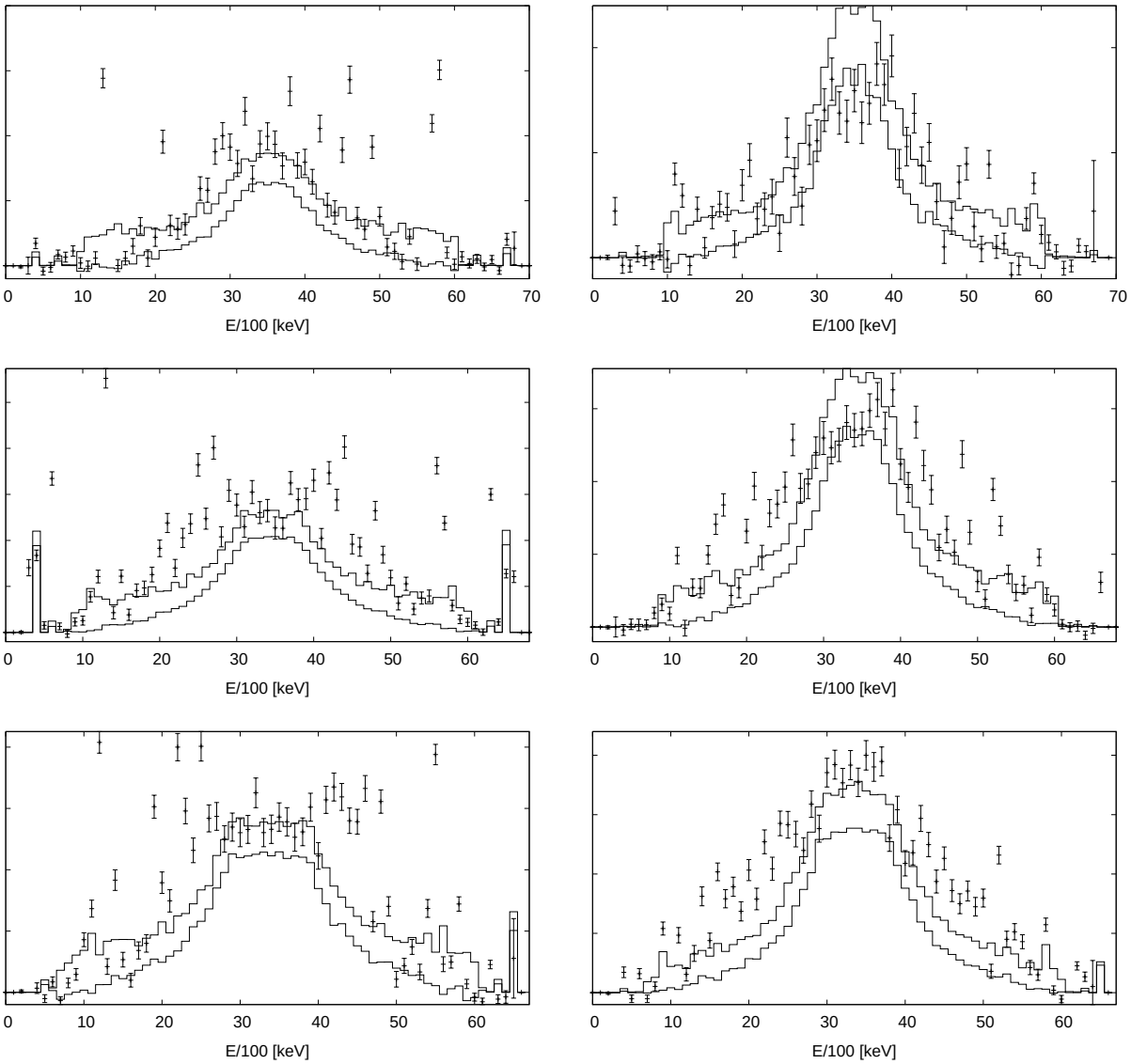

Figure 4.12: The TSC spectra for the model combination 41116 with SC resonance parameters (3.8;1.0;2.0).

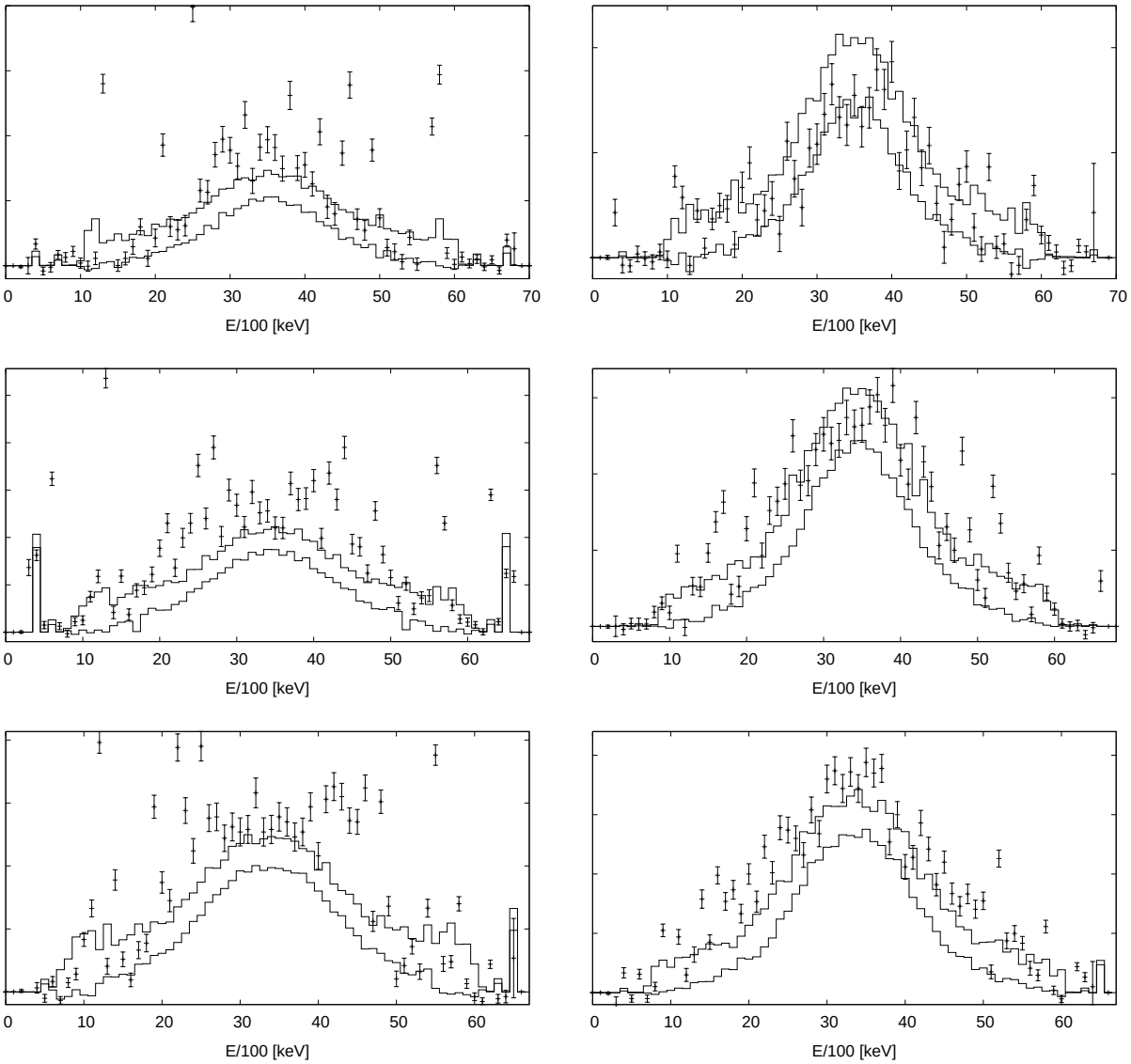

Figure 4.13: The TSC spectra for the model combination 41116 with SC resonance parameters (3.9;1.4;2.0).

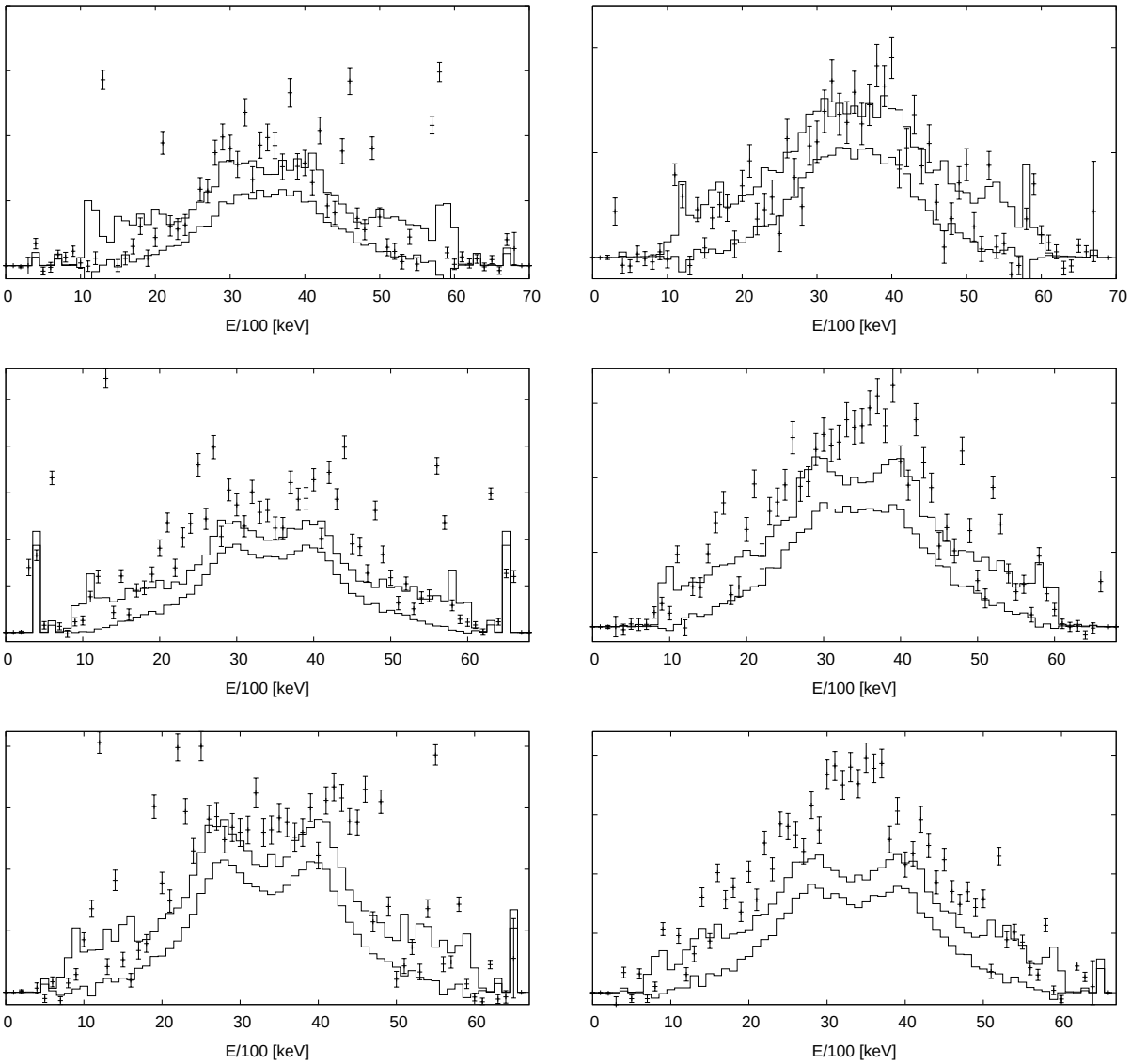

Figure 4.14: The TSC spectra for the model combination 41116 with SC resonance parameters (4.0;0.8;2.0).

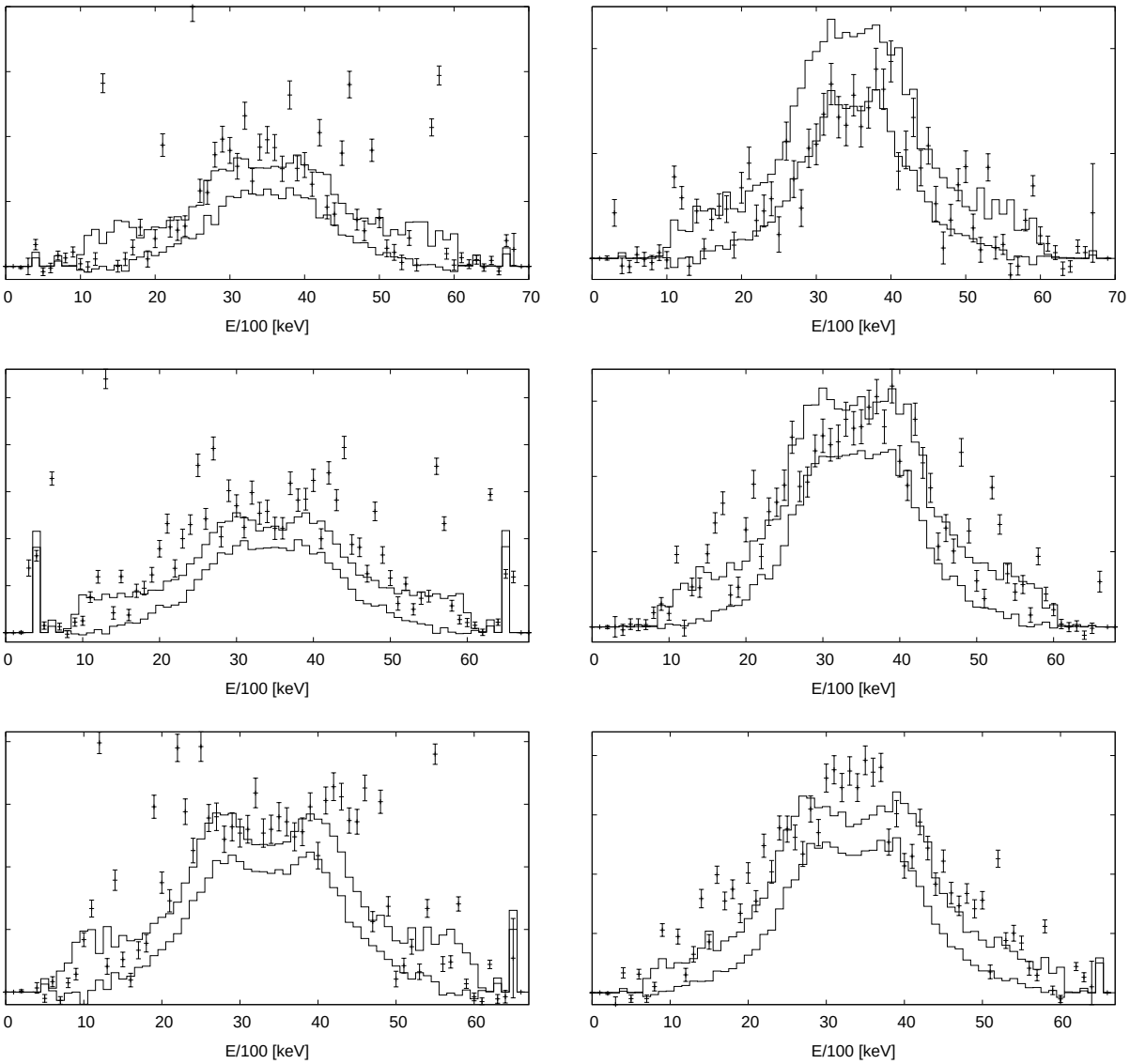

Figure 4.15: The TSC spectra for the model combination 41116 with SC resonance parameters (4.0;1.0;3.0).

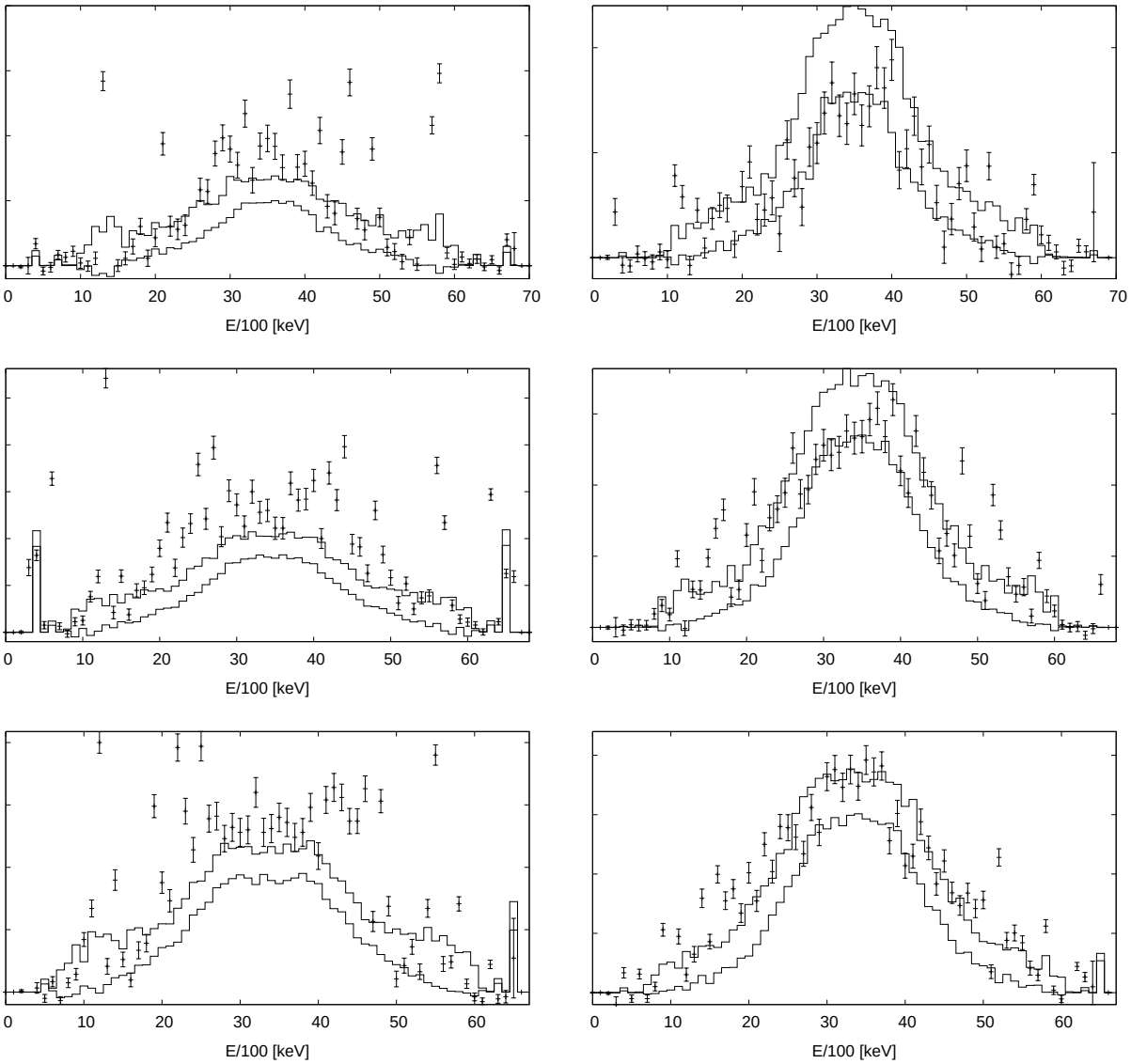

Figure 4.16: The TSC spectra for the model combination 41116 with SC resonance parameters (4.0;1.4;3.0).

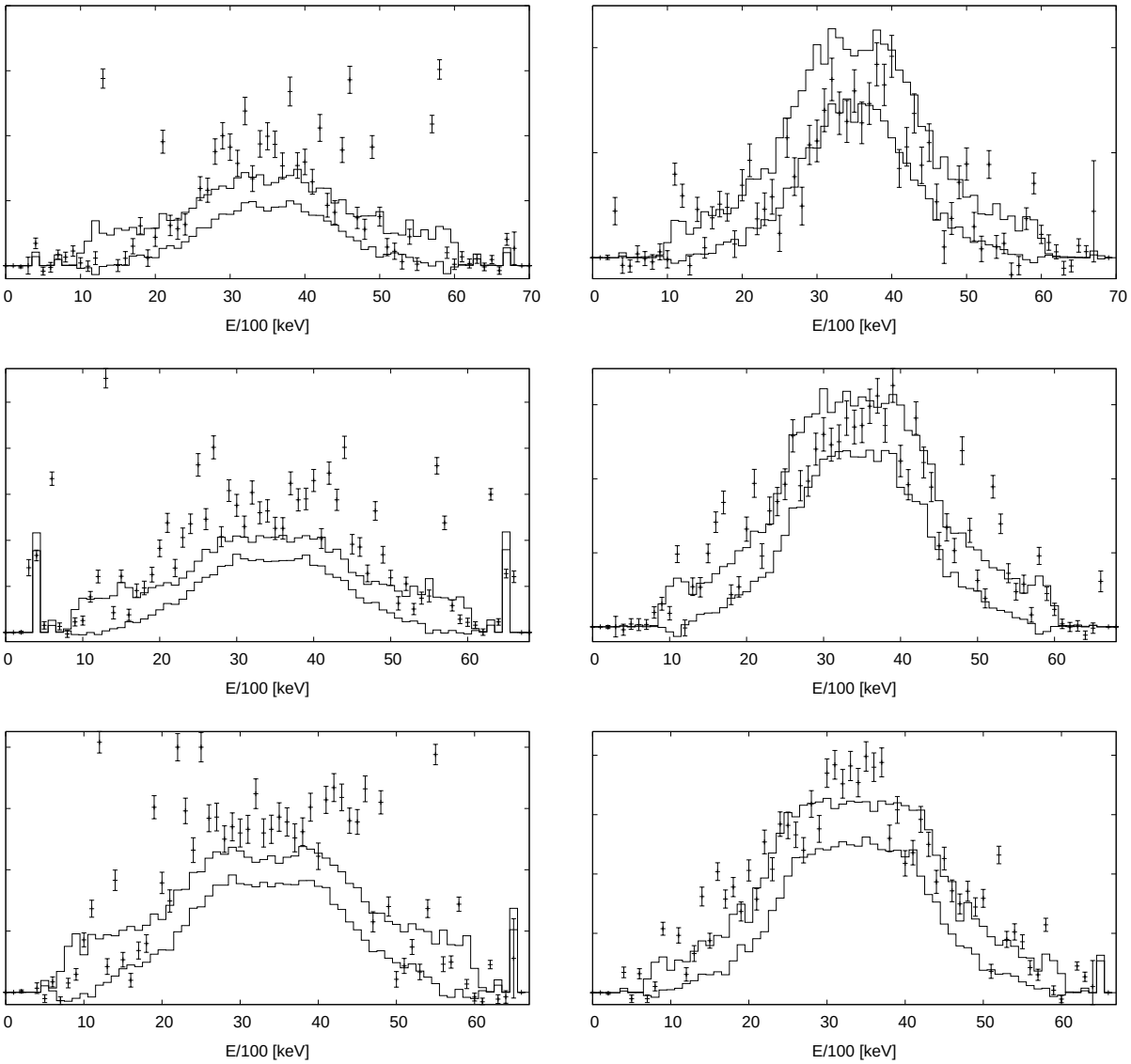

Figure 4.17: The TSC spectra for the model combination 41116 with SC resonance parameters (4.1;1.4;3.0).

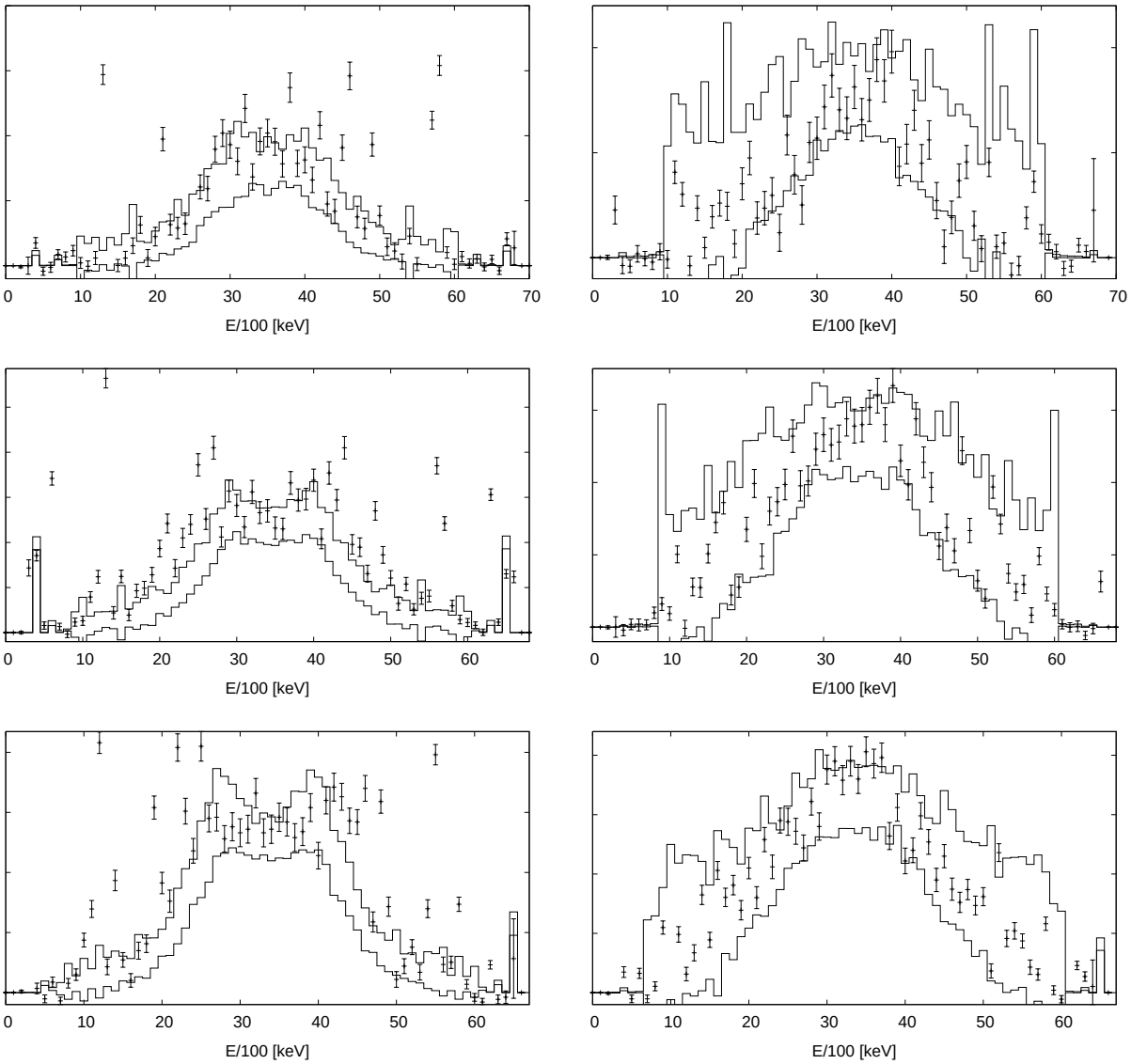

Figure 4.18: The TSC spectra for the model combination 11110 with SC resonance parameters (4.0;1.0;3.0).

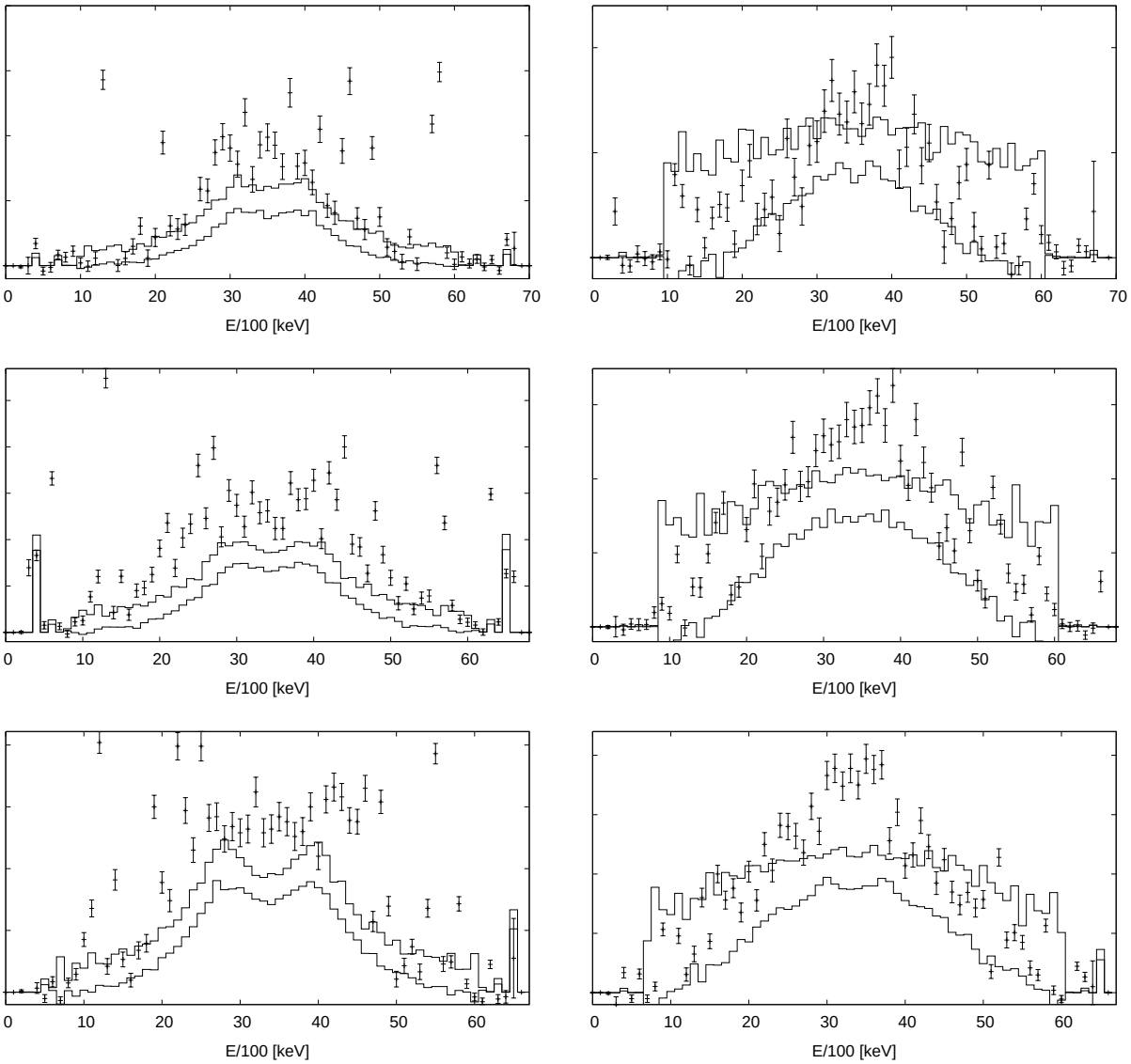

Figure 4.19: The TSC spectra for the model combination 11116 with SC resonance parameters (4.0;1.0;3.0).

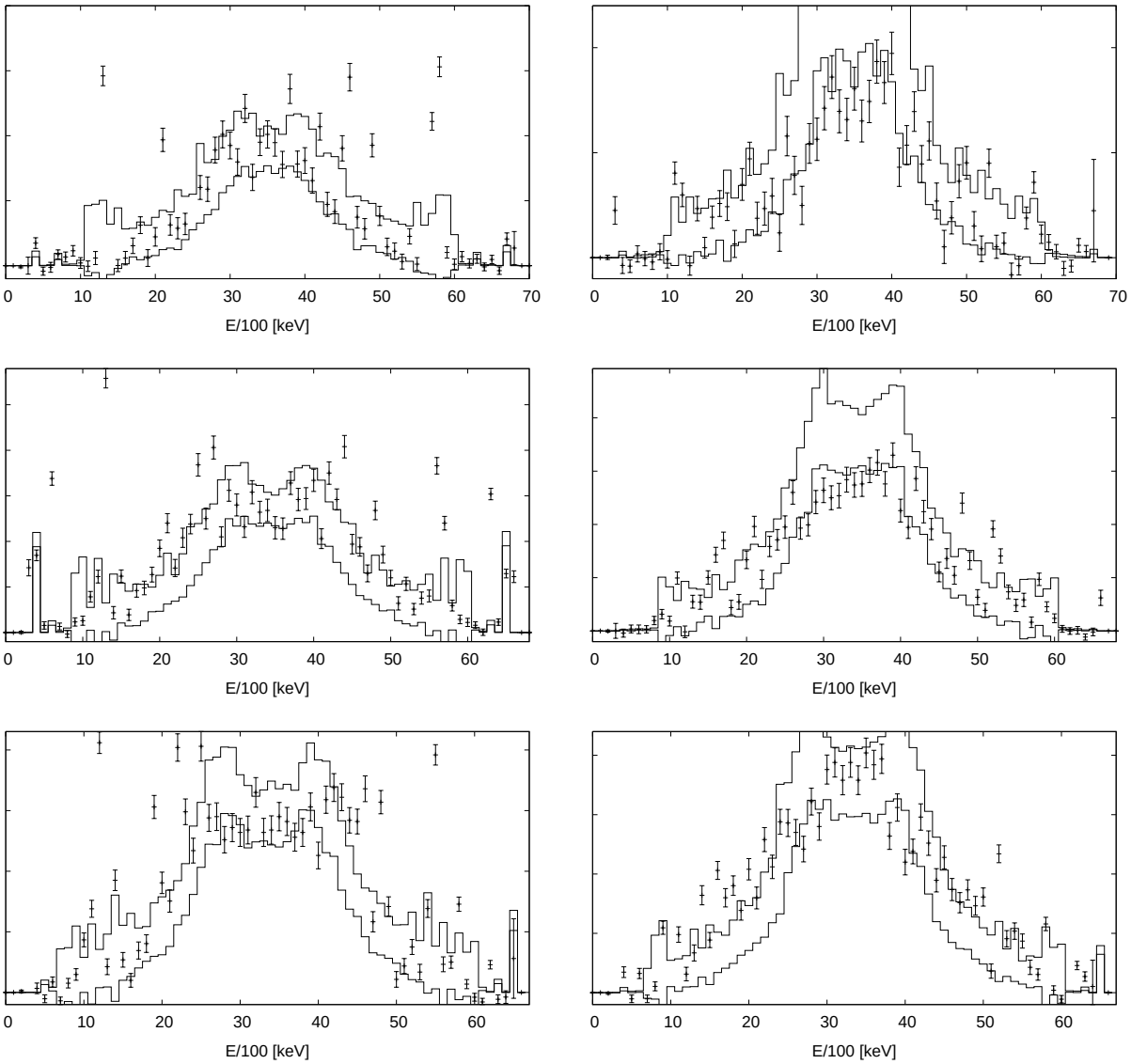

Figure 4.20: The TSC spectra for the model combination 41110 with SC resonance parameters (4.0;1.0;3.0).

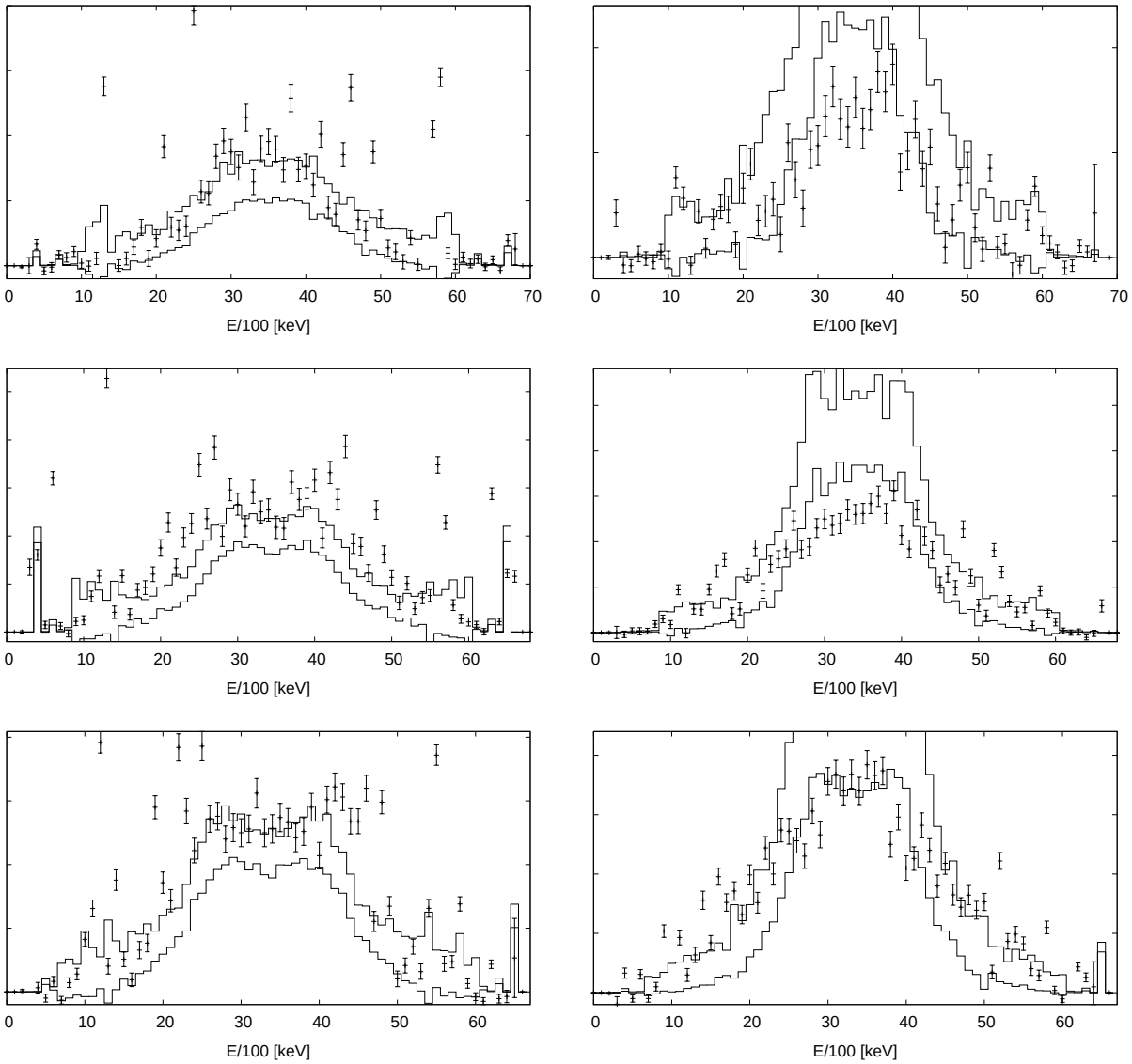

Figure 4.21: The TSC spectra for the model combination 51110 with SC resonance parameters (4.0;1.0;3.0).

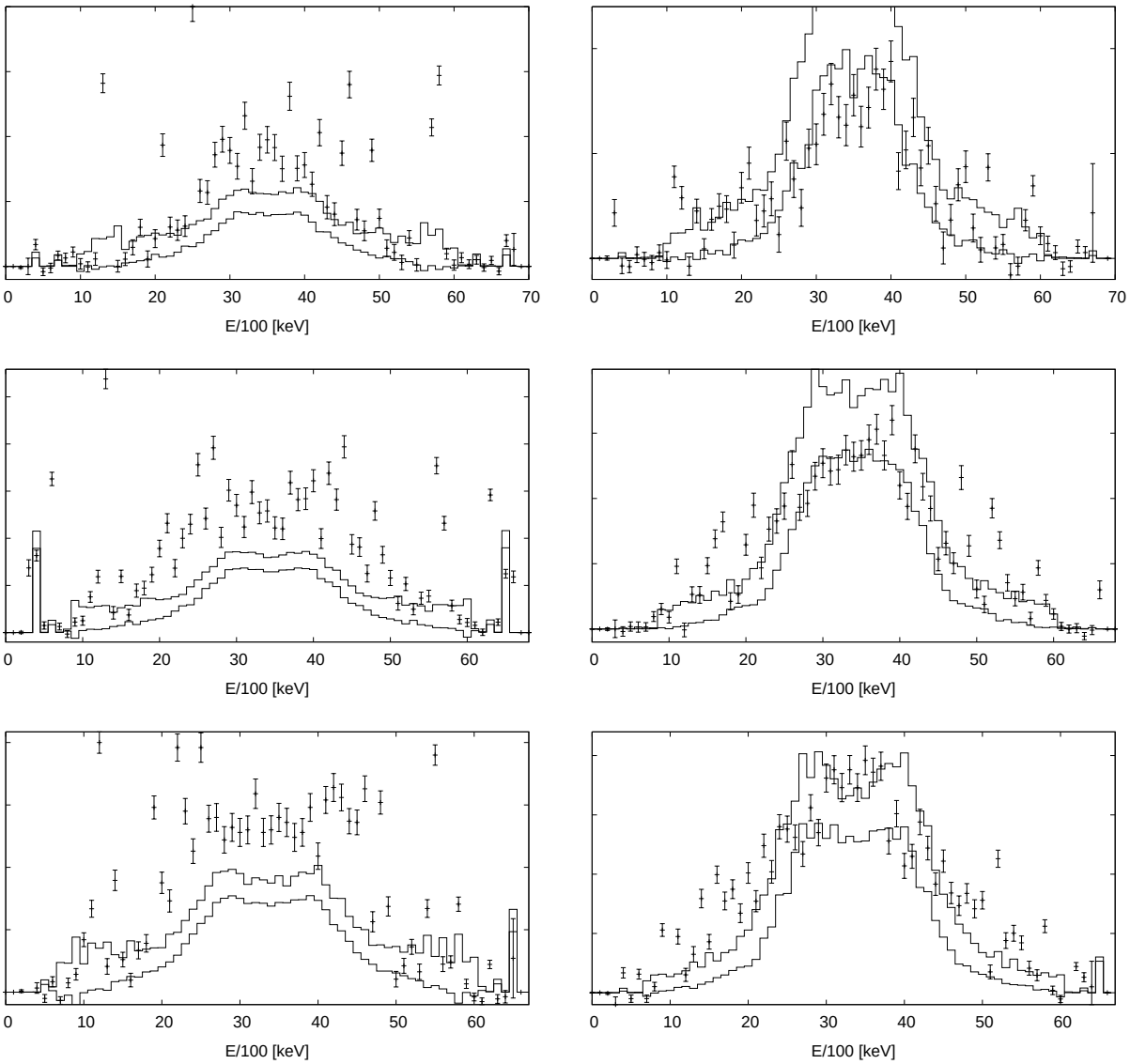

Figure 4.22: The TSC spectra for the model combination 51116 with SC resonance parameters (4.0;1.0;3.0).

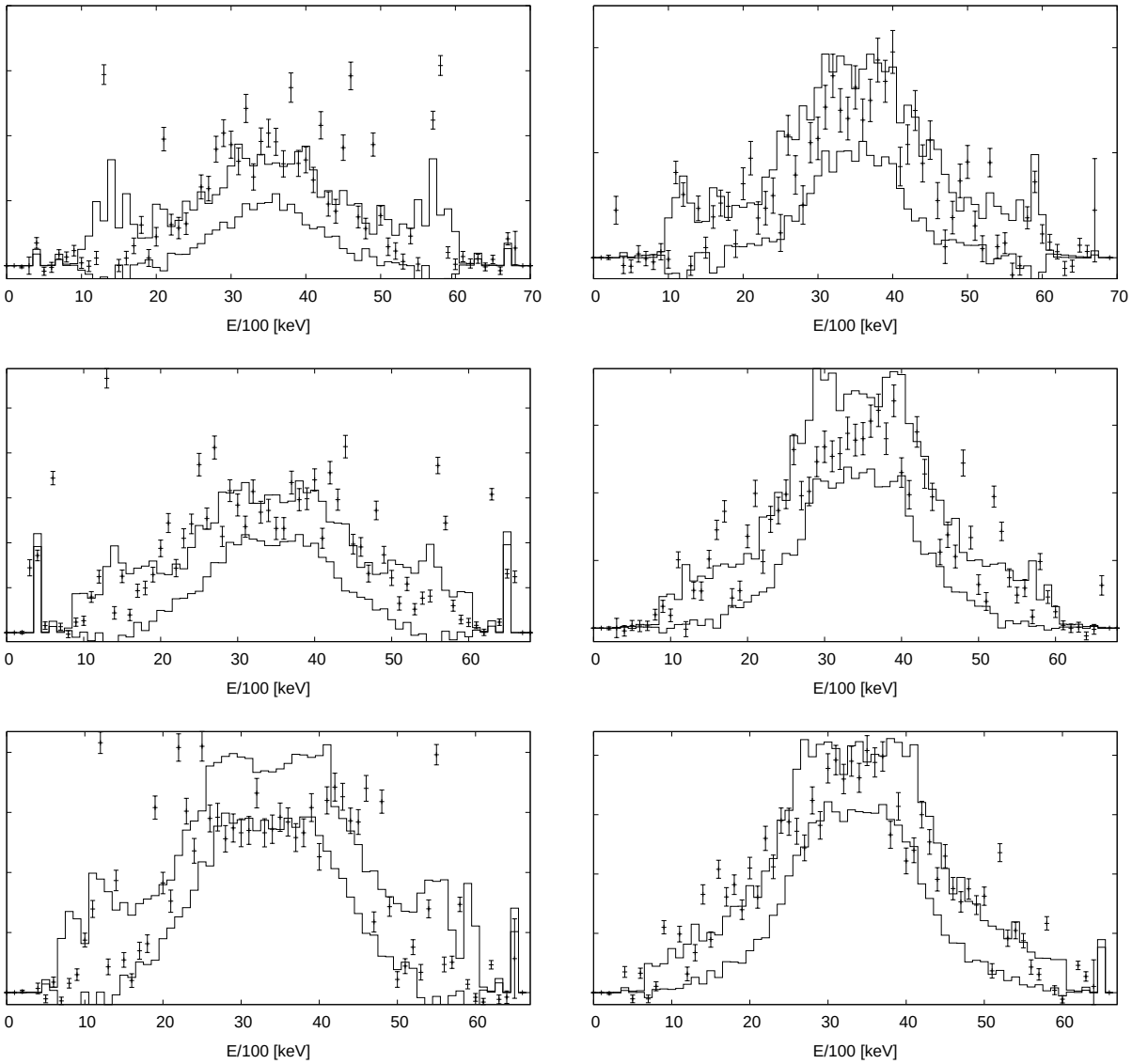

Figure 4.23: The TSC spectra for the model combination 61110 with SC resonance parameters (4.0;1.0;3.0).

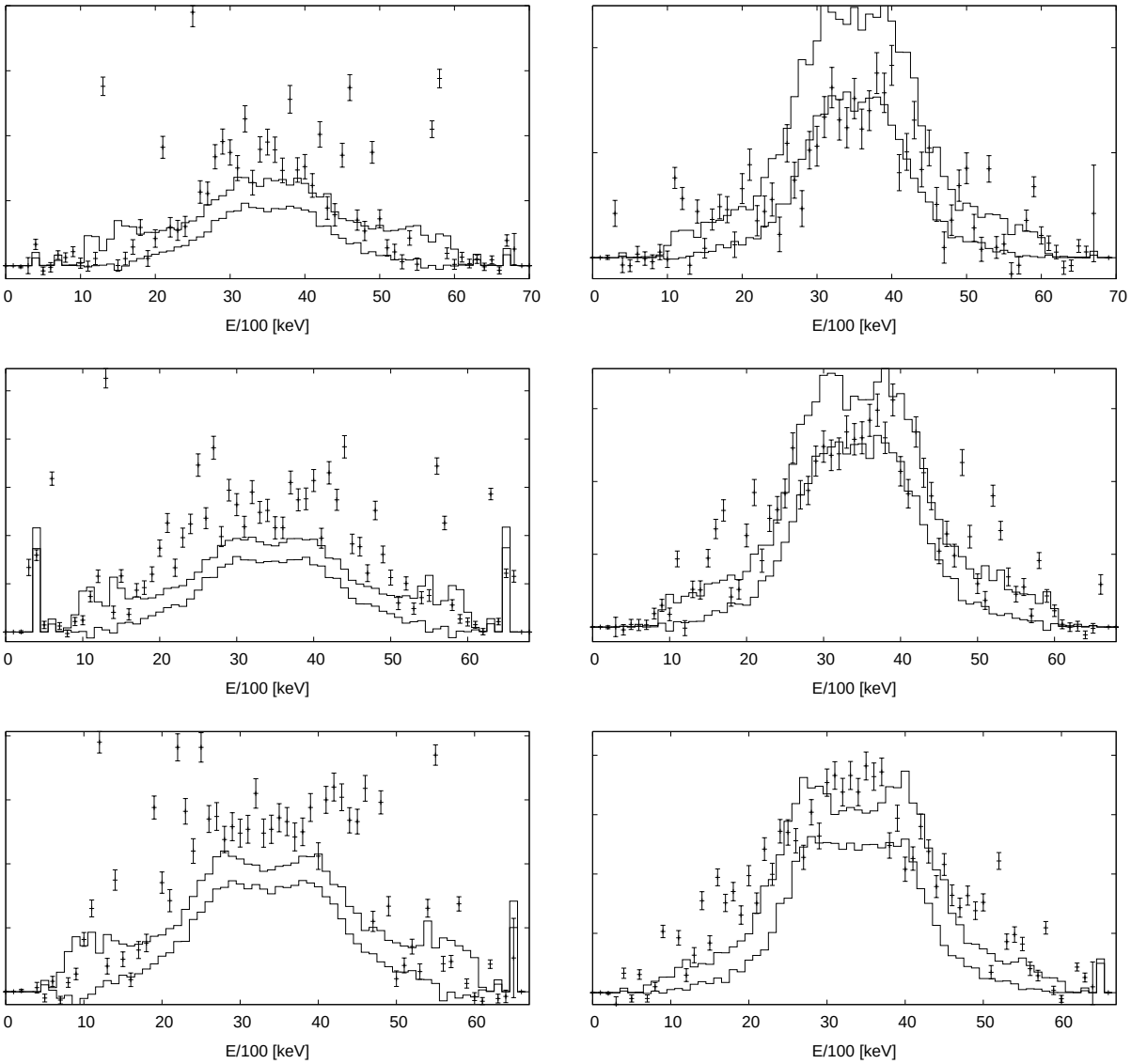

Figure 4.24: The TSC spectra for the model combination 61116 with SC resonance parameters (4.0;1.0;3.0).

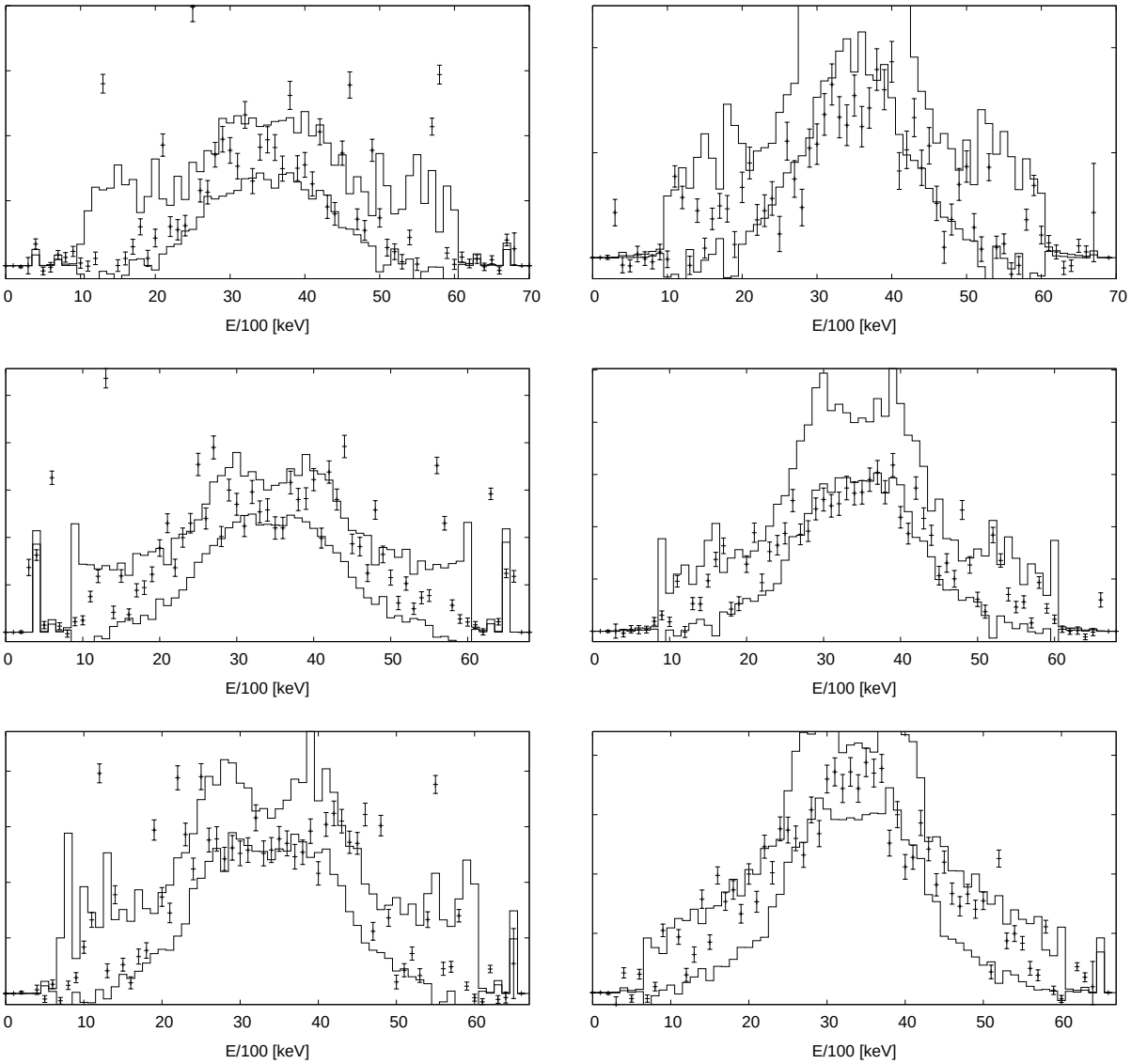

Figure 4.25: The TSC spectra for the model combination X1110 with SC resonance parameters (4.0;1.0;3.0).

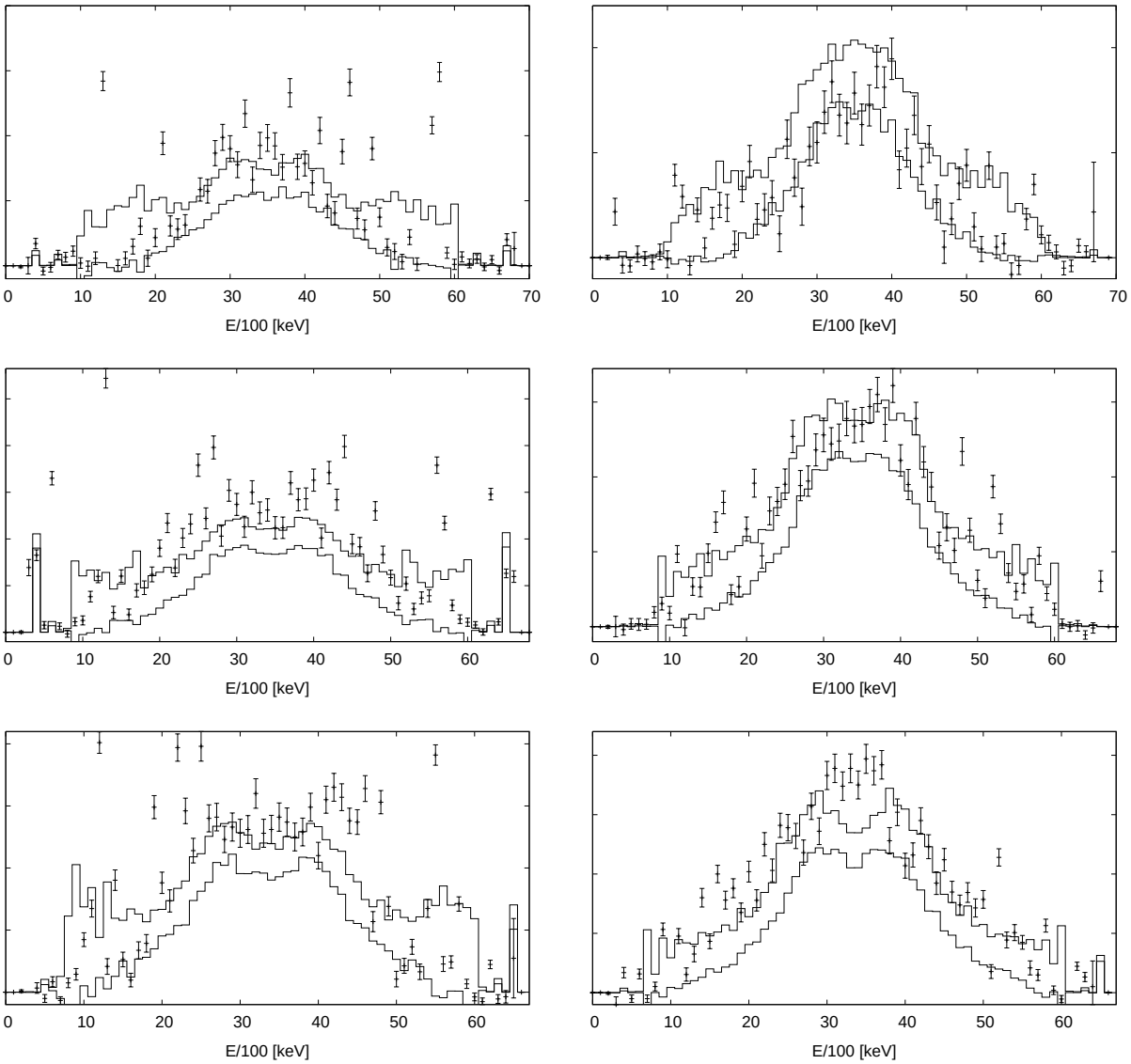

Figure 4.26: The TSC spectra for the model combination X1116 with SC resonance parameters (4.0;1.0;3.0).

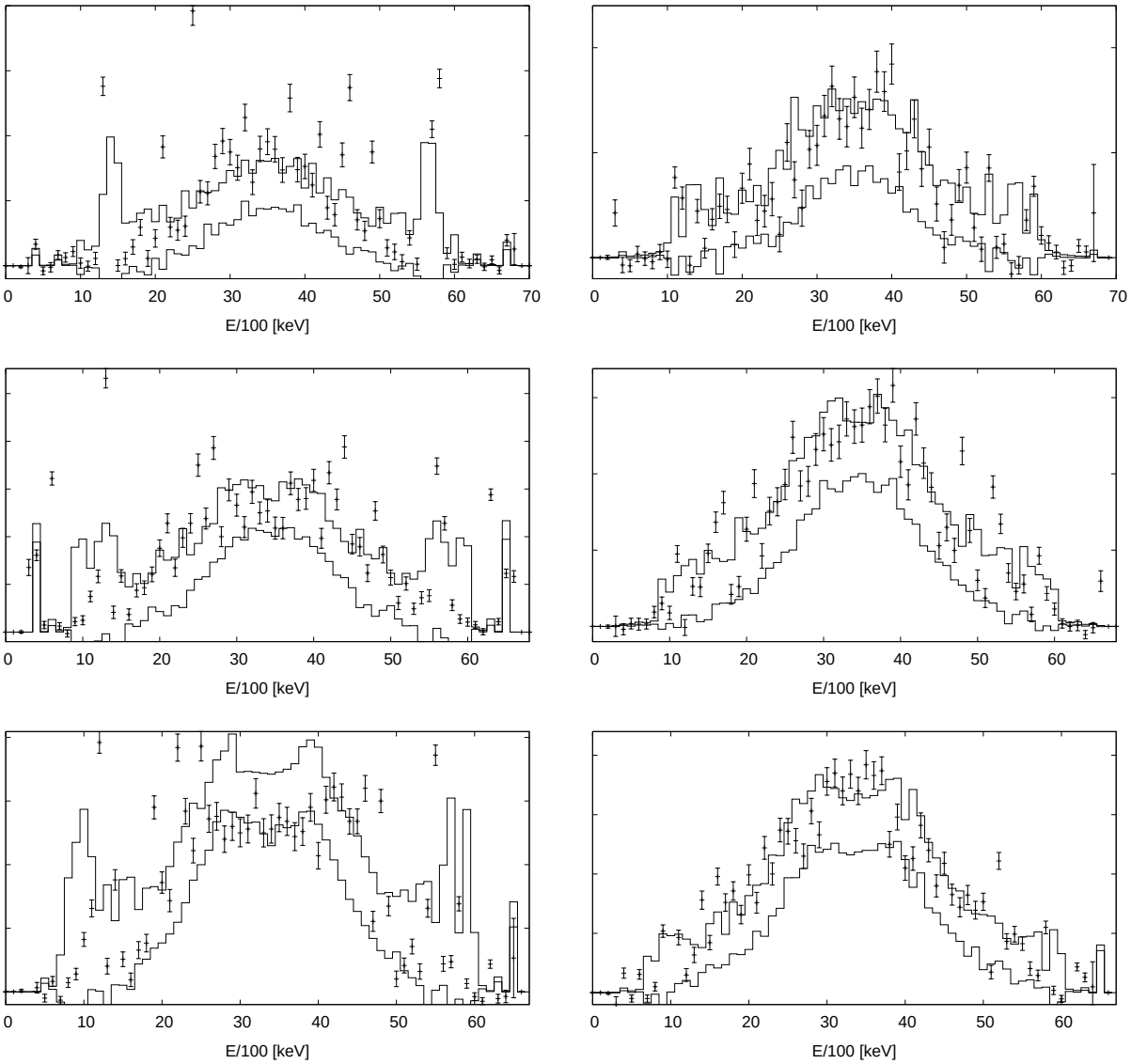

Figure 4.27: The TSC spectra for the model combination 61110 with SC resonance parameters (4.0;1.0;2.0).

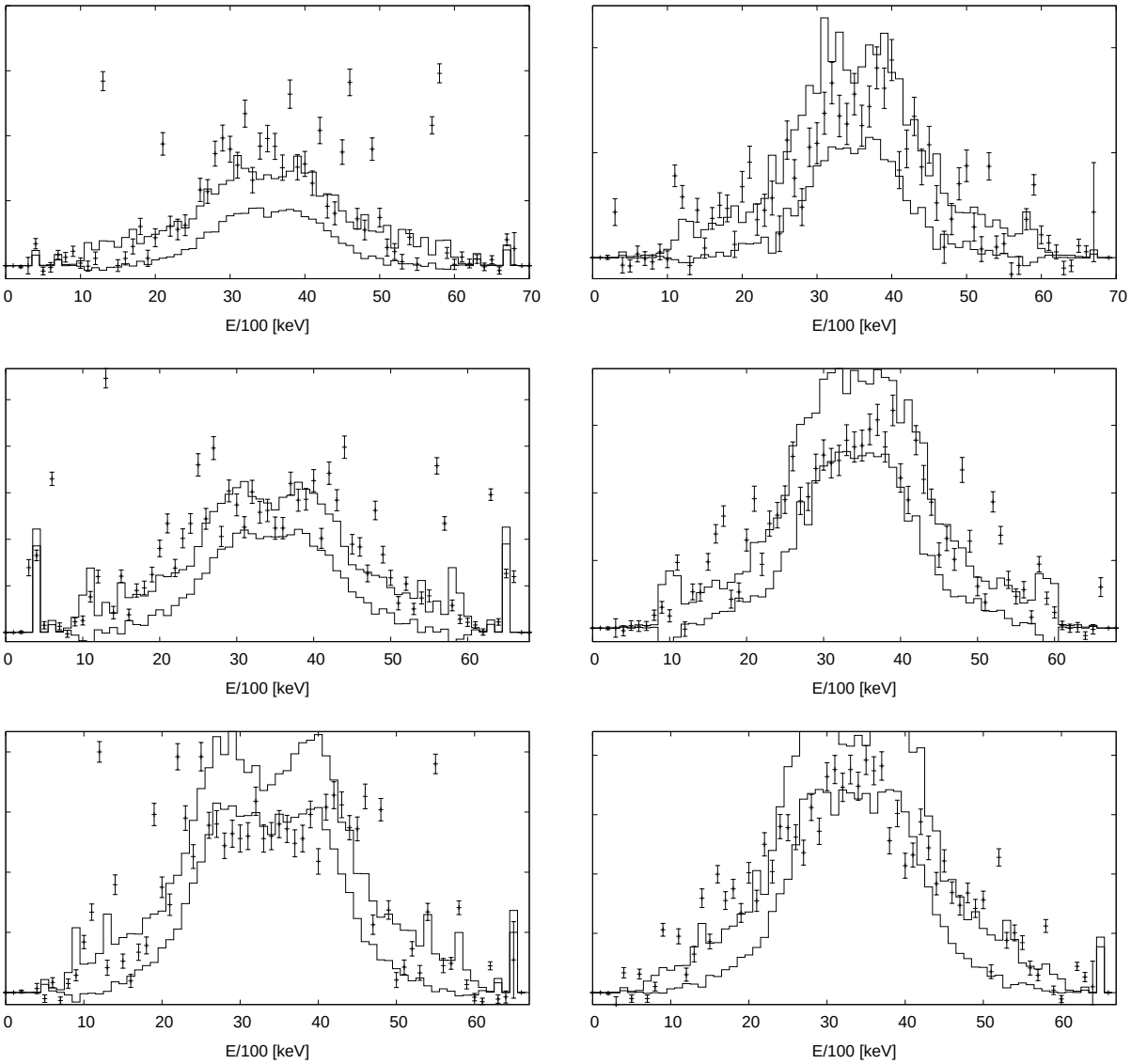

Figure 4.28: The TSC spectra for the model combination 41118 with SC resonance parameters (4.0;1.0;3.0).

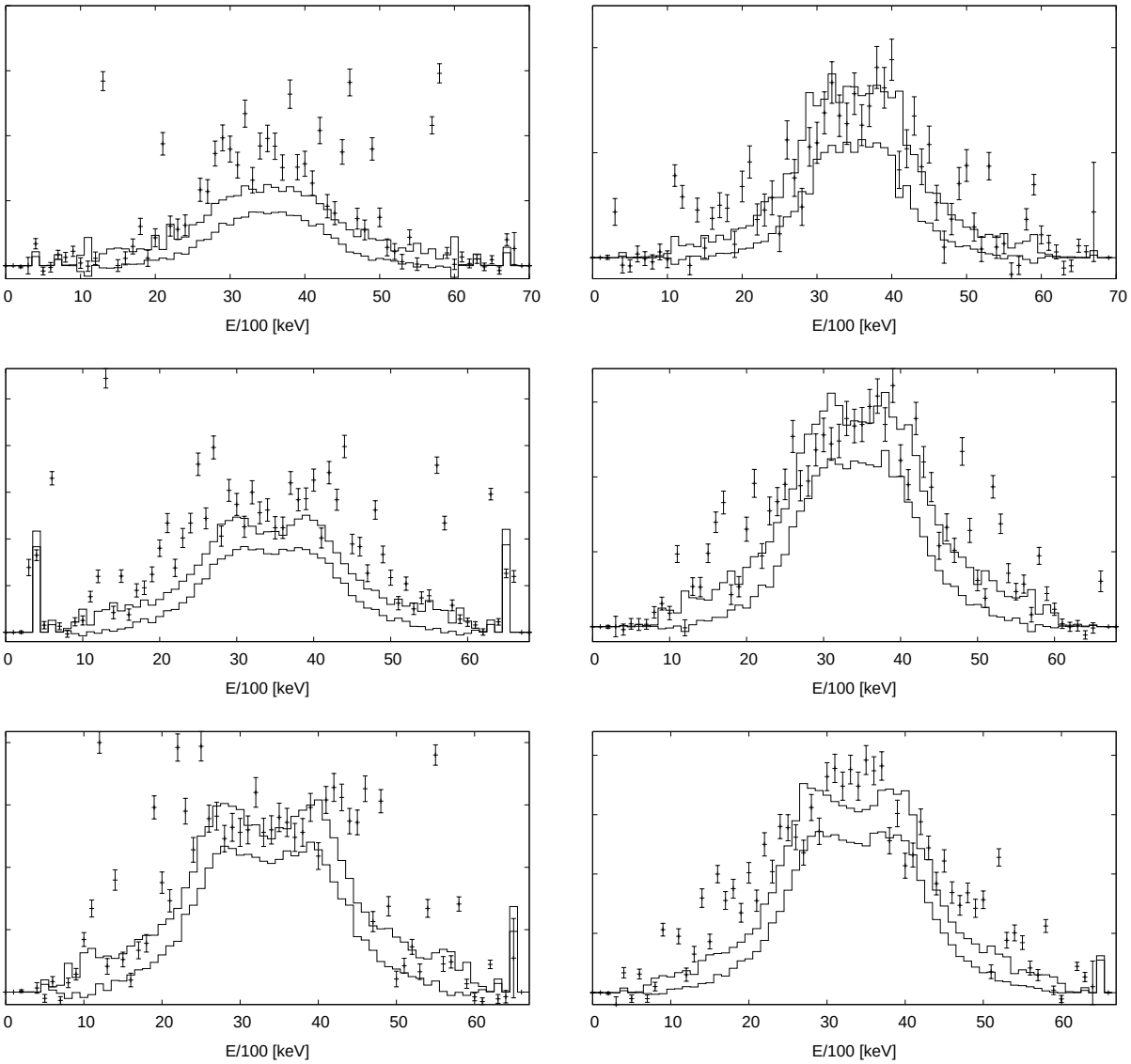

Figure 4.29: The TSC spectra for the model combination 41119 with SC resonance parameters (4.0;1.0;3.0).

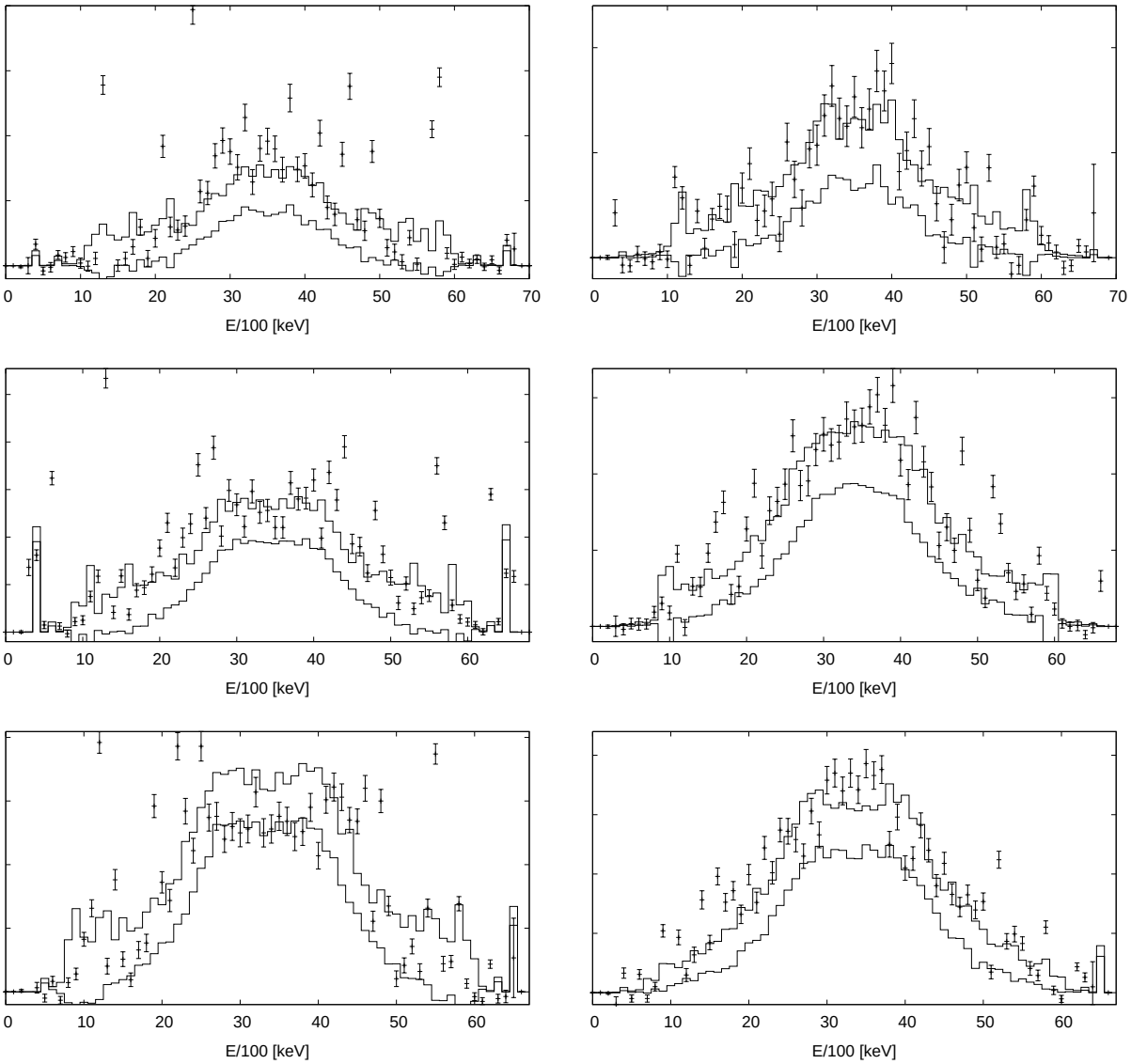

Figure 4.30: The TSC spectra for the model combination 61118 with SC resonance parameters (4.0;1.0;3.0).

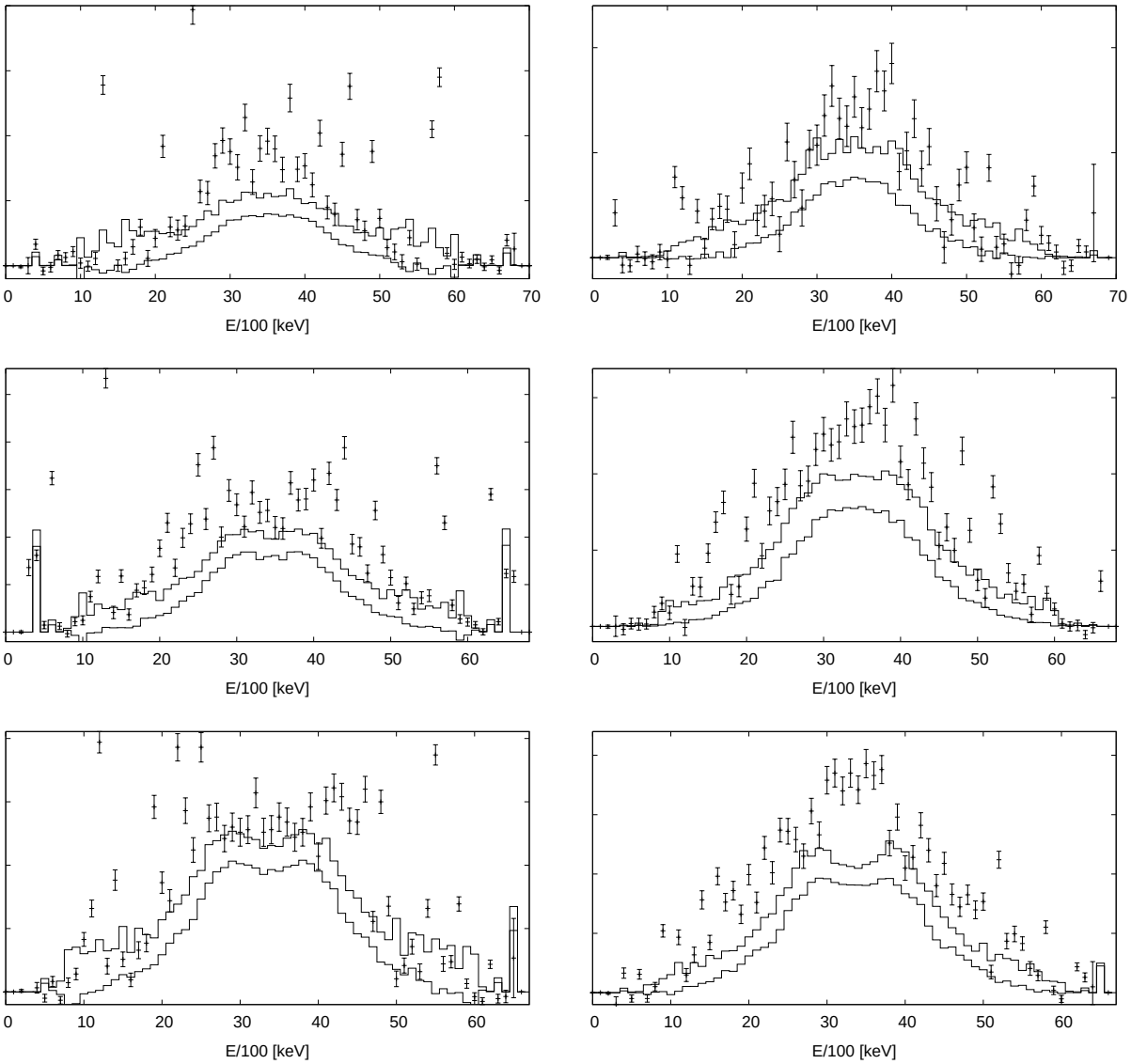

Figure 4.31: The TSC spectra for the model combination 61119 with SC resonance parameters (4.0;1.0;3.0).

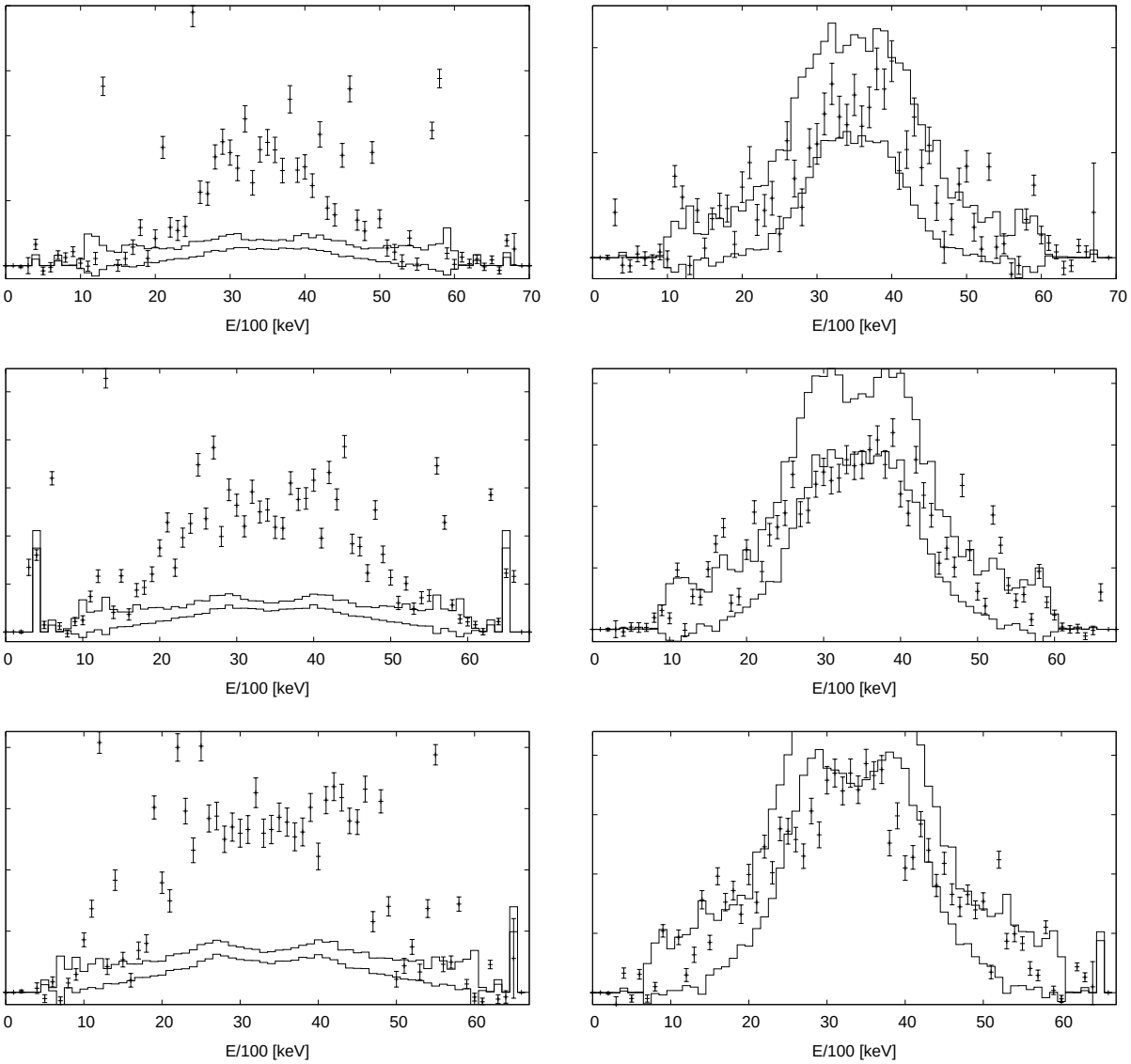

Figure 4.32: The TSC spectra for the test of presence of the pigmy mode in $E1$ PSF. The parameters of the pigmy mode are same as for the SC resonance, (4.0;1.0;3.0).

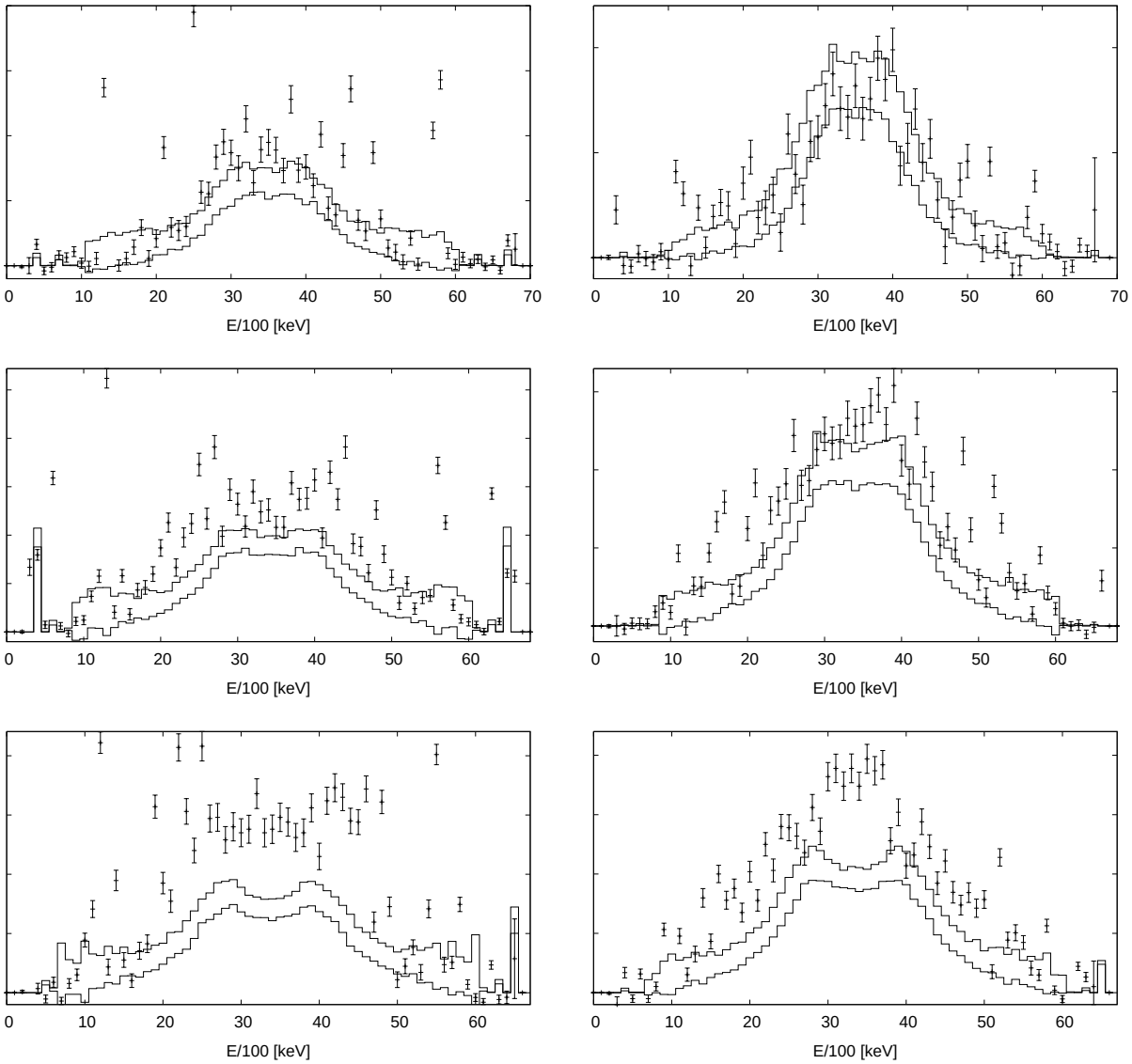

Figure 4.33: The TSC spectra for the test of presence of the pigmy mode in $E2$ PSF. The parameters of the additional resonance in the $E2$ PSF are (4.0;1.0;3.0).

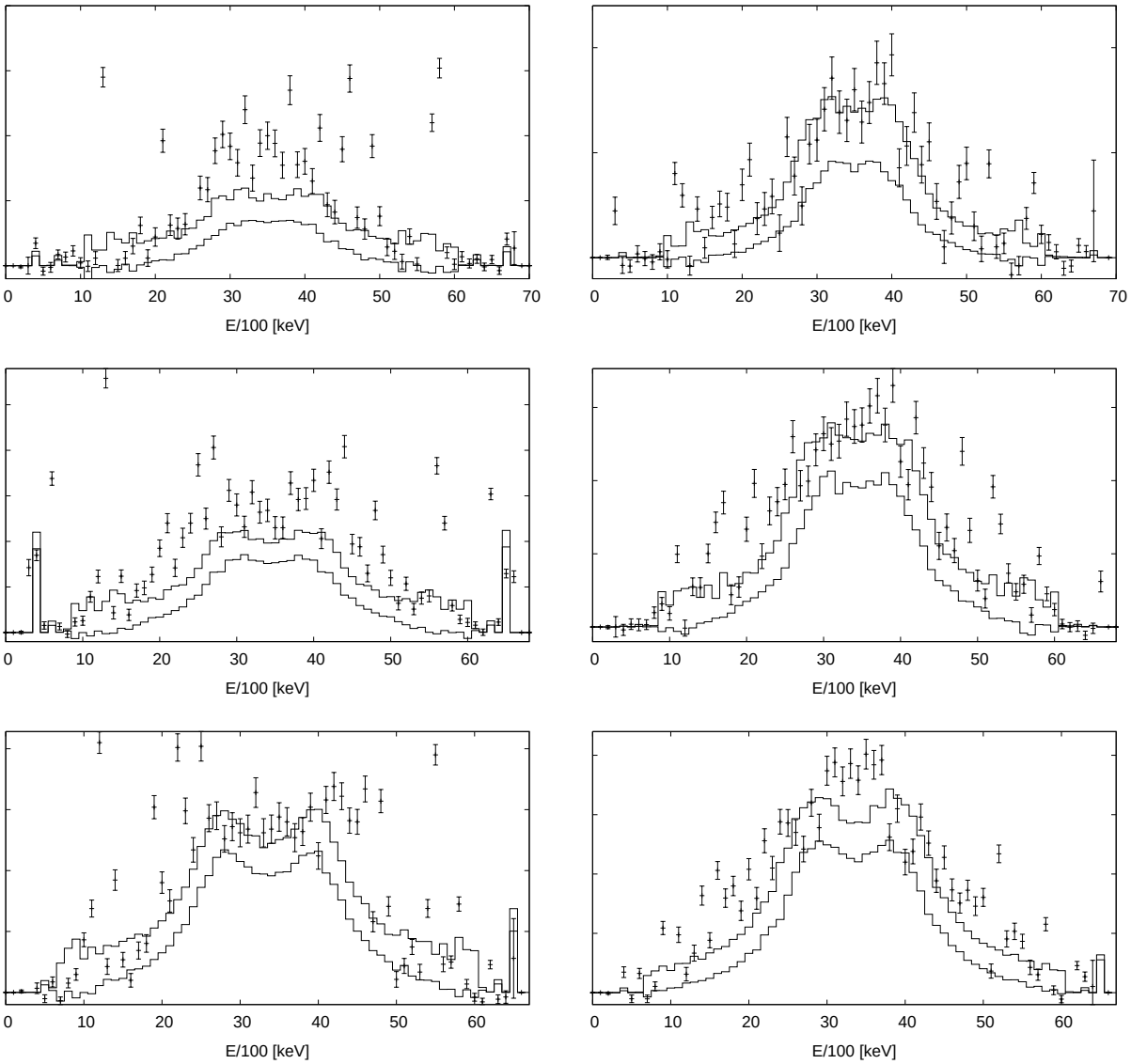

Figure 4.34: The TSC spectra for the test of $M1$ PSF without SF mode. The parameters of the SC resonance are (4.0;1.0;3.0).

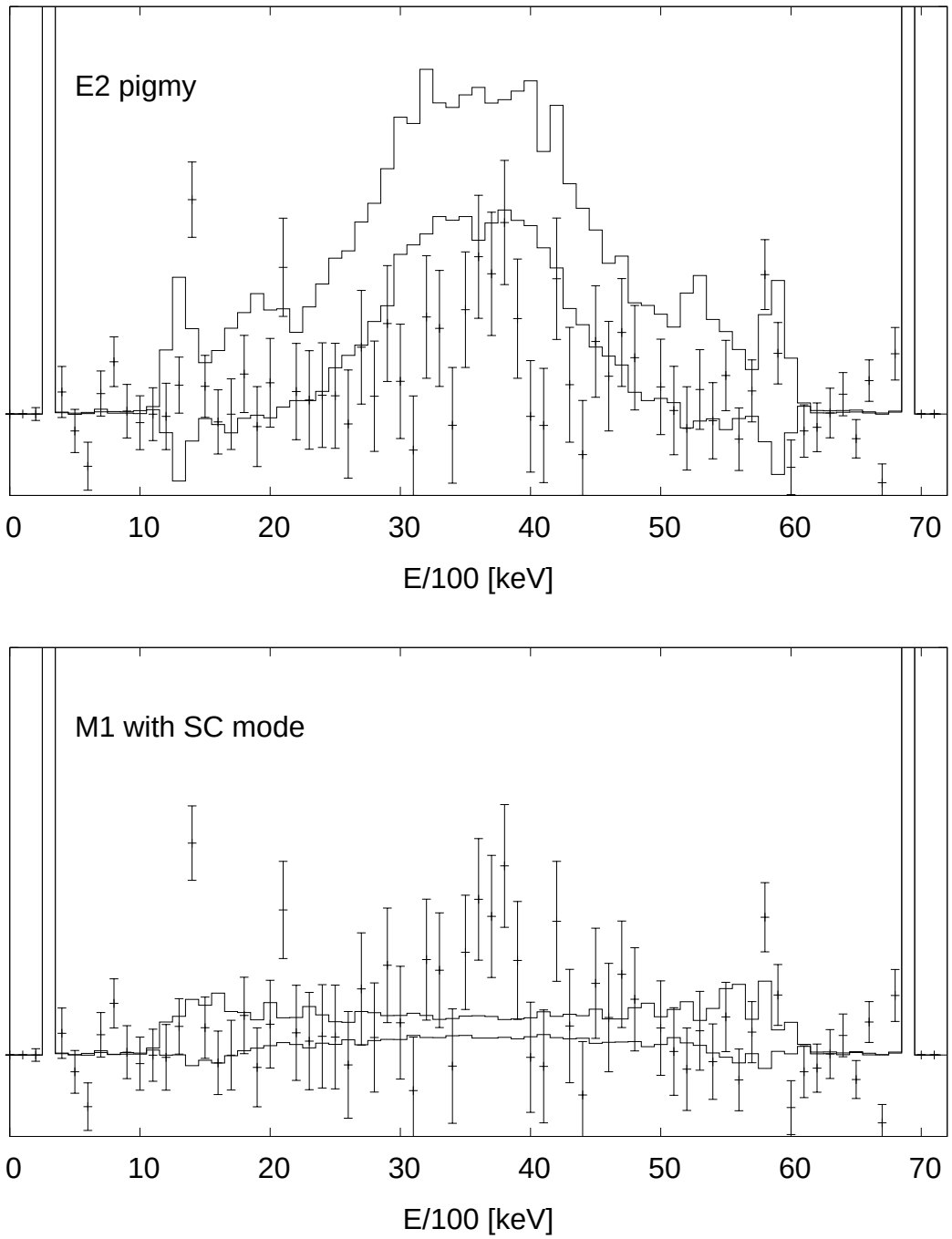

Figure 4.35: The ground state TSC spectra for the test of presence of the pigmy mode in $E2$ PSF. The parameters of the pigmy mode are same as for the SC resonance, (4.0;1.0;3.0).

Chapter 5

Summary

The experimental data from two-step cascades measurements of the ^{176}Lu(n,γ)^{177}Lu reaction were processed to form comparable with simulation results produced by the code `DICEBOX`. The studied nucleus ^{177}Lu is unique thanks to relatively high spins of the nuclear levels involved in the process of γ-deexcitation of nucleus. These spins are higher than in any other nucleus studied so far – the spin of neutron resonances are $\frac{13}{2}$ and $\frac{15}{2}$. The main results that were obtained from comparison of experimental spectra with simulations can be summarized as follows:

- Experimentally observed shapes of TSC spectra *cannot* be reproduced without postulating a resonance structure in a PSF. The resonance structure was proved to be of magnetic dipole character and it is identified with the scissors mode vibrations.
- The energy center of the scissors mode must be very close to $E_{SC} = 4$ MeV to provide reasonable agreement with the experimental data.
- The parameters of SC mode – $E_{SC} = 4$ MeV, $\Gamma_{SC} \geq 1.0$ MeV and $\sigma_{SC} \geq 2.0$ mb – are very different compared to the parameters that were observed so far. Both the energy center and the total strength of the scissors mode are significantly higher than the energy center and strength observed so far in any other nucleus, see Fig. 5.1. This conclusion may suggest that the parameters of SC mode depend on spin.
- The scissors mode has to be build on all levels in the nucleus and, at least its position, has to be very stable with excitation.
- We are unable to make strong restrictions on the possible models of $E1$ PSF. But the $E1$ PSF models with a non-zero limit for $E_\gamma \to 0$ give better description of experimental data.

- Only dipole strength seems to be important in the decay. We have found almost no dependence of simulated spectra on adopted model for $E2$ PSF model.

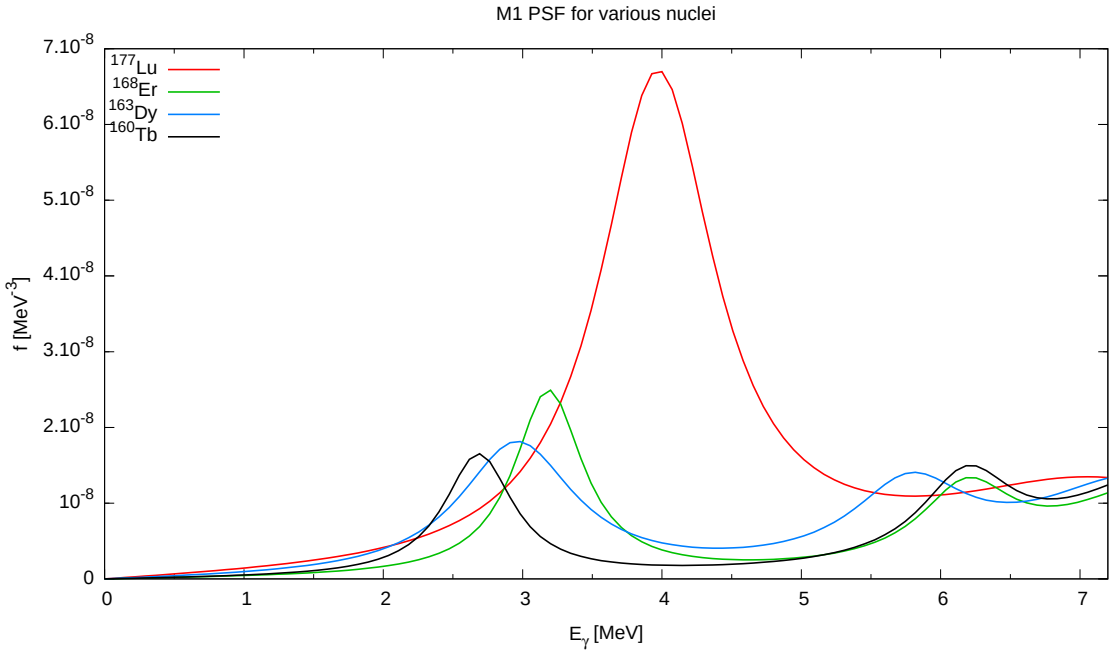

Figure 5.1: The comparsion of SC parameters for several nuclei - ^{177}Lu with SC mode parameters (4.0,1.0,3.0), ^{168}Er with (3.2,0.6,0.9), ^{163}Dy with (3.0,1.0,0.6) and ^{160}Tb with (2.7,0.6,0.5). The parameters for ^{156}Gd and ^{158}Gd are very similar to those for ^{163}Dy. The results are taken from [51] for ^{160}Tb and from [50] for other nuclei.

Bibliography

[1] G.A. Bartholomew, *Ann. Rev. Nucl. Sci.* **11** (1961) 259

[2] N. Bohr, *Nature* **137** (1936) 344

[3] H.A. Bethe, *Phys. Rev.* **50** (1936) 332; H.A. Bethe, *Rev. Mod. Phys.* **9** (1937) 69

[4] T.D. Newton, *Can. J. Phys.* **50** (1956) 804

[5] A. Gilbert and A.G.W. Cameron, *Can. J. Phys.* **43** (1965) 1446

[6] G. Reffo, *Parameter Systematics for Statistical Theory Calculations of Neutron Reaction Cross Section* in Nuclear Theory for Applications, IAEA-SMR-43 (1979) p.205

[7] V. Paar, D.K. Sunko, S. Brant, M.G. Mustafa and R.G. Lanier, *Z. Phys.* **A345** (1993) 343

[8] F. Garcia *et al., Phys. Rev.* **C60** (1999) 0643311

[9] T. von Edigy and D. Bucurescu, Systematics of nuclear level density parameters, August 11, 2005

[10] T. von Edigy, H.H. Schmidt and A.N. Behkami, *Nucl. Phys.* **A481** (1988) 189

[11] A.V. Ignatyuk, K.K. Istetov and G.N. Smirenkin, *Yad. Fiz.* **29** (1979) 875; *Sov.J. Nucl. Phys.* **29** (1979) 450
A.V. Ignatyuk, J.L. Weil, S. Raman and S. Kahane, *Phys. Rev.* **C47** (1993) 1504

[12] G. Audi, A. H.Wapstra, and C. Thibault, *Nucl. Phys.* **A729** (2003) 337

[13] T. von Edigy and D. Bucurescu, *Phys. Rev.* **C80** (2009) 054310

[14] N. Cerf, *Nucl. Phys.* **A554** (1993) 85

[15] B. Pichon, *Nucl. Phys.* **A568** (1994) 553

[16] B.V. Zhuravlev, *et al., Yad. Fiz.* **39** (1984) 264
G.N. Lovtsikova *et al.*, in *Proceeding of the 4th International Symposium*, Smolenice, Czechoslovakia, June 1985, p. 82, edited by J. Krištiak and E. Běták
B.V. Zhuravlev, N.N. Titarenko and V.I. Trykova, in *Proceedings of the OECD Meeting: Nuclear Level Densities*, ENEA, Bologna, Italy, November 15-17 1989, p. 210, ed. by G. Reffo, M. Herman and G. Maino
V.G. Pronyaev *et al., Yad. Fiz.* **30** (1979) 604; *Sov. J. Nucl. Phys.* **30** (1979) 310
B.V. Zhuravlev, N.N. Titarenko and V.I. Trykova, in *Proc. of VII International Seminar on Interaction of Neutrons with Nuclei*, Dubna May 25-28 1999, p. 208

[17] B.V. Zhuravlev, in *Proc. of VI International Seminar on Interaction of Neutrons with Nuclei*, Dubna, May 13-16 1998, p. 161

[18] T.S. Tveter, L. Berghold, M. Guttormsen, E. Melby and J. Rekstad, *Phys. Rev. Lett.* **77** (1996) 2404

[19] E. Melby *et al., Phys. Rev. Lett.* **83** (1999) 3150

[20] A. Schiller, M. Guttormsen, E. Melby, J. Rekstad and S. Siem, *Phys. Rev.* **C61** (2000) 044324

[21] D.M. Brink, Thesis, Oxford University, 1955

[22] G.C. Baldwin and G.S. Kleiber, *Phys. Rev.* **71** (1947) 3; *Phys. Rev.* **73** (1948) 1156

[23] A.B. Migdal, *J. Phys.* (USSR) **8** (1944) 331

[24] H. Steinwedel and J.H.D. Jensen, *Z. Naturforsch.* **5a** (1950) 413

[25] M. Goldhaber and E. Teller, *Phys. Rev.* **74** (1948) 1046

[26] S.G. Kadmenskij, V.P. Markushev and V.I. Furman, *Sov. J. Nucl. Phys.* **37** (1983) 165, *Yad. Fiz.* **37** (1983) 227

[27] A.H. Wapstra and G. Audi, *Nucl. Phys.* **A432** (1985) 55

[28] F. Bečvář *et al., Yad. Fiz.* **46** (1987) 3

[29] F. Bečvář, M.E. Montero-Cabrera, Huynh Thuong Hiep and S.A. Telezhnikov, in *Proc. of the 6th Int. Symposium on Capture Gamma-Ray Spectroscopy and Related Topics*, Lauven, Belgium, 1987

[30] R.E. Chrien, in *Proc. of the Vth International School on Neutron Physics*, Alushta, Dubna 1987, ed. by B.B. Kolesova and V.R. Sarantseva (Dubna Report No. D3, 4, 17-86-747, 1987)

[31] V.I. Furman *et al., Phys. Lett.* **B44** (1973) 465

[32] L. Aldea and H. Seyfarth, in *Neutron capture Gamma-Ray spectroscopy*, ed. by R.E. Chrien and W. Kane, N.Y.Plenum Press (1979) 529

[33] J.Kopecky, M. Uhl and R.E. Chrien, *Phys. Rev.* **C47** (1993) 312

[34] J. Kopecky, M. Uhl and R.E. Chrien, ECN internal report ECN-RX-92-011, 1992

[35] J. Kopecky, *Handbook for calculations of nuclear reaction data*, IAEA-TECDOC-1034, August 1998, p. 97; available at http://iaeand.iaea.or.at/ripl/

[36] S.K. Kataria, V.S. Ramamurthy and S.S. Kapoor, *Phys. Rev.* **C18** (1978) 549

[37] B.L. Berman et al., *Phys. Rev.* **185** (1969) 1576

[38] U. Kneissl, H.H. Pitz and A. Zilges, *Prog. Part. Nucl. Phys.* **37** (1996) 349

[39] A. Schiller *et al., Yad. Fiz.* **64** (2001) 1263; *Phys. Atomic Nuclei* **64** (2001) 11186

[40] L.M. Bollinger and G.E. Thomas, *Phys. Rev.* **C2** (1970) 1951

[41] A. Richter, *Prog. Part. Nucl. Phys.* **34** (1995) 261

[42] M.A. Lone *et al.*, in *Proceeding of Second International Symposium on Neutron Capture Gamma Ray Spectroscopy and Related Topics*, September 2-6 1974, Petten, The Netherlands

[43] J. Kopecky and R.E. Chrien, *Nucl. Phys.* **A468** (1987) 285

[44] J. Speth, *Int. Rev. of Nucl. Phys.* **7** (1991), Electric and Magnetic Giant Dipole Resonances in Nuclei (World Scientific) 56

[45] D. Bohle *et al., Phys. Lett.* **B137** (1984) 27

[46] N. Lo Iudice and F. Palumbo, *Phys. Rev. Lett.* **53** (1978) 1532

[47] A. Zigles *et al., Phys. Rev.* **C58** (1998) 184

[48] F. Bečvář, P. Cejnar, J. Honzátko, K. Konečný, I. Tomandl and R.E. Chrien, *Phys. Rev.* **C52** (1995) 1278

[49] M. Krtička *et al., Phys. Rev. Lett.* **92** (2004) 172501

[50] M. Krtička, Doctoral Thesis, April 2002

[51] J. Kroll, Diploma Thesis, April 2009

[52] S. Raman, in *Proc. of the 4th Int. Symposium on Capture Gamma-Ray Spectroscopy and Related Topics*, ed. by T. von Egidy, F. Gönnenwein and B. Meier (Inst. Phys. Conf. Ser. No. 62, London, 1982)

[53] W.V. Prestwich, M.A. Islam and T.J. Kennett, *Z. Phys.* **A315** (1984) 103

[54] K.A. Snover, *Ann. Rep. Nucl. Part. Sci.* **36** (1986) 545

[55] P.J. Siemens and A.S. Jensen, *Elements of Nuclei* (Addison-Wesley, 1987)

[56] M. Igashira, H. Kitazawa, H. Shimizu, H. Komano and N. Yumamuro, *Nucl. Phys.* **A457** (1986) 301

[57] A. Voinov *et al., Phys. Rev.* **C63** (2001) 044313

[58] S. Joly, D.M. Drake and L.Nilsson, *Phys. Rev.* **C20** (1979) 2072

[59] S. Mizuno, M. Igashira, H. Kitazawa, in *Proceedings of the CGS9*, Budapest, Hungary, Springer (1997)

[60] F. Bečvář, *Nucl. Instr. Meth.* **A417** (1998) 434

[61] B. Krusche *et al., Nucl. Phys.* **A386** (1986) 245

[62] J. Honzátko, K. Konečný, I. Tomandl, J. Vacík, F. Bečvář and P. Cejnar, *Nucl. Instr. Meth.* **A376** (1996) 434

[63] A.A. Bogdzel *et al.*, JINR Report No. P15-82-706, Dubna, 1982

[64] I. Tomandl, Doctoral Thesis, Řež (UJF Řež), 1997

[65] K.S. Krane and R.M. Steffen, *Phys. Rev.* **C2** (1970) 724

[66] D.C. Camp and A.L. van Lehn, *Nucl. Instr. and Meth.* **76** (1969) 192

[67] A.M. Hoogenboom, *Nucl. Instr. Meth.* **3** (1958) 57

[68] S.T. Boneva *et al., Particles & Nuclei* **22** (1991) 479 (in Russian)

[69] C.E. Porter and R.G. Thomas, *Phys. Rev.* **C2** (1956) 2030

[70] P. Petkov, W. Andrejtscheff, H. G. Börner, S. J. Robinson, N. Klay and S. Yamada, *Nucl. Phys.* **A599** (1996) 505

[71] A.V. Ignatyuk, Contribution to the Third CRP Meeting on RIPL, Trieste (1997)